



## Removal of Boron from Simulated Iraqi Surface Water by Electrocoagulation Method

Waleed M. Salih, Saadi K. Alnasri, and Ali Abdulameer Al Abdalaali

Environmental Engineering Department, Collage of Engineering, University of Baghdad

### Abstract

The removal of boron from aqueous solution was carried out by electrocoagulation (EC) using magnesium electrodes as anode and stainless steel electrodes as cathode. Several operating parameters on the removal efficiency of boron were investigated, such as initial pH, current density, initial boron ion concentration, NaCl concentration, spacing between electrodes, electrode material, and presence of carbonate concentration. The optimum removal efficiency of 91.5 % was achieved at a current density of 3 mA/cm<sup>2</sup> and pH = 7 using (Mg/St. St.) electrodes, within 45 min of operating time. The concentration of NaCl was 0.1 g/l with a 0.5cm spacing between the electrodes.

First and second order rate equation were applied to study adsorption kinetics. The adsorption process follows second order kinetic model with good correlation. The energy consumption was evaluated for the optimum operating conditions. It was in the range of 1.296 to 1.944 Kwh/m<sup>3</sup>. The overall expected increase in the operating cost of water treatment using membrane desalination facility (for example) will be about 20%.

**Keywords:** Boron removal, Electrocoagulation, Water treatment, Mg electrode, pH.

### الخلاصة

في هذا البحث استخدمت طريقة التخثير الكهربائي لمعالجة الماء الملوث بالبورون وباستخدام اقطاب انود من المغنسيوم كمختر واقطاب كاثود من الحديد المقاوم . خلية تخثير بحجم 1.5 لتر قد استخدمت ايضا في العمل. تم دراسة العديد من العوامل المؤثرة على عملية معالجة المياه الملوثة بالبورون وكانت هذه العوامل كالتالي: الدالة الحامضية، كثافة التيار، التركيز الاولي للبورون، تركيز كلوريد الصوديوم، المسافة بين الاقطاب، نوعية الاقطاب، وتركيز ايونات الكربونيت. ومن النتائج تبين ان الازالة المثلي كانت 91.2% و قد تحققت بزمان 45 دقيقة بدالة حامضة تساوي 7 و كثافة تيار قدرها 3 ملي امبير لكل سنتيمتر مربع وباستخدام اقطاب المغنسيوم. وتركيز كلوريد صوديوم يساوي 0.1 ملغرام / لتر ومسافة 0.5 سنتيمتر بين الاقطاب. كما وقد تم دراسة كلفة استهلاك الطاقة في الظروف المثلى للازالة ، وقد كان استهلاك الطاقة يتراوح بين 1.296 الى 1.944 كيلو واط . ساعة/ متر مكعب

## 1. Introduction

Recently boron has come to the forefront as a possible drinking water contaminant (WHO, 2008). Due to the increasing demand of water in both potable use and for Irrigation, coupled with a decrease of suitable water sources, suppliers have to use alternatives such as sea water. By using those alternative sources more trace contaminants start to appear in the final product. One of these is boron. Boron (B), an inorganic compound, is a non-volatile metalloid that is ubiquitous in the environment in compounds called borates. Common borates include boron oxide, boric acid, and borax (USEPA, 2008). Boron could be released into the environment by both natural weathering processes and anthropic sources (Yonglan et al, 2008).

Concentrations of boron vary widely and depend on the surrounding geology and wastewater discharges. Boron compounds are used in the manufacture of a variety of industrial products such as glass and porcelain, wire drawing, leather production, carpets, cosmetics, detergents, food preservatives, photographic chemicals, fireproofing fabrics and weather proofing for woods (Nihal et al, 2004). During these processes many boron compounds are introduced into the environment as a waste.

Short and long term oral exposures to boric acid or borax in laboratory animals have demonstrated that the male reproductive tract is a consistent target of toxicity (WHO, 2008). According to the WHO and Iraqi drinking water guideline for 2009, boron levels in drinking water have to be limited to 0.5 mg/l.

There is no easy or simple method for the removal of boron from water and wastewater (Kabay, 2010). Technologies for boron removal include conventional and advanced treatment technologies such as, chemical precipitation, ion exchange, reverse osmosis (RO), adsorption with Activated carbon (AC), Electrodialysis (ED) and etc. These methods have disadvantages such as using large quantities of chemicals and generating large volume of sludge causing disposal problems. Therefore there is a need to

find more efficient method to remove boron from water.

In recent years, the level of fresh water flowing into Shatt Al-Arab from Euphrates and Tigris rivers has declined, so salt and boron containing-water from the Arabian Gulf has increasingly poured in. This resulted in a problem to the water treatment plants in the south of Iraq because they use conventional methods for water treatment which are not effective for boron reduction as previously mentioned.

Researches had been done to remove boron from water and wastewater using EC method with different types of electrodes materials. Nihal et al., 2004 investigated the feasibility of boron removal from wastewater using EC with aluminum electrodes. The process was examined under various factors in order to assess optimal operating conditions. They showed that boron removal by EC process depends on current density, initial concentration and time. Removal of 92-96% was achieved under a current density of 30 mA/cm<sup>2</sup>. Erden et al., 2007 provided a quantitative comparison of EC and Chemical Coagulation (CC) approaches based on boron removal. Comparison was done with the same amount of coagulant between EC and CC processes. Although, all operational parameters were same in EC and CC, boron removal efficiency between each treatment processes was a quite different. Boron removal efficiency for EC and CC were 94% and 24%, respectively. Subramanyan et al., 2010 optimized the process parameters for the removal of boron from drinking water by EC. The results showed that a maximum removal efficiency of 97.3% was achieved at a current density of 50 A/m<sup>2</sup> and pH of 7 using magnesium at the anode and stainless steel as the cathode.

This work aims to evaluate the effectiveness of EC process to remove boron from water using Magnesium/ St.St. electrodes and determine the effects of various operating parameters on the removal efficiency such as initial boron concentration, initial pH, current density, gap



between electrodes, sodium chloride concentration, and time.

## 2. Electrocoagulation Mechanism

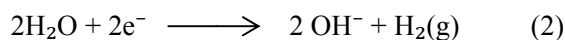
EC is a complicated process involving many chemical and physical phenomena that use sacrificial electrodes, such as Al, Fe and others, to supply ions into the water (Christos et al, 2010). In the EC process the coagulants generates in situ by dissolving electrically the consumable electrodes (Fe/Al). The metal ions generation takes place at the anode; hydrogen gas is released from the cathode (Lawrence, et al, 2007). In the EC process current is passed through a metal electrode, oxidizing the metal (M) to its ( $M^{n+}$ ) at the anode.



At the cathode side, hydrogen gas ( $H_2$ ) and the

hydroxyl ion ( $OH^{-}$ ) are generated by reducing

the water.



(Holt et al, 1999).

In the solution, the metal cations resulted from the anode oxidation combine with

hydroxyl ion ( $OH^{-}$ ) resulting from water to form

highly charged coagulant. In the case of Aluminum anode, the  $Al^{3+}$  reacts with  $H_2O$  to form  $Al(OH)_3$ , and in the case of magnesium anode the  $Mg^{2+}$  reacts with  $H_2O$  to form  $Mg(OH)_2$ .

The destabilization mechanism of the contaminant, particulate suspension, and breaking of emulsion may be summarized as follows (Christos et al, 2010).

- 1- Compression of the diffuse double layer around the charged species by the interactions of ions generated by oxidation of the sacrificial anode.
- 2- Charge neutralization of the ionic species in the wastewater by counter ions produced by the electrochemical dissolution of the sacrificial anode.
- 3- Floc formation.

## 3. Experimental Apparatus & Procedures

Fig 1 shows the EC cell consisted of a 1.5-L Plexiglas vessel. Magnesium electrodes of surface area ( $240\text{ cm}^2$ ) acted as the anode. The cathodes were stainless steel of the same size as the anode. A regulated direct current (DC) was supplied from a rectifier (5 A, 0–25 V).

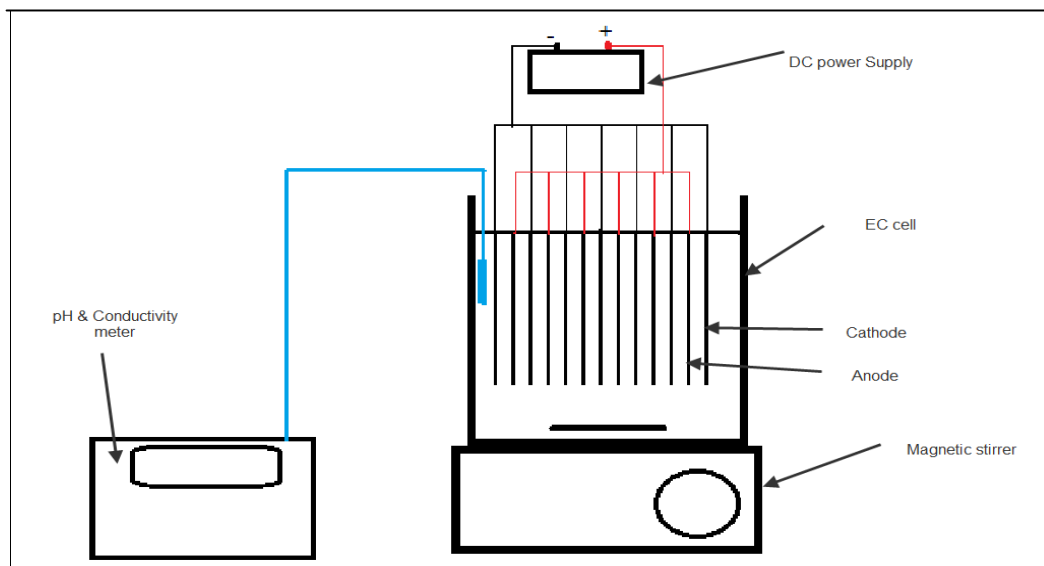


Figure 1: Schematic diagram of EC cell.

Boric acid  $\text{H}_3\text{BO}_3$  was dissolved in distilled water for the required concentration. The solution of 1.5 L was used for each experiment as the electrolyte. The pH of the electrolyte was adjusted, if required, with 1 mol/L HCl or NaOH solutions before adsorption experiments. Electrolytic cell with monopolar electrodes in parallel connections has been used with an interelectrode distance varying from 0.5 cm to 1 cm depending on each experiment conditions.

The magnesium electrode was weighed before and after each experiment to determine the amount of magnesium loss of each experiment. Before each experiment, the conductivity of the solution was adjusted with NaCl. During the experiments, the solution in the EC unit was stirred at 120 rpm by a magnetic stirrer with an Initial temperature of 22 °C.

Each run was timed starting with the DC power supply switching on. During the experiments, anodic dissolution occurred and hydrogen gas was produced at the cathode. Samples of 10 ml were taken during each experiment at different time to be filtered and then analyzed using atomic absorption spectrometer. Samples were analyzed at the civil Engineering labs at Dalhousie University in Canada. Each sample was taken from a distance between two electrodes and at fixed depth. After each run, the electrodes were washed and brushed then cleaned by ethanol to remove any solids accumulated on the electrode surface.

The operating conditions for each test run are summarized in Table 1. These operating conditions were optimized from preliminary tests and found out that they are the best conditions that give acceptable removal efficiency.





Table 1: Test runs plan summary for operating parameters.

Test run number	Test run description	pH	Boron conc. (mg/l)	Current density (mA/cm <sup>2</sup> )	NaCl conc. (g/l)	Spacing between electrodes cm	Carbonate conc. (mg/l)	Time (min)
1	Eff. of pH	3-10	5	3	0.1	0.5	0	0-120
2	Eff. of current	7	5	1-4	0.1	0.5	0	0-90
3	Eff. of B conc.	7	3-7	3	0.1	0.5	0	0-90
4	Eff. of NaCl conc.	7	5	3	0.01-0.2	0.5	0	0-90
5	Eff. of spacing	7	5	3	0.1	0.5-1	0	0-90
6	Eff. of carbonate	7	5	3	0.1	0.5	50-250	0-90

From other related research, it has concluded that the best stirring speeds are from 100 – 150. So, stirring speed of 120 rpm has kept constant during all the experiments.

#### 4. Results and Discussion

##### 4.1 Effect of Initial pH

pH of the solution plays an important role in the electrochemical and chemical coagulation process (Christos et al, 2010). In this study a set

of experiments were performed with initial pH in the range of (3-9), the test operating conditions are shown in Table 1. The maximum boron removal efficiency (99.59%) was obtained at pH of 7 within 120 min, which is neutral, from this it can be concluded that the majority of Mg coagulants are formed at this pH. The major

complex that is formed at this pH maybe due to formation of  $Mg(OH)_2$  which could be less soluble in water at pH of 7. However, that could be the reason of high boron removal percentage at this pH. This result is in agreement with the work of (Vasudevan et al, 2010). In which he indicated that the highest boron removal was obtained at pH of 7 because boron was present as  $B(OH)_3$  and the formation of  $Mg(OH)_2$  was high.

The results that show the effect of different pH values on removal efficiency of boron are shown in Fig 2

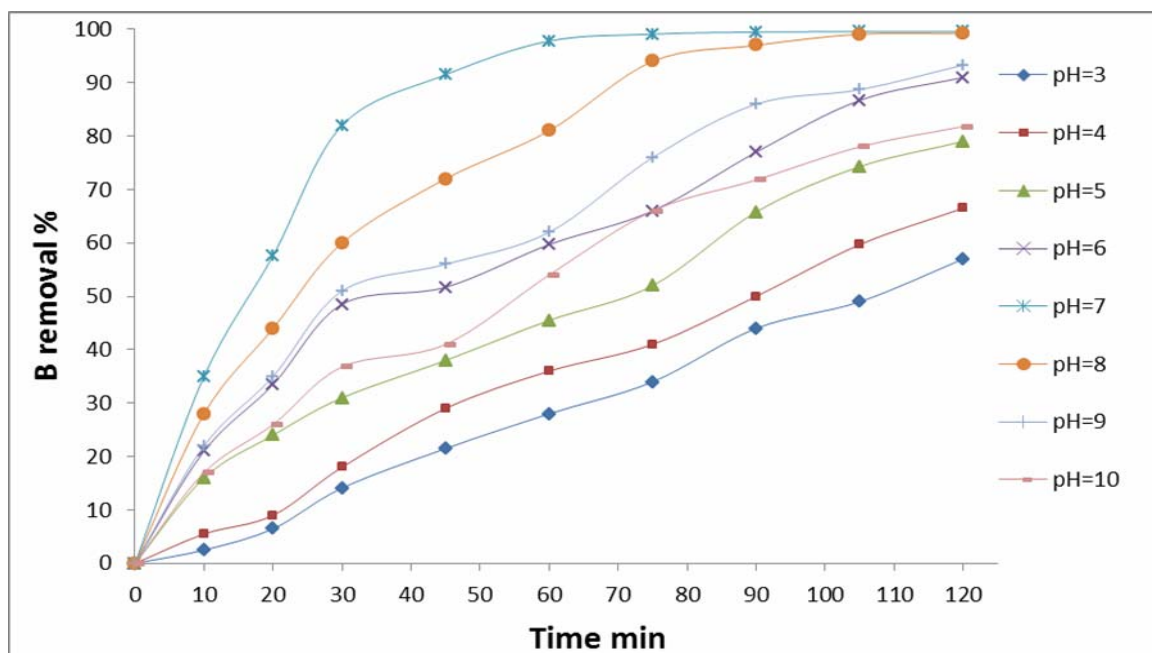


Figure 2: Boron removal efficiency with different pH values (Current density = 3mA/cm<sup>2</sup>, [B]= 5 mg/l, [NaCl] = 0.1 g/l, gap = 0.5 cm, T = 22 °C, and stirring speed = 120 rpm).

#### 4.2 Effect of Current Density

Current density is very important parameter that affects the EC process because it directly determines both coagulant dosage and bubble generation rates and strongly influences both solution mixing and mass transfer at the electrodes. So current density is the key operational parameter that affecting the system's response time and also influencing the dominant pollutant separation mode (Christos et al, 2010).

To examine the effect of current density on boron removal efficiency, a series of experiments were carried out with the current density being varied from 1 – 4 mA/cm<sup>2</sup>. The test operating conditions are shown in Table 1. The results are depicted in Figure 3.

From the Figure it can be seen that the boron removal efficiency increases with the increase of current density. At high current densities, the generation of Mg ions increases due to the increase of anodic dissolution, resulting in a greater boron removal rates, indicating that the

Adsorption depends up on the availability of binding sites for boron.

From Fig 3, it can be indicated that a current of 3mA/cm<sup>2</sup> gives B removal efficiency of 94%

which effectively reduces boron concentration to less than 0.5 mg/l. Any other increase in current density leads to increase in removal efficiency but it is not economically efficient due to high power consumption. A comparison between experimental and theoretical sacrificial magnesium anode consumption has been achieved by calculating the theoretical Mg loss from the anode using Faraday's equation and compared with those obtained experimentally. (Christos et al, 2010).

$$w = \frac{itM}{Nf}, \quad \text{Faraday's law} \quad (3)$$

Where:-  $w$  is the quantity of electrode material dissolved (g of M/cm<sup>2</sup>),  $i$  is the current density (A/cm<sup>2</sup>),  $t$  is the time in seconds,  $M$  is the relative molar mass of the electrode concerned, ( $M$  =56 for Fe, 27 for



Al, and 26.3 for Mg),  $N$  is the number of electrons in oxidation/reduction reaction, ( $N=2$  for Fe and Mg,  $N=3$  for Al), And  $f$  is the Faraday's constant, 96,500 C/mol.

The comparison between theoretical and experimental amount of Mg dissolved in the electrolysis is shown in Figure 4.

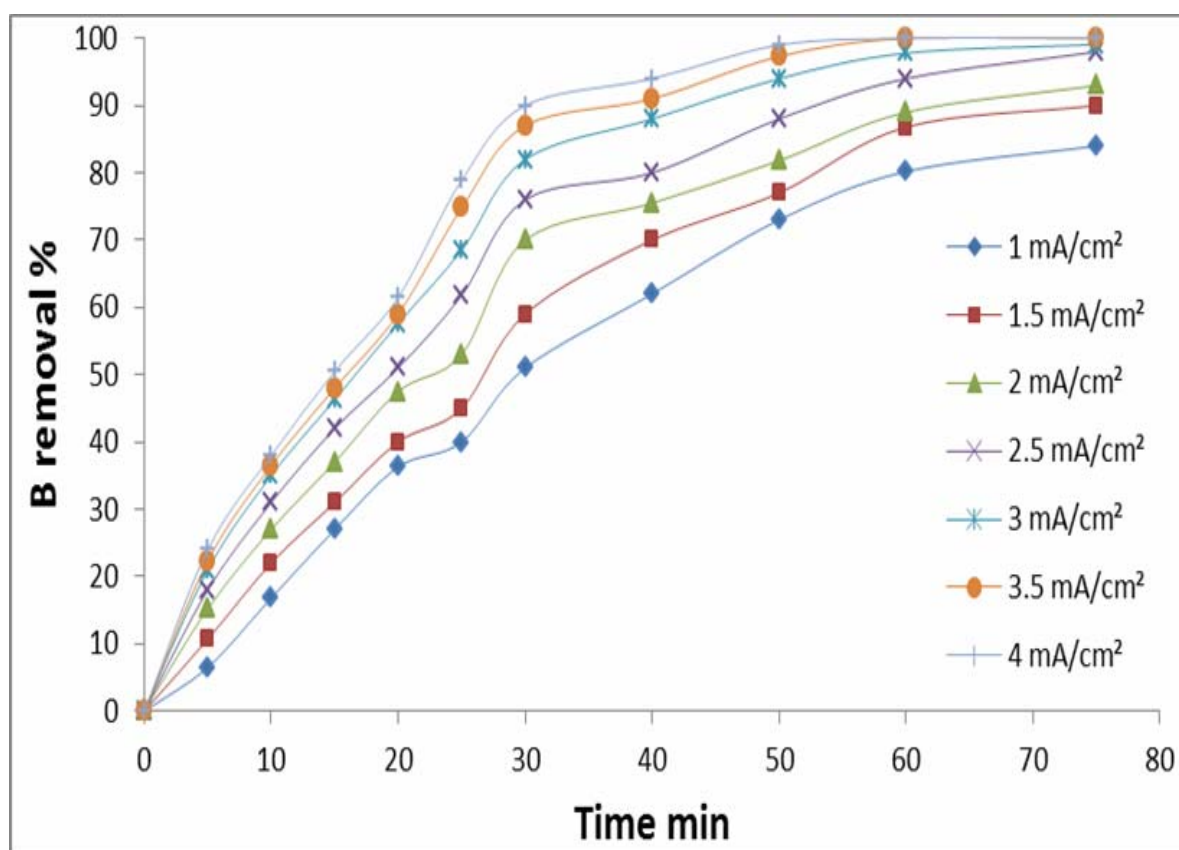


Figure 3: Effect of current density on boron removal efficiency. (pH = 7, [B] = 5 mg/l, [NaCl] = 0.1 g/l, gap = 0.5 cm, T = 22 °C, and stirring speed = 120 rpm).

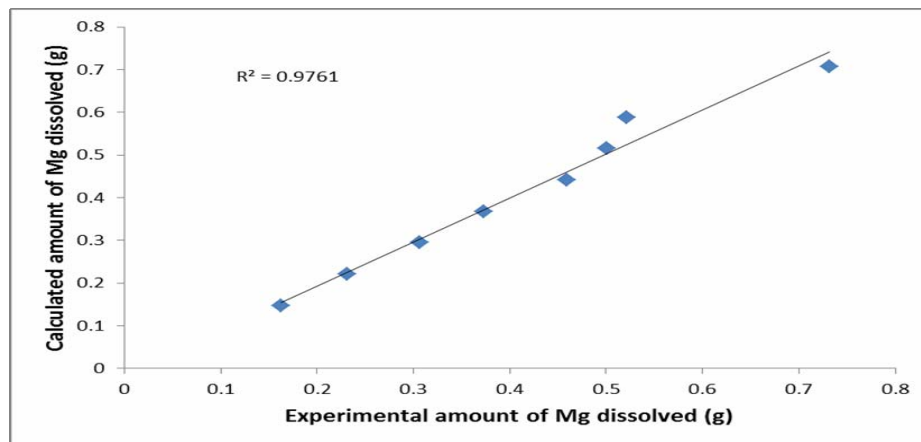


Figure 4: Measured Vs. calculated amount of Mg released from the anode

#### 4.3 Effect of Initial Boron Concentration

The effect of initial boron concentration on boron removal was examined with solutions of boron concentrations ranging from 3-7 mg/l. The other test operating conditions are shown in Table 1. Fig 5 shows the boron removal efficiency with time for different initial boron Concentrations. From the results it can be seen

That boron removal efficiency decreased with increasing boron concentration. This can be explained as follows; although the same amount  $Mg^{2+}$  passed to solution at the same current density for all boron concentration,  $Mg^{2+}$  was insufficient for solutions of higher B concentration.

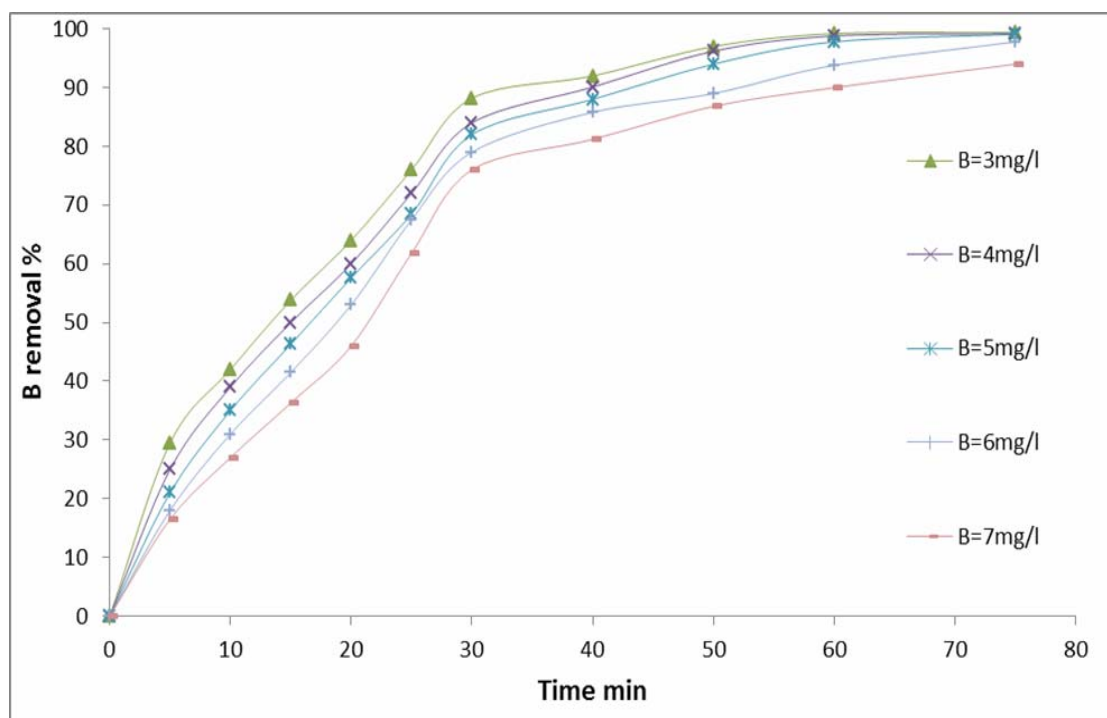


Figure 5: The Effect of initial boron concentration on Boron removal efficiency. (pH = 7, current = 3mA/cm<sup>2</sup>, [NaCl] = 0. 1g/l, gap = 0. 5cm, T = 22 °C, and stirring speed = 120rpm).

#### 4.4 Effect of Sodium Chloride Concentration

The effect of NaCl concentration on boron removal was examined with NaCl concentrations ranged between 0. 01 – 0. 2 g/l. the other test operating conditions is shown in Table 1. As expected, the obtained results showed that boron removal increased with

increasing concentration of sodium chloride because of the increase in solution conductivity.

In addition, the energy consumption decreased with increasing concentration of sodium chloride due to potential decrease under constant current density. The results obtained from the experimental work are shown graphically in Fig 6.

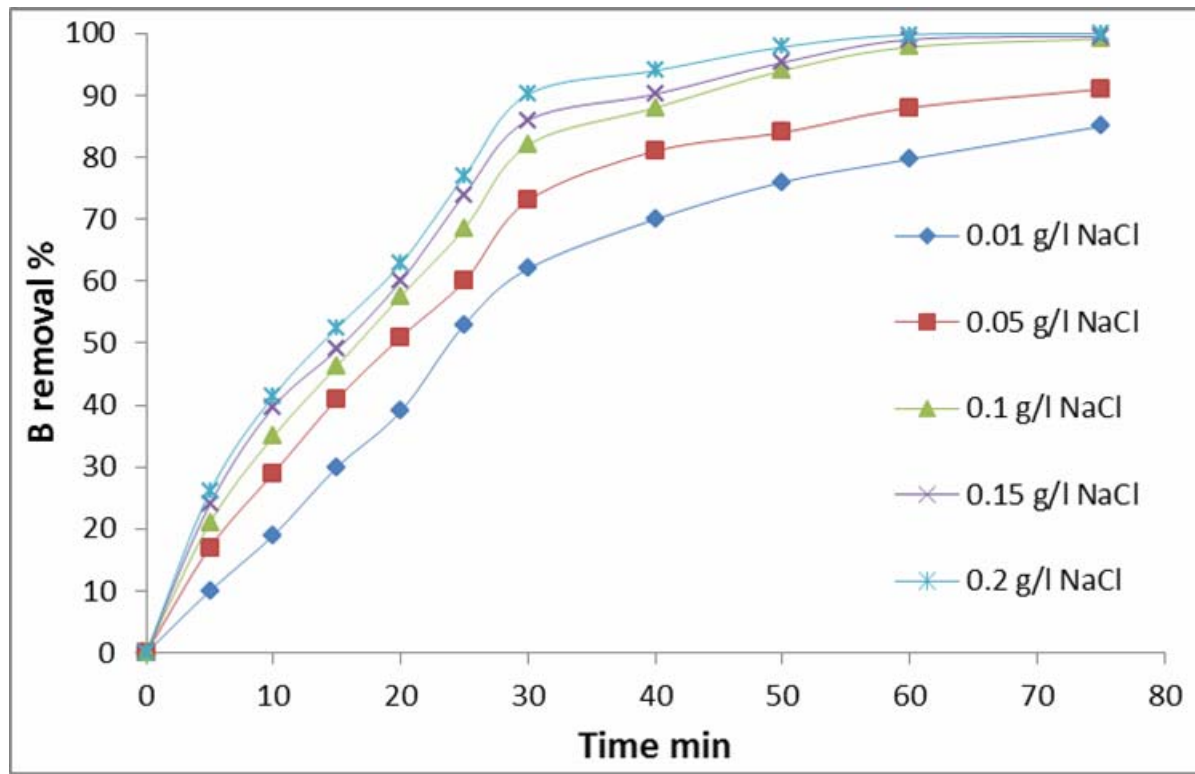


Figure 6: Relationship between B removal efficiency and time with different NaCl concentrations. (pH = 7, current = 3 mA/cm<sup>2</sup>, [B] = 5 mg/l, gap = 0.5 cm, T = 22 °C, and stirring speed = 120 rpm).

#### 4.5 Effect of Spacing between Electrodes

The effect interelectrode spacing on boron removal was investigated with spaces of 0.5, 0.75, and 1cm. The other operating conditions are shown in Table 1. It can be seen from Figure 7 that the removal efficiency increases with the decrease of space between electrodes while the highest removal efficiency of 99.1% was obtained at gap of 0.5 cm after 75 min. This can be explained that decreasing the space between electrodes results in low resistance through the solution which in effect results in increasing the rate of magnesium dissolution and

boron removal from the solution. On the other hand, decreasing the space could enhance the flotation process by limiting the generated bubbles in a narrow space which results in higher removal efficiencies.

Mg<sup>2+</sup> releases and consequently leads to more

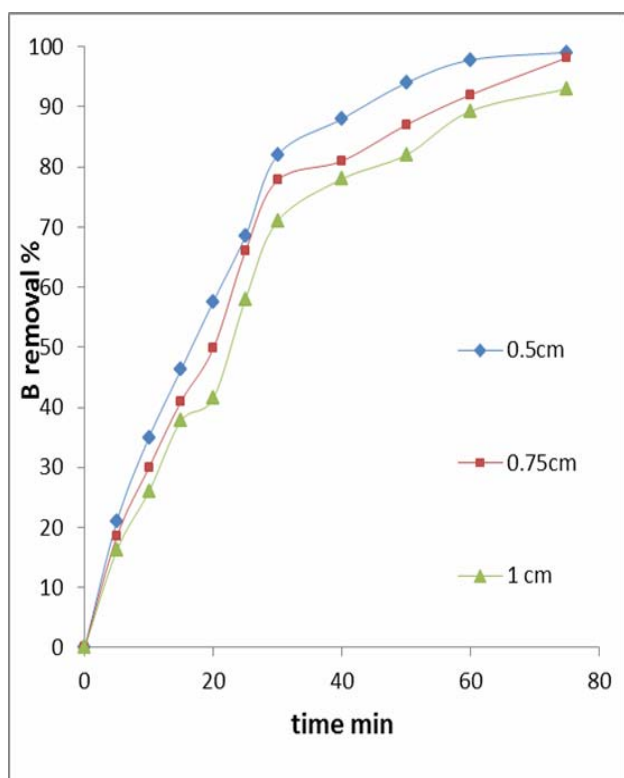


Figure 7: Effect of interelectrode spacing on boron removal efficiency

#### 4.6 Effect of Electrode Material

A set of experiments were carried out using aluminum electrodes with the same dimensions and active area of the magnesium electrodes to investigate the effect of different electrode material on boron removal efficiency. The operating conditions were maintained the same

As when magnesium electrodes were used in the previous experiments. The operating conditions were: current density of 3 mA/cm<sup>2</sup>, pH = 7, boron concentration of 5 mg/l, NaCl concentration of 100 mg/l, and interelectrode spacing of 0.5 cm.

Figure 8 shows that using Al electrodes is more efficient than Mg electrodes for the same operating conditions, although both electrodes reach the same maximum efficiency within 80 min. This could be happened because that the positive charge of Al ions (Al<sup>3+</sup>) is higher than the charge of Mg ions (Mg<sup>2+</sup>) which leads to more sorption affinity on pollutant colloids for Al ions.

The reason of using Mg electrodes instead of Al electrodes in the boron removal from drinking water is the high residual of aluminum in treated water, which can create health problems. In the case of Mg electrodes, there is no such disadvantage. The maximum allowed concentration of Al in drinking water is 0.2 mg/l while it is 100 mg/l for Mg (Iraqi specifications for drinking water, 2009).



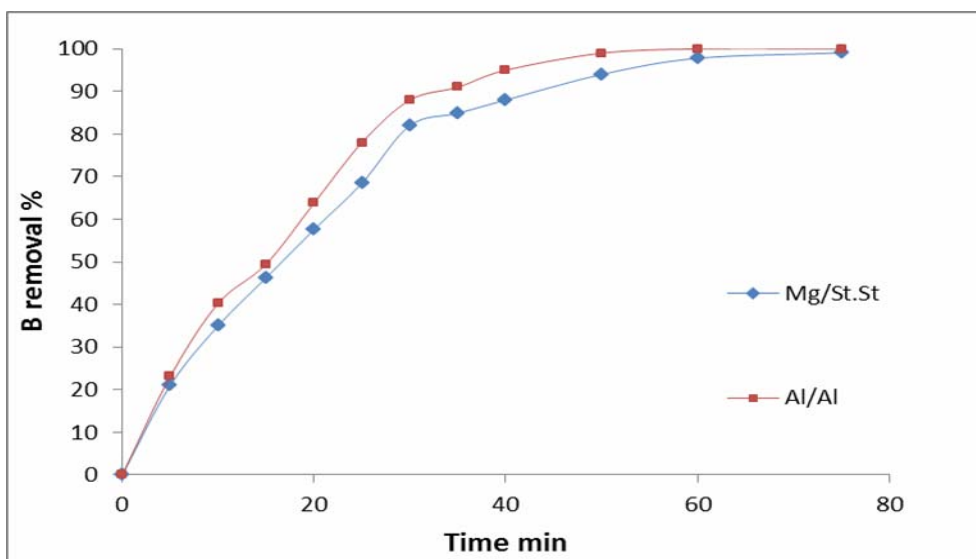


Figure 8: Effect of electrode material on boron removal efficiency

#### 4.7 Effect of Coexisting Anions (Carbonate).

To investigate carbonate anions on boron removal a set of experimental series were conducted with different carbonate concentrations of 50, 100, 150, 200, and 250 mg/l. the other operating conditions are shown

in Table 1. Figure 9 shows the effect of different carbonate concentrations on boron removal efficiency. The results indicate that carbonate anions have a significant effect on boron removal efficiency. This could be due to passivation of the anode and reducing dissolution of the anode.

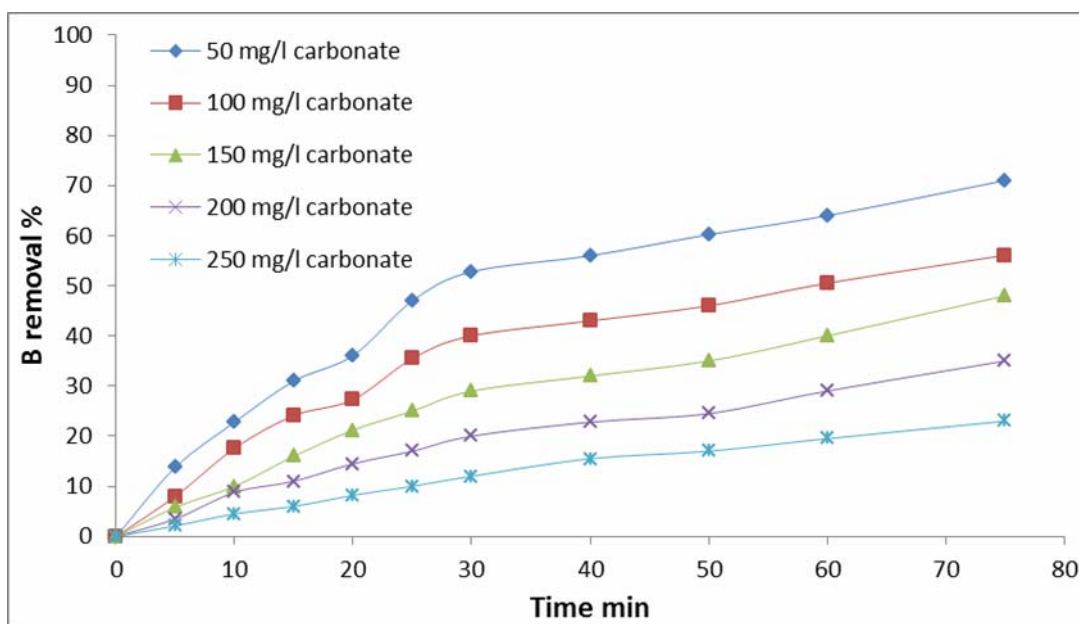


Figure 9: Effect of different carbonate concentration on B removal efficiency



#### 4.8 Studies of Adsorption Kinetics

The kinetics of adsorption of boron is analyzed using first-order and second-order Lagergen rate equations. (Azizian, 2004).

The pseudo-first-order rate equation is

$$\frac{dq}{dt} = k_1 (q_e - q) \quad (4)$$

Integrating Eq. (4) for the boundary conditions  $t = 0$  to  $t = t$  and  $q = 0$  to  $q = q$  gives

$$\ln \frac{(q_e - q)}{q_e} = -k_1 t \quad (5)$$

Where:  $q$  and  $q_e$  are the grams of solute sorbed per gram of sorbent at any time and at

equilibrium, respectively, and  $k_1$  is the rate

constant of first-order sorption.

Another model for the analysis of sorption kinetics is pseudo-second-order. The rate law for this system is expressed as

$$\frac{dq}{dt} = k_2 (q_e - q)^2 \quad (6)$$

Integrating Eq. (6), for the boundary conditions  $t = 0$  to  $t = t$  and  $q = 0$  to  $q = q$ , gives

$$\frac{1}{(q_e - q)} = \frac{1}{q_e} + k_2 t \quad (7)$$

Where:  $k_2$  is the pseudo-second-order rate constant of sorption.

Equation (7), can be rearranged to obtain a linear form,

$$\frac{t}{q} = \frac{1}{k_2 q_e^2} + \frac{t}{q_e} \quad (8)$$

The amount of boron adsorbed at equilibrium and the first-order rate constant ( $k_1$ ) were calculated from the slope of the plots of  $\ln \frac{q_e - q}{q_e}$  versus time ( $t$ ). It was found that the calculated  $q_e$  values do not agree with the experimental  $q_e$  values.

To investigate the adsorption of boron using Lagergen second-order equation,  $t/qt$  versus time were plotted in Figure 10. The second order kinetic values of  $q_e$  and  $k_2$  were calculated from the slope and intercept of the plots  $t/qt$  vs.  $t$ .

Table 2 gives the computed results from first- and second-order kinetic models. For the second-order kinetics model the calculated experimental amount of boron adsorbed at equilibrium values agree better than those of the first order kinetic model, indicating that adsorption follows more closely the second-order kinetic model.

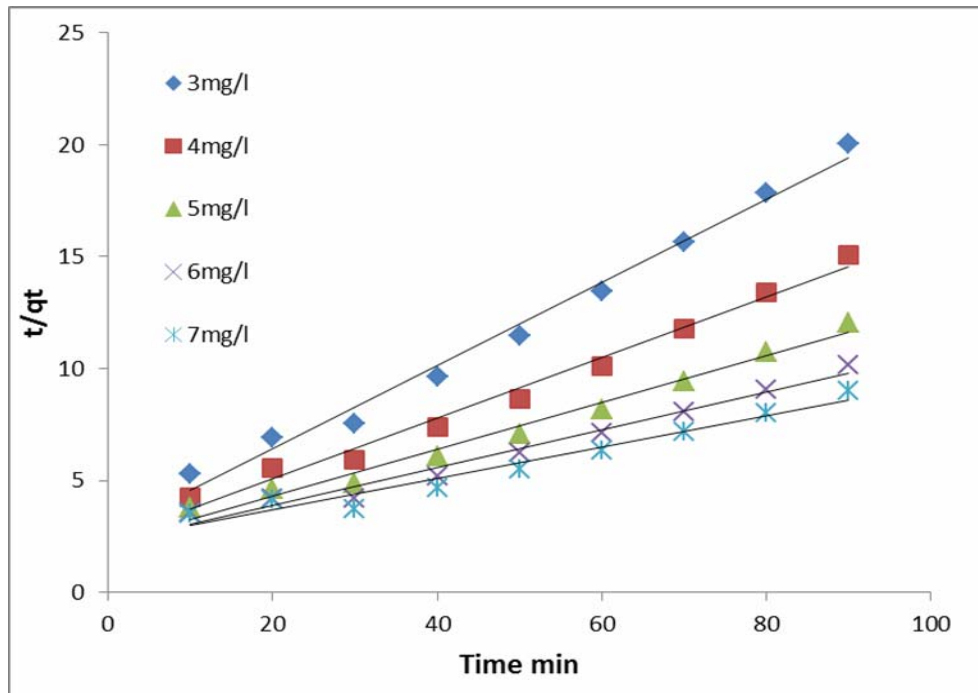


Figure 10: Second order kinetic model plot for different concentration of boron.

Table 2: Comparison between experimental and calculated  $q_e$  values for different initial boron concentrations in first and second-order adsorption isotherm.

B conc mg/l	$q_e$ expt.	first order adsorption			second order adsorption		
		$q_e$ calc	$K_1$ 1/min	$R^2$	$q_e$ calc	$k_2 * 10^{-2}$ 1/min	$R^2$
3	4.4955	7.7428	0.0859	0.9873	5.379	12.85	0.9884
4	5.976	21.8	0.1064	0.9171	7.3964	7.693	0.9857
5	7.4625	16.1213	0.08198	0.9768	9.5877	4.907	0.9822
6	8.874	15.8635	0.06747	0.9391	11.8906	3.1894	0.9771
7	9.9855	18.16	0.06632	0.9404	14.2247	2.162	0.9561

#### 4. 9 Study of Cost of EC Process

The energy consumption was evaluated for the optimum operating conditions that obtained from the tests shown before.  $E_c$  (Kwh/m<sup>3</sup>) is calculated from the following equation. (Al Gurany, 2009).

$$E_c = \eta I R t / 1000V \quad (9)$$

Where,  $\eta I R$  is the potential drop across the solution (V),  $I$  is the electrolysis current (A),  $t$  is the electrolysis time (h),  $V$  is the volume of the solution treated (m<sup>3</sup>).

For current consumption of 3 mA/cm<sup>2</sup> (0.72 A in this thesis), voltage of 5.4 V, cell volume of 1.5 l, and 45 min operating time, the  $E_c$  is 1.944 Kwh/m<sup>3</sup>. If electric cost is estimated to be 0.06 \$/kWh, then each m<sup>3</sup> will cost extra 11 cents for only the electric consumption. There are also other costs, such as sludge movement, magnesium material costs, maintenance, etc.



The overall expected increase in the operating cost of water treatment using membrane desalination facility (for example) will be about 20%. Water samples were taken from two water treatment plants at Shat Al-Arab then these samples were tested. The results showed that the treated water comes from the treatment plants has high salinity reaches up to thousands of mg/l. Although water salinity is not preferred in drinking water, it enhances the EC process by increasing the solution conductivity which leads to less treatment cost by reducing the operating time. Fig 11 shows how more salty water gives higher removal efficiencies.

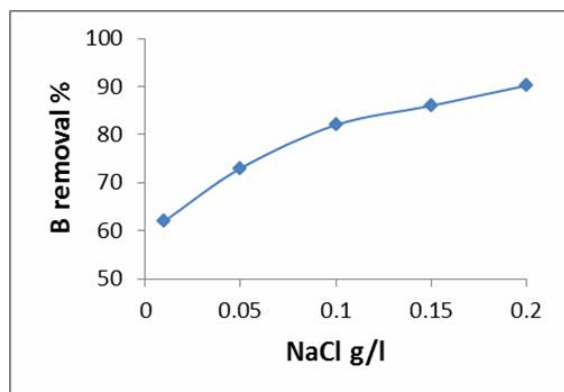


Figure 11: The effect of NaCl concentration of B removal efficiency (30min)

This Figure shows that using a concentration of 200 mg/l of NaCl instead of 100 mg/l gives 90.2% removal efficiency at 30 min. This removal efficiency reduces B level from 5 mg/l to 0.49 mg/l, which is within the drinking water guidelines. So that, using 200 mg/l NaCl reduces the cost of EC process by time reduction. Operating time of 30 min gives Ec equal to 1.296 Kwh/m<sup>3</sup>. In this case the EC cost will be 7.7 cents instead of 11 cents for only the electric consumption.

## 5. Conclusions

Experiments have been carried out to determine the best operating conditions which give an acceptable boron removal with the lowest time and cost.

1- The results showed that the optimized boron removal efficiency of 91.5% was achieved at a current of 3mA/cm<sup>2</sup>, pH of 7, NaCl = 0. 1g/l, time = 45min, electrode spacing = 0.5cm, at a stirring speed of 120rpm, and temperature equal to 22°C, using magnesium electrodes as anode and stainless steel electrodes as cathode.

2- Although, aluminum electrodes gave more boron removal efficiency than magnesium electrodes, the use of magnesium electrodes in drinking water treatment is preferred because of the high Al ions residual in the treated water which may lead to some health problems.

3- It was clearly indicated that the boron removal efficiency of 91.5% was achieved from the generation of magnesium hydroxide in the EC cell. The magnesium hydroxide removes boron presents in the water and reduces the boron concentration to less than 0.5 mg/l, and makes it within the acceptable range for drinking water as mentioned by WHO guidelines for boron.

4- The effect of carbonate anions concentration on boron removal also was studied and the result showed a significant effect on the removal efficiency when the carbonate concentration is high, which could be caused by the passivation of the anode causing reduction in anode dissolution.

5- From an experimental study of boron adsorption kinetics, it was found that the boron adsorption process follows Lagerange second-order kinetics rather than first-order kinetics.



## References

Al Gurany, A. J. M., Separation of oil from O/W emulsion by electroflotation technique, MSc. Thesis, University of Baghdad, 2009.

Christos C. and G. Chen, Electrochemistry for the Environment, Springer, New York, 2010, pp. 245-262.

Iraqi specifications for drinking water, 2009.

Kabay, N., Boron in seawater and methods for its separation — A review, Desalination 2010, doi:10. 1016/j. desal. 2010. 05. 033

5. Lawrence K. , Yung Tse, Nazih K. , Advanced Physicochemical Treatment Technologies, Humana Press, Totowa, New Jersey, 2007, pp. 64-65.

Nihal Bektas, S. Oncel · H. Y. Akbulut, A. Dimoglo, Removal of boron by electrocoagulation, Environ Chem Lett, 2004, pp. 2:51–5.

Peter Holt, Geoffrey Barton, Cynthia Mitchell, EC as a wastewater treatment, The Third Annual Australian Environmental Engineering Research Event. 23-26 November Castlemaine, Victoria, 1999.

Saeid Azizian, Kinetic models of sorption: a theoretical analysis, Journal of Colloid and Interface Science 276 2004, pp. 47–52.

Subramanyan Vasudevan, Jothinathan Lakshmi, Sagayaraj Margrat Sheela, Optimization of the process parameters for the removal of boron from drinking water by electrocoagulation – a clean technology, J Chem Technol Biotechnol (2010), DOI 10. 1002/jctb. 2382.

USEPA. 2008. Regulatory Determinations Support Document for Selected Contaminants from the Second Drinking Water Contaminant Candidate List (CCL 2). EPA Report 815-R-08-012. June.

World Health Organization, Guidelines for Drinking-Water Quality, 3rd ed. , pp. 313, 314; Geneva, 2008.

12. Yonglan Xu and Jia-Qian Jiang, Technologies for Boron Removal, Ind. Eng. Chem. Res. 2008, 47, pp. 16-24.

13. Yilmaz A. E., Recep Boncukcuoğlu, Muhtar Kocakerim M., A quantitative comparison between electrocoagulation and chemical coagulation for boron removal from boron-containing solution, Journal of Hazardous Materials, 2007, 149, pp. 475–481.





**Number 11**

**Volume 18 November 2012 Journal of Engineering**







:

:\_\_\_\_\_

:

## **The Influence of Politics on Architectural Thought**

### **A Descriptive and Analytical Study of the Effect of Political Ideology on the Achieved Architecture (Berlin City as an Example)**

**Prepare By:**

**DHIRGHAM MIZHER KAREEM ALOBAYDI**

[dhirghamalobaydi@yahoo.com](mailto:dhirghamalobaydi@yahoo.com)E-Mail:

#### **Abstract:**

The research investigates the political effect and its directions on the architectural thoughts and its achievements and how can this political system affect all fields of life in communities including architectural urban design. The problem of the research lies in the ambiguity effects of the ideological national directions of the Nazi Party on the architecture and urban design of the city of Berlin, then determining the aims of the research to discuss the concepts of politics and architecture and their relation to the way of thinking that plays a role in the process of design that works on property and achieving the suitable urban environments for those communities. After that, the Nazi's party's thought would be studied and analyzed, its concepts, public beliefs and its relation with renewing the city of Berlin as an example, to finish with introducing the conclusions.

Change

Political Decision

Urban Design

:\_\_\_\_\_

.Design

Symbolic

Metabolism

1. \_\_\_\_\_ :

1.1 :

( 2000 25 ).

( 25 ).

( : )

(...



3.1 \_\_\_\_\_ :

4.1 \_\_\_\_\_ :

5.1 \_\_\_\_\_ :

!!

( )

:

2.1 \_\_\_\_\_ :

( ) ...

( )

6.1 \_\_\_\_\_:

2000 )

.(131-129

:

.

.

2000 )

...

.(19

!

.

:

:

:

.

.

.

.

.



( )

:( )

2000 )

.(107

:

.(33 2000 )

( )

( )

:( )

( 2000 52-53 ).

( 2000 54 ).

:"

"

( )





:

•

( 2000 132-134 ) .

(We shape

Our Building Thereafter - They Shape Us)

( 1985 17-19 ) .

:

•

(

R.Dripps

R.Dripps

( )

( )

(Dripps, 1996,

p.107, 18)

7.1 :

:

•

“The

idea of man-made world”

:

” ”

( )

.(Crowe, 1995, p.233)

” :

”

” :

( )

”( )

:

.

2000 )

(Positivist)

.(103



( 2000 103-105 ).

· :

·

·  
( )

·

·

-

( )  
( )

·

( )

·

!!

Metabolism

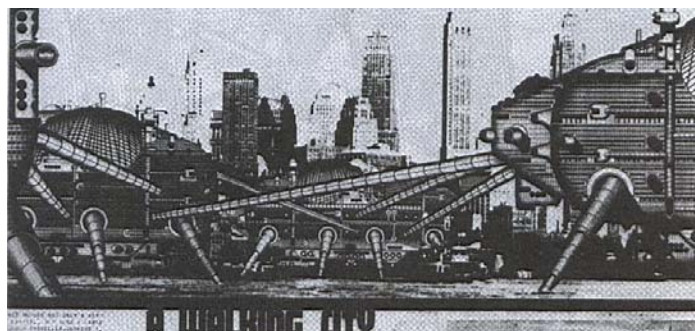
Osaka 1970 (1

(319-317)

(Jencks,1980,p.100-101).

.2.

.1.



(2)

1964 Herron للمعمار

(138 2002 ) :

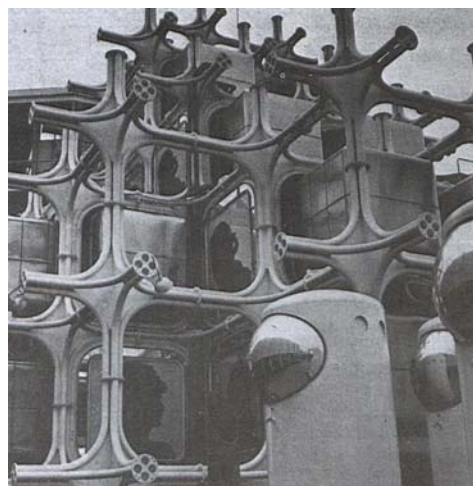
Walking City

(2 ) 1964 Ron Herron  
(137-135 2002 )

.Abstract Thinking

) "

.(335

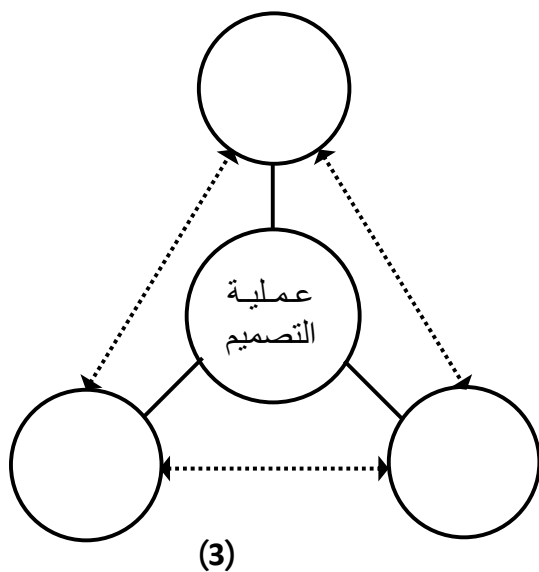


(1)

(74 2002 ) : 1970 Korokawa

( )

!



Design Problems

Dilemma

Troubles

2005 )

(4).

( ) :

( )

( )

(3 )

والتي تختلف من مدينة الى أخرى (شكل4). وللتقصي في هذا الموضوع بشكل اعمق واعتماداً على احد الامثلة المشهورة فيه.



(4)

(Wessling, 2010, p.14) :



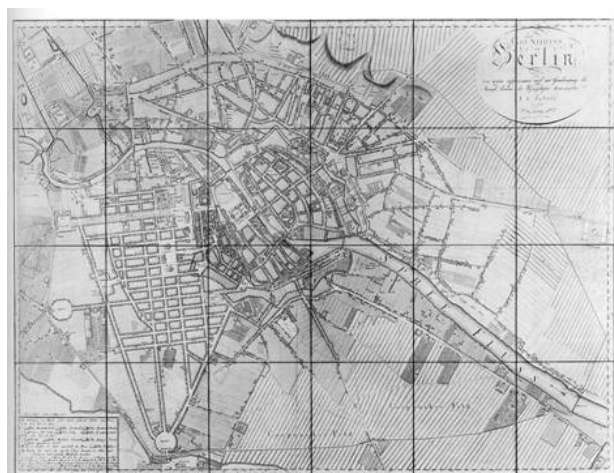
!

\_\_\_\_\_ ) .2

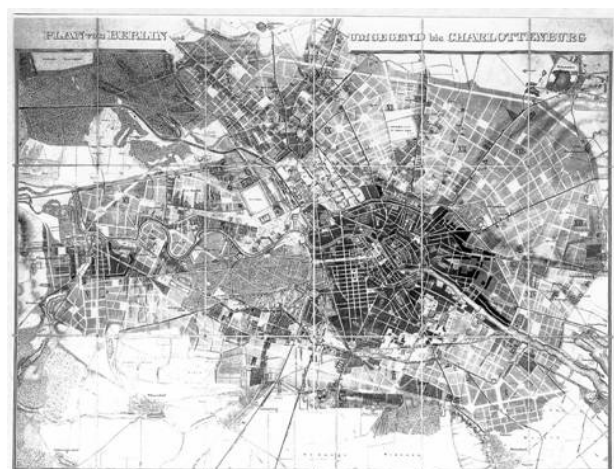
:( \_\_\_\_\_

:

1.2



(Hitler)



.(5 )

( )

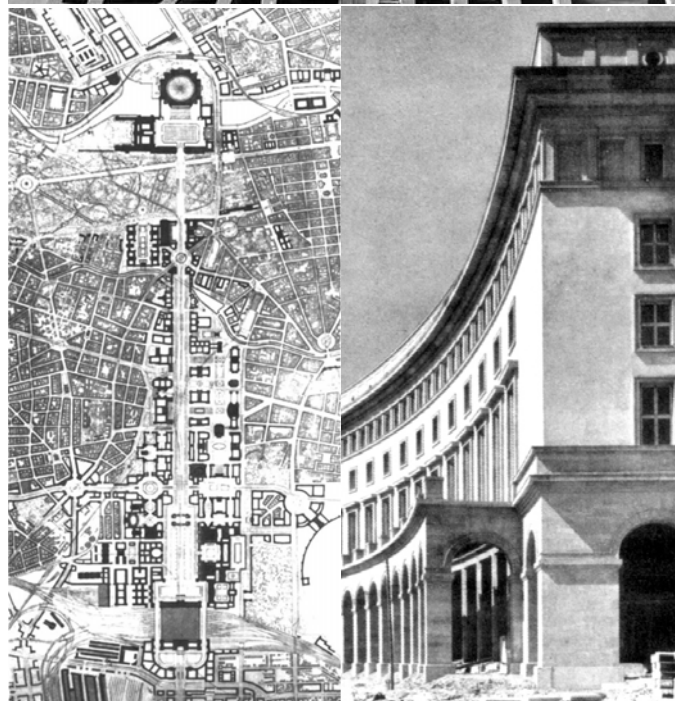
)

.(

(5)

(Wessling, 2010, p.10& 12) :





(6)

(Wessling, 2010, p.24) :

( )

(6 ) .



:

)

:(

.(Aryan )

Nazi Architecture, P.1-)

(3

:

:(

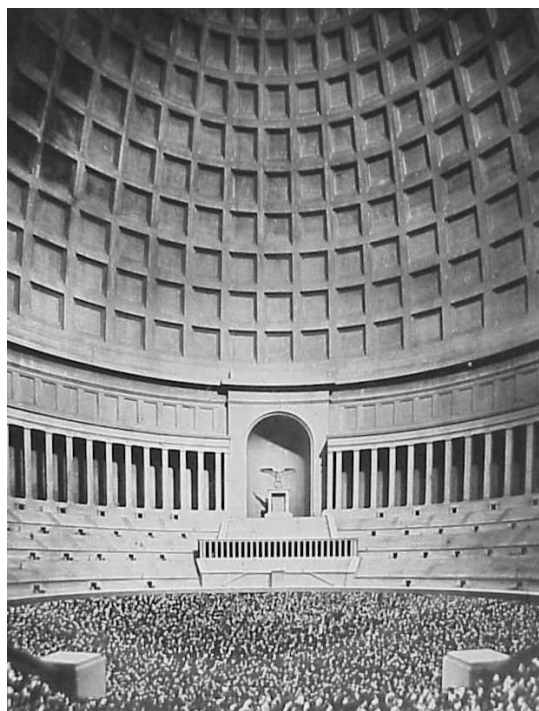
)

**THEATRICAL**

**:STAGE**

( )

270



(7)

Speaker

3.2 :

Speaker

)

Speaker

(

( - )  
( - )

:

:

350000

(7 ) ( )

.( )

.( )

( )



أثر السياسة على فكر العمارة دراسة وصفية تحليلية لتأثير الأيديولوجية السياسية على مُنجز العمارة، مدينة برلين إنموذجاً

Speer

( )

( )

( )

(Hitler)

.

!

.(8 )

: ( )

4.2

"

..."



(8)

**(2010 ) :**

Nazi Architecture, ) ( )  
:(P.1-3

## 5.2

•



( )  
(27) ( )

Speer Bogen

:

.

:



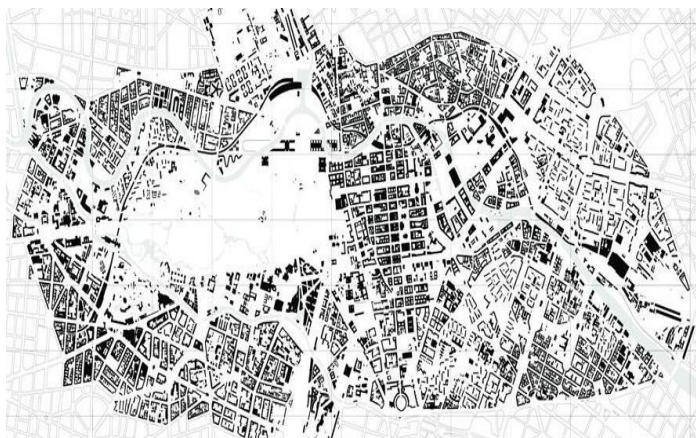
(9)

(9)

1993

(Wessling, 2010, p.106&108) :

!







(10)

1993

(Wessling, 2010, p.73&75) :

!!

.(10 )





... ( )

( )

: 2.3  
.1



.2

.4 \_\_\_\_\_ :

Design Process :

1.4 :

( )

.2005

.3

( )

.2000

.4

.2002

.1985

:

## 2.4

IV.Jencks, Charles, **Late Modern Architecture**, Academy editions, 1980.

V.Shane, Grahame, **Contextualism**, A.D. Architecture Design, No. 11, 1976.

VI. Wessling, Christoph, **THE BERLIN EXPERIENCE**, Reconstruction and urban development of the inner city since the Unification 1990, BTU Cottbus, Germany, 2010.

I.Article, **Nazi Architecture**, From Wikipedia, the free encyclopedia.

II.Crowe, Norman; **Nature And Idea Of A Man-Made World: An Investigation Into The Evolutionary Roots of Form And Order In The Built Environment**, the MIT press, London, England; 1995.

III.Dripps, R.D.; **The First House; Myth, Paradigm, and the Task of Architecture**; the MIT press; 1996.



## The Impact of Materials' Technology on Sustainability of Buildings

Assist. Lect. ASEEL ABD- ALHALEEM  
LATIF  
University of Baghdad  
College of Engineering  
Departement of Architecture Engineering  
[mmrreemm@yahoo.com](mailto:mmrreemm@yahoo.com)

Assist. Lect. HALA SHAMSI MOHAMMED  
ALDIWANI  
University of Baghdad  
College of Engineering  
Departement of Architectural Engineering  
[hala\\_aldywani@yahoo.com](mailto:hala_aldywani@yahoo.com)

### Abstract:

The evolution in materials' technology in the last decades resulted in interesting projects that aimed at preserving the environment and energy and reduce pollution. They have been taken the principles of environmental design as a basis for architectural thought, starting from the early stages of the design process ending in choosing appropriate building materials to achieve sustainable buildings, but these trying are limited in our local environment and there isn't demanded seriousness. The

research problem emerges in the ignorance of the environmental aspect (ecological system) when selecting building materials during design process to achieve sustainable buildings. The aim of this research is revealing the mechanisms of selecting building materials to improve the functional performance and reduce the negative effects on the environment and preserve its resources and the ecological systems as much as possible according to the following indicators: Embodied energy, recycling, durability; to assist architects and specific engineers in making decisions that have a significant impact in achieving sustainable buildings in the local environment and the possibility of application in Iraq .

**Research Keys: Materials' Technology, Ecological system, Embodied energy, Recycling, Durability.**



William Morris

" : 1892

"

"The subject of Material

( 2003 69 83 ) is clearly the foundation of Architecture"

(Randall, 2006, P.67)

( 2 )

( )

).

( 2009 47 )

" :

((1) )

2

( 2009 43 )



)

(6 -5 2009 ). (



:

■



■

( )

( )

:

:

(Structural potentialities)

-

:

■

■

-

(Applicable potentialities)

-

-

(Cladding potentialities)

-

:

( 1997 ص62 )

(Esko, 2002, .

P.1)

.( )

(Jones, .



2000, P.22)

حيث إن

%40

(Roaf etal, 2007, P.48 )

(Gunther, 1999, P.135) .

ولما

3

( 1989، ص9 )

" 1987

) "

(ص30

( )

4

(Esko, 2002, P.1)

( )

(Randall, 2006, P.67)

(  
(Us Green Building Council, 1996, P.183)

4  
(

3  
(Gro Harlem Brundth Land)  
(اللجنة العالمية للبيئة والتنمية، 1989، ص9)



:

:

■



■

■

■

■

( )

. (Roaf etal, 2007, P.50)

. (موشيت، 2000 ، ص135- 136).

– Embodied energy

(Roaf etal, 2007, P.48-)

– حيث

49



. (Roaf etal, 2007, P.50)

:



CO2

■

■

■

( )

:

.(Calkins, 2009, P.3-6)

. . . .

■

■

■

■

■

. (Roaf etal, 2007,P.49) .



LAC<sup>5</sup>

(None-Durable)

(Calkins, 2009, P.3-6)

8

(Jones, 2000, P.6)



Hydroelectric power

.CO2

:

-

-

-

-

-

(US Green Building Council 1996, P.185)

:

(Calkins, 2009, P.6-7)



)

(

:

-

)

(

-

**Embodied Energy**



<sup>5</sup> تقييم دورة الحياة (Life Cycle Assessment)



## ) Embodied Emissions

)

(

(Jones, 2000, P.6) .

.(

CO2

:

.

، (Roaf etal, 2007, P.50-51 )

The total primary energy that has to be sequestered from a stock within the earth in order to produce, transport, maintain and dispose of materials within a specified product, component, element or building .

(Pank, 2002, P.21)

## Gray Energy

Delivered energy

Primary energy

( )

:

- :Initial embodied energy

soft wood

- Recurring embodied

:energy (Roaf etal, 2007, P.53) .

○

-

-

.(1)

:

(2)

(Holtshausen, 2007, P.2)

، (2)

(Roaf etal, 2007, P.54-57)

**Recycling**



(Gunther, 1999, P.135)

Refurbishing

—

—

○

و (Roaf etal, 2007, P.55) ،



)

(Jones, 2000, P.6) .

(

• (Jones,2000,P.18)

( )

• (Holtshausen , 2007, P.8 ) .

( )

:  
 (USGreen Building Council, 1996, P.179)

(2)

Post consumer Material

Recovered industrial

process waste

Internally recycled materials from a  
 manufacturing process

( )

( )

**Durability**

(Holtshausen , ) .

•2007, P.7

(None-Durable)

Soft wood

6

. (Esko, 2002, P.1)

(Roaf etal, 2007, P.60-61)



:

■

)

(

(Us Green Building Council )

.

, 1996, P.180

:

■

.

.

(Roaf etal, 2007, P.59-60)

:



(

)



.

:

و

CO2

-

-

-

:

■

:

■

:

-

:

-

100°f

الى 400°f

:

-

Hard Wood

6

. (Roaf etal, 2007, P.60 )



:  
 - ( Calkins,2009,P.182) .  
 %40-%15  
 . %100  
 -  
 -  
 .  
 -  
 CO<sub>2</sub>  
 )  
 ( ( Kim, 1998, P.24) .  
 (Us Green Building Council, 1996, P.183) : -  
 rood stone  
 .  
 : ■  
 : -  
 .  
 (Calkins, 2009, P.180-184) .  
 . 100C : ■  
 : -  
 .  
 .  
 %80  
 :  
 - ( Ibid , P.179-181) .  
 : ■  
 -  
 350  
 (Holtshausen , 2007, P.5) .  
 : ■  
 ( Kim, 1998, P.24).

%70-50

(Us Green Building Council , 1996, P.180)

(Us Green Building Council, 1996, P.180-185)

( Kim, 1998, P.23).

CO2

7

80 MJ/Kg (Holtshausen , 2007, p.5) ،  
%8.5

CO2

%0.33

%27

(Holtshausen , 2007, P.4-5) .

CO2

(Us Green Building Council, 1996, P.180-185)

( )

<sup>9</sup>AIA

)

.(

(Roaf etal, 2007, P.58)

:

-

:

-

CO2

)

.(

(Roaf etal, 2007, P.59) .

-

:

■

:



(Energy Resource Center)

(Downey)

:

■

:

■

:

■

.1995

1957

(Us Green Building Council , 1996, P.180) .

:

■

:

■

(Roaf etal, 2007, P.58)

ومن خلال ماتقدم أعتد البحث على المنهج الوصفي التحليلي المقارن (جدول (3)) في المواد البنائية المنتخبة للدراسة وفق مؤشرات الطاقة المجددة ، إعادة التدوير ، المتانة ، ليتسنى دراستها وتحليلها على الجانب التطبيقي.

:

■

LEED

2009

LEED



5

AIA

.1998

:

■

:

-

<sup>8</sup>LEED

(Leadership in Energy and Environmental Design )<sup>8</sup>

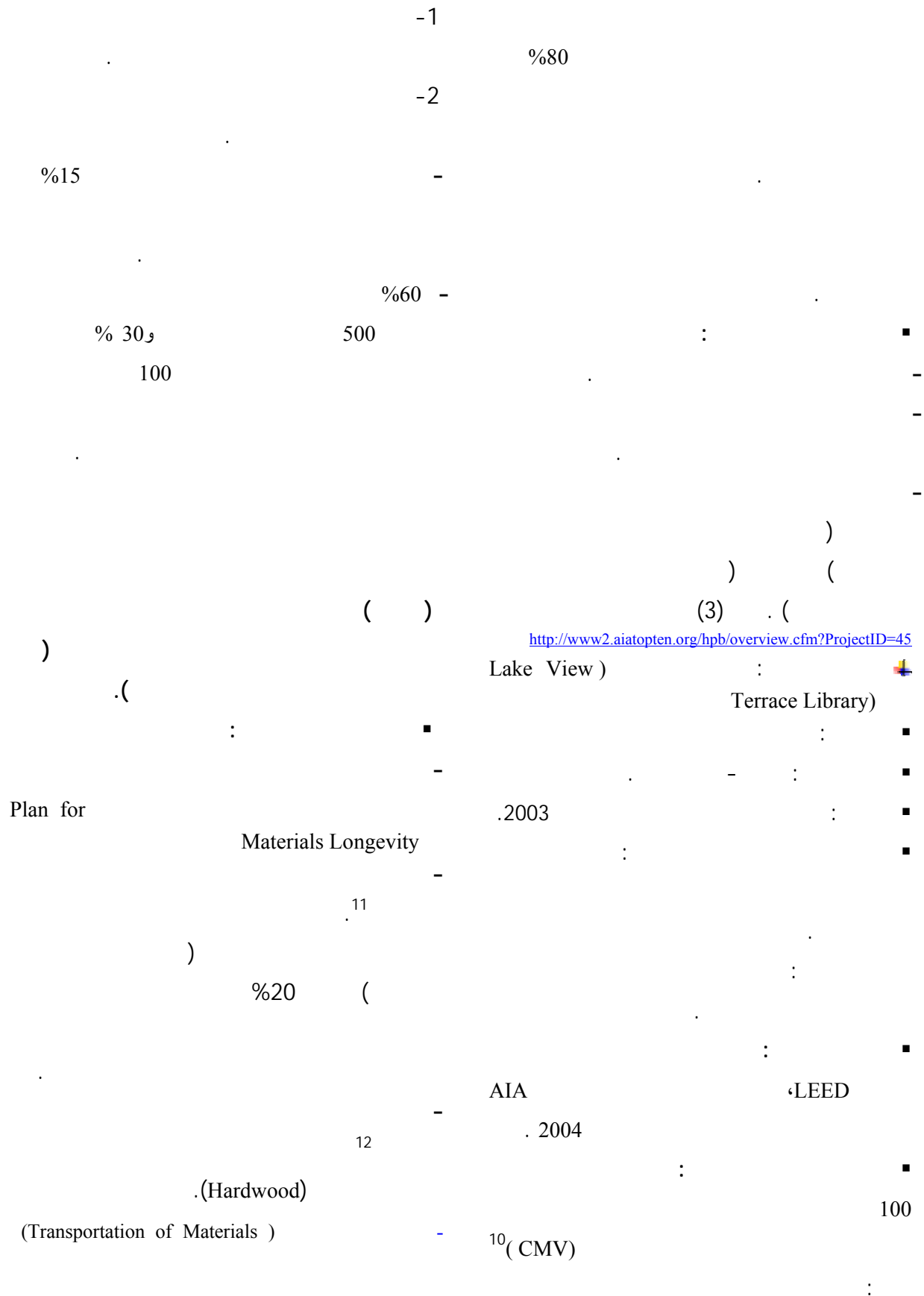
2000

1993

( 4 ) ، (5) . (Mendler&Odell,2000,P.20)

<sup>9</sup> The American Institute of Architects (المعهد الامريكي للمعماريين)





<sup>11</sup> Greenhouse Gas Emissions From Manufacture  
<sup>12</sup> Materials and Wildlife Habitat

<sup>10</sup> CONCRETE MASONRY UNITS



- :  
 91% 9%  
 2008 :  
 :  
 :  
 ( Charles Hostler Student center )  
 1951 - :  
 :  
 2008 :  
 :  
 -  
 ( )  
 -  
 -  
 -  
 2009 AIA  
 :  
 :  
 LEED  
 AIA ( )  
 2011  
 :  
 -  
 :  
 -  
 -  
 90% -  
 :  
 :  
 (5)  
<http://www2.aiatopen.org/hpb/images.cfm?ProjectID=1301>  
 :  
 (First Unitarian Society Meeting House)  
 ( Madison ) :  
 (Wisconsin)

(7)

[http://www2.ariatopen.org/hpb/grid2011.cfm?project\\_id=1950&section=16](http://www2.ariatopen.org/hpb/grid2011.cfm?project_id=1950&section=16)

❖

Modules

LEED

AIA

:

(5)

.1



■

(3 4)

(5 4 1)

■

(5)

.3

◆

■

...

(5 4 2 1)

■

.4

.(5 4 2)

■

:

■

◆

■

■

■

■

- 8) Mendler, Sandra & Odell, William; "the hok guide book to sustainable design", John Wiley and Sons Inc., USA, 2000.
- 9) Pank, Will – Girardet, Herbert & Cox, Greg "Tall Buildings and Sustainability", Corporation of London, 2002.
- 10) Randall, Thomas; "Environmental Design (An Introduction for Architects and Engineers)" Taylor & Francis e-Library, 2006.
- 11) Reddy, Venkatarama, "Sustainable building technologies", Department of Civil Engineering & Centre for Sustainable Technologies, Indian Institute of Science, Bangalore 560 012, India, Current Science, Vol. 87, NO. 7, 10 October, 2004.
- 12) Roaf, Sue - Fuentes, Mannel and Stephanic Thomas, "Eco House :A Design Guide", Oxford, UK 2007.
- 13) US green building Council, "sustainable Building Technical Manual", Public Technology Inc., 1996.

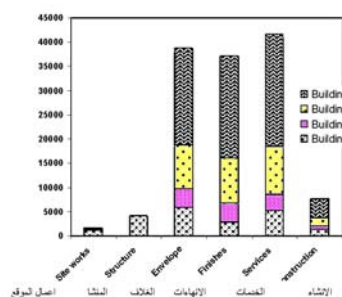
#### Internet Sites references

- 1) <http://www.usgbc.org/DisplayPage.aspx?CMSPageID=1721>
- 2) [http://www2.aiatopten.org/hpb/grid2011.cfm?project\\_id=1950&section=16](http://www2.aiatopten.org/hpb/grid2011.cfm?project_id=1950&section=16)
- 3) [http://www2.aiatopten.org/hpb/grid2011.cfm?project\\_id=1964&section=16](http://www2.aiatopten.org/hpb/grid2011.cfm?project_id=1964&section=16)
- 4) <http://www2.aiatopten.org/hpb/images.cfm?ProjectID=1301>
- 5) <http://www2.aiatopten.org/hpb/overview.cfm?ProjectID=289>
- 6) <http://www2.aiatopten.org/hpb/overview.cfm?ProjectID=45>

- (1) "
  - (2) "
  - (3) "
  - (4) "
  - (5) "
  - (6) "
- 2000
- 2003
- (142)
- 1989

#### English References

- 1) Calkins, Meg, "Materials of Sustainable Sites", John Wiley & Sons, Inc., Hoboken, New Jersey, Canada, 2009.
- 2) Esko Miettinen, "Sustainable Architecture with Stainless Steel" the conference creative architecture with Stainless Steel jointly organized by (Euro Inox, Brussels, Belgium, and Cedinox, Madrid, Spain), Barcelona on 12th March 2002.
- 3) Gumaste, Krishnakedar. S., "Embodied Energy Computations In Buildings", Advances in Energy Research (AER – 2006).
- 4) Gunther, Thomas Schmitz, "Living Spaces- Ecological Building and Design", Slovenia, 1999.
- 5) Holtshausen, H.J, "Embodied Energy and its impact on Architectural Decisions", Faculty of Art and, Design and Architecture, University of Johannesburg, 2007.
- 6) Jones, Anna Ray; "sustainable architecture in Japan- the green buildings of nikken sekkei", wiley academy, UK, 2000.
- 7) Kim, Jong-Jin, "Sustainable Architecture Module: Qualities, Use, and Examples of Sustainable Building Materials", 1998, The University of Michigan.



(2)

100

(Holtshausen , 2007, P.3 ):



(1)

(Calkins,2009,P.24)



- ( Energy Resource Center ) : (3)

<http://www2.aiatopten.org/hpb/overview.cfm?ProjectID=45> :



- ( lake View Terrace Library ) : (4)

<http://www2.aiatopten.org/hpb/overview.cfm?ProjectID=289> :



( Charles Hostler Student center ) : (5)

<http://www2.aiatopten.org/hpb/images.cfm?ProjectID=1301> :



( ) : (6)

[http://www2.aiatopen.org/hpb/grid2011.cfm?project\\_id=1964&section=16](http://www2.aiatopen.org/hpb/grid2011.cfm?project_id=1964&section=16) :



- (High Tech High Chula Vista) : (7)

[http://www2.aiatopen.org/hpb/grid2011.cfm?project\\_id=1950&section=16](http://www2.aiatopen.org/hpb/grid2011.cfm?project_id=1950&section=16):

(2)

( Holtshausen , 2007, P.4):

MJ/m <sup>3</sup> <sup>13</sup>	MJ/kg <sup>14</sup>	المواد البنائية
2030	0.79	( ) .1
2350	0.94	( ) .2
3180	1.30	( ) .3
2780	2.00	( ) .4
5170	2.50	.5
37210	8.90	.6
251200	32.00	.7
5720	10.40	.8
3770	117.00	.9
21870	8.10	.10
515700	227.00	.11

(1)

(Reddy ,2004,P.899 ):

Prior 8000 BC	/	.1
6000 BC		.2
4000 BC -8000 BC		.3
4000 BC		.4
3000 BC		.5
1300 BC		.6
1350 BC		.7
300 BC - 476 AD	( )	.8
1808 AD		.9
1824 AD		.10
1862		.11

(3)

المصدر: الباحثان

		15				
						.1
						.2
	%100					.3
						.4
						.5
			CO <sub>2</sub>			.6

LEED (5)

:

(Mendler&Odell,2005,P.20)

<http://www.usgbc.org/DisplayPage.aspx?CMSPageID=1721>

( )			LEED
%40	32-26	.1	
%60 -51	38-33	.2	
%80 - 61	51-39	.3	
%80	69-52	.4	

(4)

LEED (4)

( ) :

<http://www.usgbc.org/DisplayPage.aspx?CMSPageID=1721>

LEED Facts					
15	16	14	7	14	.1
5	5	12	2	5	.2
15	22	29	12	17	.3
9	10	24	14	13	.4
13	18	14	17	15	.5
/	/	10	/	/	.6
/	/	5	/	/	.7
5	5	4	5	5	.8
62	76	108	57	69	التقييم لا يتجاوز مجموع النقاط

( Randall,2006,P.72)

15



(6)

:

1.	مركز مصادر الطاقة كاليفورنيا امريكا	الاعتماد على السوق المحلية لجمع المواد البنائية التي من الممكن اعادة تدويرها واستعمالها.	استعمال المواد البنائية المحلية التي لا تحتاج الى عمليات تصنيع معقدة مثل الخشب.	للتقليل من استعمال الموارد الطبيعية فان 80% من المواد البنائية المستعملة هي مواد معاد تدويرها او من المواد القابلة للتدوير (مثل الحديد والواح الزجاج) كما أن الخشب المستعمل من الخشب المعاد تأهيله.	استعمال المواد ذات المتانة العالية مثل الحديد.	المستوى البرونزي (LEED) اختير كفضل عشرة مشاريع خضراء لعام 1998 من قبل AIA
2.	مكتبة البحيرة كاليفورنيا امريكا	أكثر من نصف المواد البنائية من مواد بنائية محلية مثل شجر البابو بدلاً من الخشب الصلب لتقليل كلفة النقل ،استعملت مواد بنائية محلية تم تصنيعها في البيئة المحلية.	استعمال الوحدات البنائية الكونكريتية وأدخل مادة الرامد المتطاير (أحدى مخلفات عمليات التصنيع) بنسبة 20% بدلاً من السمنت البروتلاندي للتقليل من عمليات التصنيع للتقليل من انبعاث CO2.	استعمال مواد بنائية معاد تصنيعها بنسبة 15% من المواد المستعملة مثل الحديد	عمر المبنى المصمم له 100 سنة لذلك تم اختيار مادة الكونكريت لبناء الهيكل واختيار مواد بنائية متقاربة في أعمارها الافتراضية (وهو عامل مهم لتقليل من كلفة أعمال الصيانة)	المستوى البلاتيني (LEED) اختير كفضل عشرة مشاريع خضراء لعام 2004 من قبل AIA
3.	مركز طلابي بيروت لبنان	اختيار المواد البنائية من مصادر محلية مثل الحجر.	استعمال المواد البنائية المحلية مثل الحجر.	_____	اختيار مواد بنائية ذات عمر افتراضي كبير وذات متانة عالية مثل الكونكريت والحجر وذات ديمومة عالية مثل الألمنيوم.	اختير كفضل عشرة مشاريع خضراء لعام 2009 من قبل AIA
4.	دار للاجتماعات ماديسن ويسكونسن	اعتماد المواد البنائية المحلية والمصنعة محلياً. استعمال أخشاب أشجار الصنوبر والحجر المتوفر محلياً في الموقع .	اعتماد مواد منتجة محلياً مثل الخشب والحجر ولا تحتاج الى عمليات تصنيع معقدة.	استعمال مواد سليبوزية للعزل من مواد معادة 90% من مخلفات الموقع وضع لها برنامج لإعادة التدوير واستعمالها مرة أخرى.	التصميم لدورة حياة طويلة للمبنى باعتماد المواد ذات المتانة العالية مثل الخرسانة والهيكل الحديدية.	المستوى الذهبي (LEED) اختير كفضل عشرة مشاريع خضراء لعام 2011 من قبل AIA
5.	مبنى تعليمي كاليفورنيا أمريكا	استعمال المواد المحلية في معظم أجزاء المبنى مثل الخشب.	استعمال المواد المحلية بنسبة كبيرة اعتماد الأبعاد المقيسة للحد من القطع الثالفة الناتجة من القطع ،استعمال المواد ذات الإداء الصحي والبيئي العالي مثل منتجات الخشب والهيكل الحديدية المقيسة.	استعمال المكونات القابلة لإعادة الاستعمال ، والهيكل المعادة . اعتماد الوحدات ال متكررة المقيسة M AODULES ، إعطاء فرصة لتوفير الوقت وتقليل الأعمال الانشائية في الموقع ، إضافة الى إمكانية التفكيك بسهولة واستعمالها مرة أخرى ، استعمال الهياكل الحديدية المقيسة.	صمم المشروع لدورة حياة 100 سنة أو أكثر لذلك استعملت المواد ذات متطلبات الصيانة الأقل مثل الطوابق الخرسانية و الهياكل الحديدية والسمنت الليفي. استعمال الهياكل الحديدية المقيسة في الإنشاء .	المستوى الذهبي (LEED) اختير كفضل عشرة مشاريع خضراء لعام 2011 من قبل AIA



## Effect of Transverse Base Width Restraint on the Cracking Behavior of Massive Concrete

**Dr. Adnan Falih. Ali**  
Professor  
Baghdad University  
Email: adnan.f@yahoo.com

**Dr. Omar Al-Farouq Al-Damluji**  
Professor  
Baghdad University  
Email: omaraldamluji@gmail.com

**Dr. Ala'a Hussein. A. Al-Zuhairi**  
Lecturer  
Baghdad University  
Email: alaawn@yahoo.com

### Abstract

The effect of considering the third dimension in mass concrete members on its cracking behavior is investigated in this study. The investigation includes thermal and structural analyses of mass concrete structures. From thermal analysis, the actual temperature distribution throughout the mass concrete body was obtained due to the generation of heat as a result of cement hydration in addition to the ambient circumstances. This was performed via solving the differential equations of heat conduction and convection using the finite element method.

The finite element method was also implemented in the structural analysis adopting the concept of initial strain problem. Drying shrinkage volume changes were calculated using the procedure suggested by ACI Committee 209 and inverted to equivalent temperature differences to be added algebraically to the temperature differences obtained from thermal analysis.

Willam-Warnke model with five strength parameters is used in modeling of concrete material in which cracking and crushing behavior of concrete can be included. The ANSYS program was employed in a modified manner to perform the above analyses.

A thick concrete slab of 1.5m in thickness and 10m in length was analyzed for different widths 2, 4, 8, and 10m to produce different aspect ratios (B/L) of 0.2, 0.4, 0.8, and 1.0 respectively. The results of the analyses show an increase in cracking tendency of mass concrete member as the aspect ratio of the same member is increased due to the effect of transverse base restraint. Accordingly, such effect cannot be ignored in the analysis of base restrained mass concrete structures subjected to temperature and drying shrinkage volume changes.

**Keywords:** Mass concrete, temperature difference, drying volume change, base restraint, concrete cracking.

د. علاء حسين علوان الزهيري  
مدرس

د. عمر الفاروق الدملوجي  
استاذ

د. عدنان فالح علي  
استاذ

## ANSYS

10 8 4 2

10

1.5

1.0 0.8 0.4 0.2

/

## Introduction

Mass concrete is an expression usually used for any concrete structure with dimensions large enough to cause structural problems during and after the construction period. These problems are mainly the occurrence of cracking due to temperature variations and shrinkage volume changes. Like any solid material, concrete is affected by increase and decrease of temperature. The effect appears as a thermal strain that occurs within the concrete structure when it is prevented or restricted from motion, i.e., restrained. The second category of volume change is the drying shrinkage, which is related to the drying and shrinking of the cement gel.

ACI 207 Committee (ACI Committee 1995) suggested the following equations to be

Used to calculate the degree of restraint for rigid continuous base restraint.

$$K_R = \left[ \frac{(L/H - 2)}{(L/H + 1)} \right]^{h/H} \text{ for } L/H \geq 2.5 \quad (1)$$

$$K_R = \left[ \frac{(L/H - 1)}{(L/H + 10)} \right]^{h/H} \text{ for } L/H < 2.5$$

Where

$K_R$  = degree of restraint

$L/H$  = length to height ratio, and

$h$  = the height at which the degree of restraint is calculated.

As can be noticed, ACI 207 Committee neglects the effect of the restraint in the transverse direction and hence, eq. (1) can be applied to the concrete walls only. Therefore, it is the objective of the present study to investigate the effect of transverse base restraint, i.e., effects of 3<sup>rd</sup> dimension on the behavior of massive concrete and therefore cracking tendency and cracking prevention in such structures.

$c_p$  = specific heat, and

$\rho$  = density.

On the other hand, heat may transfer by convection according to the following Newton formula (Holman, 1981):

$$q = \int_A h_{cv} (T - T_\infty) dA \quad (3)$$

## Thermal Analysis

Based on Fourier's Law for heat transfer, the heat conduction equation can be expressed as follows (Holman, 1981):

$$k_x \frac{\partial^2 T}{\partial x^2} + k_y \frac{\partial^2 T}{\partial y^2} + k_z \frac{\partial^2 T}{\partial z^2} + \bar{q} = \rho c_p \frac{\partial T}{\partial t} \quad (2)$$

where,

$k_x$ ,  $k_y$  and  $k_z$  = heat conductivity of the material in  $x$ ,  $y$  and  $z$ -direction respectively,

$T$  = the difference between absolute and reference temperatures,

$\bar{q}$  = heat generation per unit volume,

where,

$h_{cv}$  = convection heat transfer coefficient (film coefficient).

$T_\infty$  = bulk fluid temperature.

$T$  = temperature.

Both of the above equations may be discretized using Rayleigh-Ritz variation process to derive an expression employing the finite difference method to overcome the time-rate nature of the problem, that is,

$$[K_e^*]\{\Delta\delta(t)\} = \{F^*\} \quad (4)$$

where,

$$[K_e^*] = [K_e] + \frac{[C]}{\Delta t}$$

$$\{F^*\} = \{\Delta F(t)\} + \frac{[C]}{\Delta t}\{\Delta\delta(t-\Delta t)\}$$

Eq. (4) is used in the finite element method to predict the temperature distribution within the mass concrete body invoking the described initial and boundary temperatures as follows:

1. Initial temperature = concrete placement temperature = 20°C.
2. Bulk ambient temperature  $T_\infty$  which is specified for Baghdad climate according to Kammouna, 2001, from:

$$T_\infty = 29.815 - 15.291 \cos(0.893t) \quad (5)$$

Where, t is time in days.

### Shrinkage Strain Calculation

Following the procedure recommended by (ACI Committee 209, 1992) and taking the ambient circumstances and concrete mixing and placing conditions, the drying shrinkage strains may be calculated as a function of time after curing period for concrete which is assumed to be seven days.

Quoting the concept of evaporable moisture content that was adopted by Carlson, 1937, the distribution of drying shrinkage strains may be assessed within the body of mass concrete member. Table (1) shows such distribution in which the values of drying shrinkage strains seem very low. Such observation may be related to the non-convenience of eq. (6) that was suggested by ACI 209 Committee (ACI Committee, 1992) and used to estimate shrinkage strain-time relation.

$$(\epsilon_{sh})_t = \frac{t}{35+t} (\epsilon_{sh})_u \quad (6)$$

where,

$(\epsilon_{sh})_t$  = shrinkage strain at any time t (in days), and

$(\epsilon_{sh})_u$  = ultimate shrinkage strain =  $780 \times 10^{-6}$ .

As can be seen from eq. (6) 50% only of the ultimate shrinkage strain occurs at 35 days after curing. However, one can conclude from the trend of the drying shrinkage strains as they are decreased with the increase in the width of the slab as the major cause of cracking in large mass concrete members is the temperature variation rather than shrinkage volume changes.

### Adopted Constitutive Relationship For Concrete

The concrete was modeled using Willam and Wranke model (Willam and Wranke, 1974) which predicts failure of brittle materials in which the cracking and crushing modes should be accounted for. The criterion for failure of concrete due to a multiaxial stress state can be expressed in the form:

$$\frac{F}{f'_c} - S \geq 0 \quad (7)$$

where,

F = a function of the principal stress state  $(\sigma_{xp}, \sigma_{yp}, \sigma_{zp})$ ,

S = failure surface expressed in terms of principal stresses and five input strength parameters as follows:

$f'_t$  = ultimate uniaxial tensile strength in MPa

$f'_c$  = ultimate uniaxial compressive crushing strength in MPa,

$f'_{cb}$  = ultimate biaxial compressive strength in MPa,

$\sigma_h$  = ambient hydrostatic stress state in MPa,

$f_1$  = ambient hydrostatic stress state of biaxial superimposed on hydrostatic stress state in MPa, and

$f_2$  = ambient hydrostatic stress state of uniaxial superimposed on hydrostatic stress state in MPa.

For simplicity, Willam and Warnke, 1974, suggested the following equations to calculate three of strength parameters in terms of  $f'_c$  in case of  $|\sigma_h| \leq \sqrt{3}f'_c$ . Thus, the failure surface S can be specified with a minimum two constants,  $f'_t$  and  $f'_c$ .

$$\begin{aligned} f_{cb} &= 1.2 f'_c \\ f_1 &= 1.45 f'_c \\ f_2 &= 1.725 f'_c \end{aligned} \quad (8)$$

functions were specified to describe the function F and the failure surface S. The failure surface S can be seen in Fig. (1).

Failure of concrete is categorized into four domains. In each domain, independent

### Compression-Compression-Compression Domain( $0 \leq \sigma_1 \leq \sigma_2 \leq \sigma_3$ )

In this case, F takes the form:

$$F = F_1 = \frac{1}{\sqrt{15}} \left[ (\sigma_1 - \sigma_2)^2 + (\sigma_2 - \sigma_3)^2 + (\sigma_3 - \sigma_1)^2 \right]^{\frac{1}{2}} \quad (9)$$

and the failure surface S is defined as:

$$S = S_1 = \frac{2r_2(r_2^2 - r_1^2) \cos \eta + r_2(2r_1 - r_2) \left[ 4(r_2^2 - r_1^2) \cos^2 \eta + 5r_1^2 - 4r_1 r_2 \right]^{\frac{1}{2}}}{4(r_2^2 - r_1^2) \cos^2 \eta + (r_2 - 2r_1)^2} \quad (10)$$

where,

$$\cos \eta = \frac{2\sigma_1 - \sigma_2 - \sigma_3}{\sqrt{2} \left[ (\sigma_1 - \sigma_2)^2 + (\sigma_2 - \sigma_3)^2 + (\sigma_3 - \sigma_1)^2 \right]^{\frac{1}{2}}}$$

in which  $\eta$  = angle of similarity, and

$$r_1 = a_0 + a_1 \xi + a_2 \xi^2$$

$$r_2 = b_0 + b_1 \xi + b_2 \xi^2$$

$$\xi = \frac{\sigma_h}{f'_c}$$

The undetermined coefficients  $a_0, a_1, a_2, b_0, b_1,$  and  $b_2$  are discussed below.

When  $\eta = 0^\circ$ ,  $S_1$  in eq. (10) is equal to  $r_1$  while if  $\eta = 60^\circ$ ,  $S_1$  is equal to  $r_2$ . Therefore, the function  $r_1$  represents the failure surface of all stress states with  $\eta = 0^\circ$ .

The function  $r_1$  is determined by adjusting  $a_0, a_1,$  and  $a_2$  such that  $f'_t, f'_{cb}$  and  $f_1$  all lie on the failure surface. Mathematically:

$$\left\{ \begin{aligned} \frac{F_1}{f'_c} (\sigma_1 = f'_t, \sigma_2 = \sigma_3 = 0) \\ \frac{F_1}{f'_c} (\sigma_1 = 0, \sigma_2 = \sigma_3 = -f_{cb}) \\ \frac{F_1}{f'_c} (\sigma_1 = -\sigma_h^a, \sigma_2 = \sigma_3 = -\sigma_h^a - f_1) \end{aligned} \right\} = \begin{bmatrix} 1 & \xi_t & \xi_t^2 \\ 1 & \xi_{cb} & \xi_{cb}^2 \\ 1 & \xi_1 & \xi_1^2 \end{bmatrix} \begin{Bmatrix} a_0 \\ a_1 \\ a_2 \end{Bmatrix} \quad (11)$$

In which:

$$\xi_t = \frac{f'_t}{3f'_c}, \quad \xi_{cb} = \frac{f_{cb}}{3f'_c}, \quad \text{and} \quad \xi_1 = -\frac{\sigma_h^a}{f'_c} - \frac{2f_1}{3f'_c}.$$

The proper values for the coefficient  $a_0, a_1,$  and  $a_2$  can be determined through the solution of the simultaneous equations given in eq. (11).

The function  $r_2$  is calculated by adjusting  $b_0, b_1,$  and  $b_2$  to satisfy the conditions:

$$\begin{pmatrix} \frac{F_1}{f'_c}(\sigma_1 = \sigma_2 = 0, \sigma_3 = -f'_c) \\ \frac{F_1}{f'_c}(\sigma_1 = \sigma_2 = -\sigma_h^a, \sigma_3 = -\sigma_h^a - f_2) \\ 0 \end{pmatrix} = \begin{bmatrix} 1 & -\frac{1}{3} & \frac{1}{9} \\ 1 & \xi_2 & \xi_2^2 \\ 1 & \xi_0 & \xi_0^2 \end{bmatrix} \begin{Bmatrix} b_0 \\ b_1 \\ b_2 \end{Bmatrix} \quad (12)$$

Where,

$$\xi_2 \text{ is defined by: } \xi_2 = -\frac{\sigma_h^a}{f'_c} - \frac{f_2}{3f'_c}.$$

and  $\xi_0$  is the positive root of the equation:

$$r_2(\xi_0) = a_0 + a_1\xi_0 + a_2\xi_0^2 \quad (13)$$

in which  $a_0$ ,  $a_1$ , and  $a_2$  are evaluated by eq. (11).

Since the failure surface must remain convex, the ratio  $r_1/r_2$  is restricted to the range ( $0.5 < r_1/r_2 < 1.25$ ), although the upper bound is not considered to restriction since ( $r_1/r_2 < 1.0$ ) for most materials. Also, the coefficients  $a_0$ ,  $a_1$ ,  $a_2$ ,  $b_0$ ,  $b_1$ , and  $b_2$  must satisfy the conditions:

$$a_0 > 0, a_1 \leq 0, a_2 \leq 0$$

$$b_0 > 0, b_1 \leq 0, b_2 \leq 0$$

Therefore, the failure surface is closed and predicts failure under high hydrostatic pressure ( $\xi < \xi_2$ ). This closure of the failure surface has not been verified experimentally and it has been suggested that Von Mises type cylinder is a more valid failure surface for large compressive  $\sigma_h$ -

values. Consequently, it is recommended that values of  $f_1$  and  $f_2$  are selected at a hydrostatic stress level in the vicinity of or above the expected maximum hydrostatic stress encountered in the structure.

Eq. (9) describes the condition that the failure surface has an apex at  $\xi = \xi_0$ . A profile of  $r_1$  and  $r_2$  as a function of  $\xi$  is shown in Fig. (2). The lower curve represents all stress state such that  $\eta = 0^\circ$  while the upper curve represents stress state such that  $\eta = 60^\circ$ . If the failure criterion is satisfied, the material is assumed to crush.

### Tension-Compression-Compression

#### Domain ( $\sigma_1 \geq 0 \geq \sigma_2 \geq \sigma_3$ )

In this regime, F takes the form:

$$F = F_2 = \frac{1}{\sqrt{15}} \left[ (\sigma_2 - \sigma_3)^2 + \sigma_2^2 + \sigma_3^2 \right]^{\frac{1}{2}} \quad (14)$$

and S is defined as:

$$S = S_2 = \left( 1 - \frac{\sigma_1}{f'_t} \right) \frac{2p_2(p_2^2 - p_1^2) \cos \eta + p_2(2p_1 - p_2) \left[ 4(p_2^2 - p_1^2) \cos^2 \eta + 5p_1^2 - 4p_1p_2 \right]^{\frac{1}{2}}}{4(p_2^2 - p_1^2) \cos^2 \eta + (p_2 - 2p_1)^2} \quad (15)$$

where  $\cos \eta$  is already defined above, and

$$p_1 = a_0 + a_1\chi + a_2\chi^2$$

$$p_2 = b_0 + b_1\chi + b_2\chi^2$$

$$\chi = \frac{1}{3}(\sigma_2 + \sigma_3)$$

The coefficients  $a_0$ ,  $a_1$ ,  $a_2$ ,  $b_0$ ,  $b_1$ , and  $b_2$  are defined by eq. (11) and eq. (12).

If the failure criterion is satisfied, cracking occurs in the plane perpendicular to the principal stress  $\sigma_1$ .

### Tension- Tension -Compression Domain ( $\sigma_1 \geq \sigma_2 \geq 0 \geq \sigma_3$ )

Here the function F takes the form:

$$F = F_3 = \sigma_i ; i = 1, 2 \quad (16)$$

and the failure surface S is defined as:

$$S = S_3 = \frac{f'_t}{f'_c} \left( 1 + \frac{\sigma_3}{S_2(\sigma_i, 0, \sigma_3)} \right); i = 1, 2 \quad (17)$$

If the failure criterion for both  $i = 1, 2$  is satisfied, cracking occur in the planes perpendicular to principal stresses  $\sigma_1$ ,  $\sigma_2$ . If the failure criterion is satisfied only for  $i = 1$ , cracking occurs only in the plane perpendicular to principal stress  $\sigma_1$ .

**Tension- Tension - Tension Domain ( $\sigma_1 \geq \sigma_2 \geq 0 \geq \sigma_3$ )**

In this regime, F takes the form:

$$F = F_4 = \sigma_i ; i = 1, 2, 3 \quad (18)$$

and S is defined as:

$$S = S_4 = \frac{f'_t}{f'_c} \quad (19)$$

If the failure criterion is satisfied in directions 1, 2, and 3, cracking occurs in the planes perpendicular to principal stresses  $\sigma_1$ ,  $\sigma_2$ , and  $\sigma_3$ , otherwise, cracking occurs in plane or plane

Perpendicular to the directions of principal stresses where the failure criterion is satisfied.

**Implementation of the Finite Element Method**

According to Fung, 1965, the effect of temperature changes on an elastic body subjected to external forces may be determined using one of the followings:

1. Solution of the discretized form of the coupled thermo-elastic equation in which the effect of both temperature and displacement on each other may be determined, i.e. the displacement due to unit temperature change and vice versa. However, this procedure is not usually used especially in problems where the temperature changes are not high enough like in mass concrete problem.
2. When the simplifying assumptions mentioned in (1) above are introduced, the theory is referred to as an uncoupled, quasi-static theory; it degenerates into heat conduction and thermoelasticity as two separate problems. Experience shows that the change of temperature of an elastic body due to adiabatic straining is, in general, very small. If this interaction between strain and temperature is ignored, then the only effects of elasticity on the temperature distribution are effects of change in dimensions of the body under investigation. The change in dimension of a body is of the order of product of the linear dimension of the body L, the temperature rise  $\Delta T$ , and the coefficient of thermal expansion  $\alpha$ . If L = 1m and  $\Delta T = 100^\circ\text{C}$ ,  $\alpha = 10 \times 10^{-6}$  per  $^\circ\text{C}$ , the

change in dimension is  $10^{-3}\text{m}$ , which is negligible in problems of heat conduction.

The equivalent temperature changes to the estimated drying shrinkage strains may be calculated using the following simple relation:

$$\Delta T_{DS} = \frac{\varepsilon_{sh}}{\alpha_c} \quad (20)$$

where,

$\Delta T_{DS}$  = drying shrinkage equivalent temperature change,

$\varepsilon_{sh}$  = shrinkage strain, and

$\alpha_c$  = coefficient of thermal expansion of concrete.

Then the equivalent temperature changes to drying shrinkage may be added algebraically to the temperature changes resulting from thermal analysis. The effect of this sum of temperatures, which appears as thermal stress and strain, may be

Detected using the second method described in (2) above. This means that the problem is treated as "an initial stress or strain" problem. The term "initial stress" signifies a stress present before deformations are allowed. Effectively, it is a residual stress to be superposed on stress caused by deformation. The effect of temperature changes can be placed as initial strain  $\varepsilon_o$ , or initial stress and strain  $\sigma_o$  and  $\varepsilon_o$ . Both are viewed as alternative ways to express the same thing (Cook, 1989).

In a linear elastic material, the stress-strain relation is (Cook, 1989):

$$\varepsilon = \frac{\sigma}{E} + \varepsilon_o \quad (21)$$

where,

$$\varepsilon_o = \text{initial strain} = \alpha_c \Delta T$$

or,

$$\sigma = E(\varepsilon - \varepsilon_o) \quad (22)$$

The strain energy  $U_o$  is defined as (Cook, 1989):

$$U_o = \int_v \frac{\sigma \varepsilon}{2} dv \quad (23)$$

Substituting eq. (22) into eq. (23):

$$U_o = \int_v \frac{E}{2} (\varepsilon - \varepsilon_o)^2 dv$$



or,

$$U_o = \int_v \frac{E}{2} (\varepsilon^2 - 2\varepsilon\varepsilon_o + \varepsilon_o^2) dv \quad (24)$$

The third term in the parenthesis in eq. (24) can be omitted since it is independent of nodal displacements. Then its derivative is equal to zero. Thus,

$$U_o = \int_v \frac{E}{2} (\varepsilon^2 - 2\varepsilon\varepsilon_o) dv \quad (25)$$

$$[D] = \frac{E}{(1+\nu)(1-2\nu)} \begin{bmatrix} (1-\nu) & \nu & \nu & 0 & 0 & 0 \\ \nu & (1-\nu) & \nu & 0 & 0 & 0 \\ \nu & \nu & (1-\nu) & 0 & 0 & 0 \\ 0 & 0 & 0 & \frac{1-2\nu}{2} & 0 & 0 \\ 0 & 0 & 0 & 0 & \frac{1-2\nu}{2} & 0 \\ 0 & 0 & 0 & 0 & 0 & \frac{1-2\nu}{2} \end{bmatrix} \quad (27)$$

The potential of external load may be expressed as:

$$\Omega_{ex} = -[u]\{\phi\} \quad (28)$$

where,

$[u]$  = the displacement field vector,

and

$\{\phi\}$  = the load vector.

Furthermore, the potential of body forces is given by:

$$\begin{aligned} \Pi_{p_o} &= U_o + \Omega \\ &= \frac{1}{2} [ \varepsilon ] [D] \{ \varepsilon \} - [ \varepsilon ] [D] \{ \varepsilon_o \} - [u] \{ \phi \} - [u] \{ \bar{F} \} \end{aligned} \quad (30)$$

The total potential within the element is:

$$\Pi_{p_e} = \int_v \Pi_{p_o} dv \quad (31)$$

or,

$$\begin{aligned} \Pi_{p_e} &= \frac{1}{2} \int_v [ \varepsilon ] [D] \{ \varepsilon \} dv - \int_v [ \varepsilon ] [D] \{ \varepsilon_o \} dv \\ &\quad - \int_s [u] \{ \phi \} ds - \int_v [u] \{ \bar{F} \} dv \end{aligned} \quad (32)$$

Writing  $u_o = \frac{E}{2} (\varepsilon^2 - 2\varepsilon\varepsilon_o) dv$  = is the energy per unit volume. Hence, for a state of multiaxial stresses:

$$u_o = \frac{1}{2} [ \varepsilon ] [D] \{ \varepsilon \} - [ \varepsilon ] [D] \{ \varepsilon_o \} \quad (26)$$

where

$[D]$  = the constitutive relations matrix for concrete and is defined for linear-elastic material as follows (Cook, 1989):

$$\Omega_{bf} = [u] \{ \bar{F} \} \quad (29)$$

Where,  $\{ \bar{F} \}$  = the body force vector, which is any force distributed over the entire volume of the body like the self-weight.

The total potential energy per unit volume can be written in the form (Cook, 1989):

Since,

$$\{u\} = [N] \{e\} \quad (33)$$

where,

$[N]$  = shape function matrix, and

$\{e\}$  = nodal displacement vector.

Also,

$$\{ \varepsilon \} = [B] \{e\} \quad (34)$$



where,

[B] = strain-nodal displacement matrix.

$$\Pi_{p_e} = \frac{1}{2} \int_v [e]^T [B]^T [D] \{e\} dv - \int_v [e]^T [B]^T [D] \{\varepsilon_o\} dv - \int_s [e]^T [N]^T \{\phi\} ds - \int_v [e]^T [N]^T \{\bar{F}\} dv \quad (35)$$

which after simplification and introducing effects of externally applied nodal forces becomes:

$$\Pi_{p_e} = \frac{1}{2} [e]^T [K] \{e\} - [e]^T \{R\} - [e]^T \{F\} \quad (36)$$

where, {F} = externally applied nodal forces vector.

Applying the minimization of the total potential yields:

$$\frac{\partial \Pi_p}{\partial \{e\}} = 0$$

or,

$$[K] \{e\} = \{F\} + \{R\} \quad (37)$$

where,

$$\{R\} = \int_v [B]^T [D] \{\varepsilon_o\} dv + \int_v [N]^T \{\bar{F}\} dv + \int_s [N]^T \{\phi\} ds$$

Eq. (37) will be used in the analysis of the mass concrete due to effects of temperature and drying shrinkage volume changes.

## Computer Implementation

Besides the “Graphical User Interface (GUI)” that is commonly used in software packages, ANSYS program proposes a programming language similar to some extent to the conventional FORTRAN language. The proposed language is referred as APDL (ANSYS Parametric Design Language).

A modified ANSYS program is adopted in this study. This consists of a main program and four subprograms. The main program contains the principal steps of analysis and required calls for subprograms. Each of these subprograms is responsible of some limit tasks like:

- Performing the thermal analysis,
- Storing temperature values in a pre-dimensioned array,

Hence,

- Calculating drying shrinkage strains throughout the concrete body, and

- Conducting the nonlinear structural analysis by considering the effect of concrete aging via updating concrete strength parameters ( $f_t'$ ,  $f_c'$ ,  $E_c$ ) after deleting the thermal finite element mesh and constructing a new structural one.

Two Types of elements are used in this program:

1. Thermal Solid 70: This element is an eight-noded brick element with one degree of freedom, temperature, at each node. The element is applicable to a three-dimensional, steady state or transient thermal analysis.

2. Structural Solid 65: This element is used for the three-dimensional modeling of the concrete with or without reinforcing bars. The element is defined by eight nodes having three degrees of freedom at each node: translations in the global x, y, and z directions. It is capable of considering cracking in tension and crushing in compression.

## Problem Description and Results

To investigate the effect of the transverse base restraint on the cracking behavior of mass concrete member having the dimensions shown in Fi.(3) due to temperature variation and drying shrinkage volume changes, a nonlinear finite element analysis was applied to base restrained thick plain concrete slab resting on the soil. Four different aspect ratios (width/length) were considered for the case of a slab with fixed bottom cast at the first of January (winter concrete placement) in Baghdad. The aspect ratios were 0.2, 0.4, 0.8, and 1.0 and obtained by fixing the length of the slab to 10 meters and varying the width as 2, 4, 8, and 10 meters. In all these cases, the thickness of the slab was taken as 1.5 m. The properties of the concrete tht adopted during analysis were listed in Table(2).

Thermal and structural analyses were conducted on the slab including all the surrounding circumstances and boundaries utilizing the finite element mesh shown in Fig. (3).



The temperature distribution in the central sections along the length and width directions at some times after concrete placement are shown in Figs. (4) to (15). The assessed final cracking pattern of the concrete slabs with different aspect ratios can be seen in Figs. (16) to (19).

## Conclusions

The following conclusions can be drawn from the results of analysis:

1. Value of peak temperature increases with increasing aspect ratio (B/L) of the slab especially at age of 3 days after concrete placement as shown in Figs. (4), (7), (10) and (13). This may be related to the increase in the magnitude of heat generated upon concrete placement due to volume increase.
2. A small temperature drop at the 28<sup>th</sup> day of concrete age is noticed as the ratio B/L is increased (see Figs. (5), (8), (11) and (14). This is attributed by the effect of the volume to surface ratio (V/S), since the temperature increases with increasing the aspect ratio (B/L).
3. The number of primary cracks (cracks that extend over the entire thickness) increase with increasing the width of slab, i.e., the aspect ratio as shown in Figs. (16), (17) and (18). This can be interpreted as a result of the considerable increase in restraint provided by the slab base and the increase in the maximum temperature due to the hydration process after concrete placement.
4. The full-depth cracks are concentrated at the central portion of the slab where the maximum drop in temperature occurs (Figs. (16) to (19)).

From the above and since it was concluded previously that the major cause of cracking in the thick slabs is temperature drop, the effect of the third dimension (width) cannot be ignored when the response (stresses and cracking) of this type of structures is required. Unfortunately, most of the standards like ACI-Committee neglect the effect of the third dimension and assume a uniform temperature distribution.

## REFERENCES

ACI Committee 207, "Effect of Restraint, Volume Change, and Reinforcement on Cracking in Massive Concrete", (ACI 207.2R-95). American Concrete Institute, Detroit, 1999, 26 pp

ACI Committee 209, "Prediction of Creep, Shrinkage, and Temperature Effects in Concrete Structures", (ACI 209R-92),

(Reapproved 1997). American Concrete Institute, Detroit, 1999, 47 pp.

ANSYS 5.4 Inc., "ANSYS Theory Reference", Eighth Edition, SAS IP, Inc. 1997, Chapter 4 pp. 48-56.

Carlson, R. W., "Drying Shrinkage of Large Concrete Members" ACI Journal, Proceedings, Vol. 33, January-February 1937, pp.327-336.

Cook, R. D., Malkas, D. S., and Plesha, M. E., "Concepts and Applications of Finite Element Analysis", John Wiley and Sons Inc., Third edition, 1989, 630 pp.

Fung, Y. C., "Foundations of Solid Mechanics", Prentice-Hall Inc., Englewood Cliffs, New Jersey, 1965, 525 pp.

Holman, J. P., "Heat Transfer", Fourth Edition, 1976, McGraw-Hill.

Kammouna, Z. M., "Development of A Mathematical Model for Creep of Concrete with Reference to Baghdad Climate", M.Sc. Thesis, Baghdad University, College of Engineering, 2001, 90 pp.

Willam, K. J., and Warnke, E. D., "Constitutive Model for the Triaxial Behavior of Concrete", Proceedings, International Association for Bridge and Structural Engineering, Vol. 19, ISMES, Bergamo, Italy, p. 174 (1975).

**Table (1) Drying shrinkage strains**

d/H (*)	Drying shrinkage strain ( $10^{-6}$ )																			
	Slab width = 2.0m					Slab width = 4.0m					Slab width = 8.0m					Slab width = 10.0m				
	After ... days					After ... days					After ... days					After ... days				
	8	14	28	90	180	8	14	28	90	180	8	14	28	90	180	8	14	28	90	180
0	0.5	3.2	7.5	18.0	24.3	0.2	1.3	3.0	7.1	9.6	0.1	0.6	1.4	3.3	4.4	0.08	0.48	1.12	2.7	3.6
0.2	0.2	1.3	3.1	7.5	10.3	0.1	0.5	1.2	3.0	4.1	0.04	0.25	0.57	1.4	1.9	0.03	0.2	0.47	1.13	1.5
0.4	0.07	0.4	1.01	2.4	3.2	0.03	0.17	0.4	0.96	1.3	0.01	0.08	0.19	0.44	0.63	0.01	0.07	0.15	0.36	0.48
0.6	0.02	0.1	0.3	0.8	1.1	0.01	0.05	0.12	0.3	0.45	0	0.02	0.05	0.14	0.21	0	0.02	0.04	0.11	0.17
0.8	0	0	0	0	0	0	0	0	0	0	0	0	0	0	0	0	0	0	0	0
1.0	0	0	0	0	0	0	0	0	0	0	0	0	0	0	0	0	0	0	0	0

(\*) d/H defines the ratio of the depth from top surface / the slab thickness H.

**Table (2) Material Properties**

Property		Unit	Values for	
			Concrete	Soil
Thermal	Conductivity, k	kJ/m.day.°C	240	72
	Specific heat, $c_p$	kJ/kg.°C	1.0	0.92
Physical & Mechanical	Density, $\rho$	Kg/m <sup>3</sup>	2400	1700
	Modulus of elasticity, E	MPa	23168(*)	1000
	Poisson's ratio, $\nu$	-	0.15	0.40
	Compressive strength, $f'_c$	MPa	21(*)	-
	Tensile strength, $f'_t$	MPa	1.55(*)	-
	Coefficient of thermal expansion, $\alpha$	/°C	$12 \times 10^{-6}$	$0.3 \times 10^{-6}$
	Cohesion, c	MPa	4.7(*)	0.1
	Angle of internal friction, $\phi$	degrees	41.7(*)	20

(\*) The values were assumed or calculated at the age of 28days

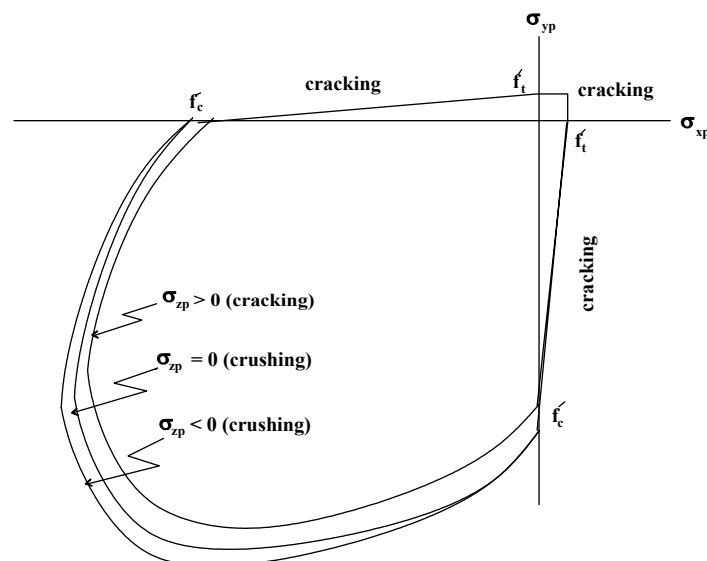


**Fig.(1): Failure surface in principal stress space with nearly biaxial stress state, after ANSYS Inc.**

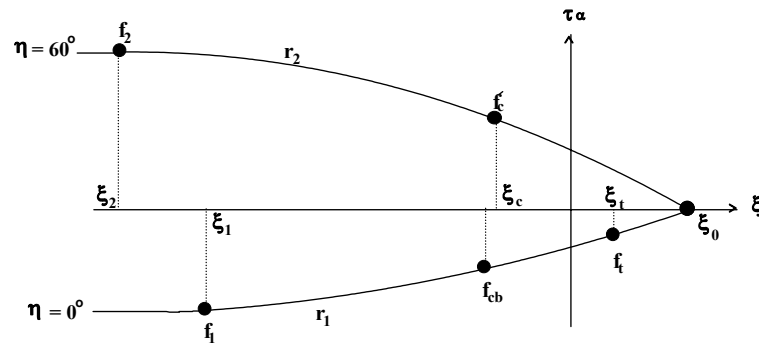


**Fig. (2): A profile of the failure surface, after ANSYS Inc.**

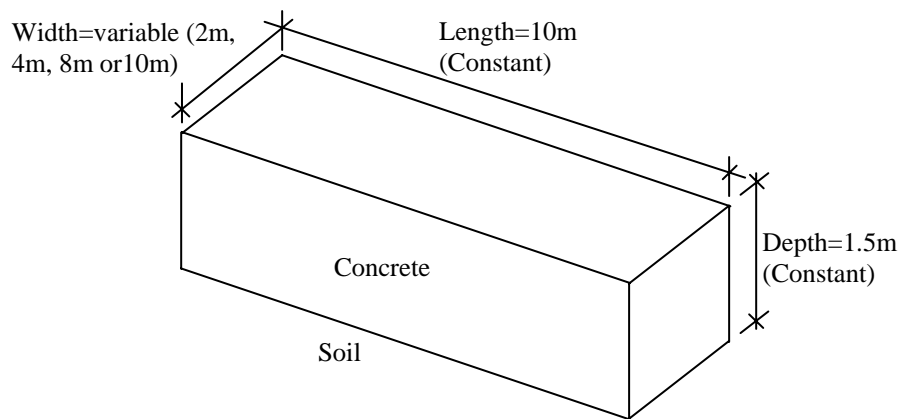
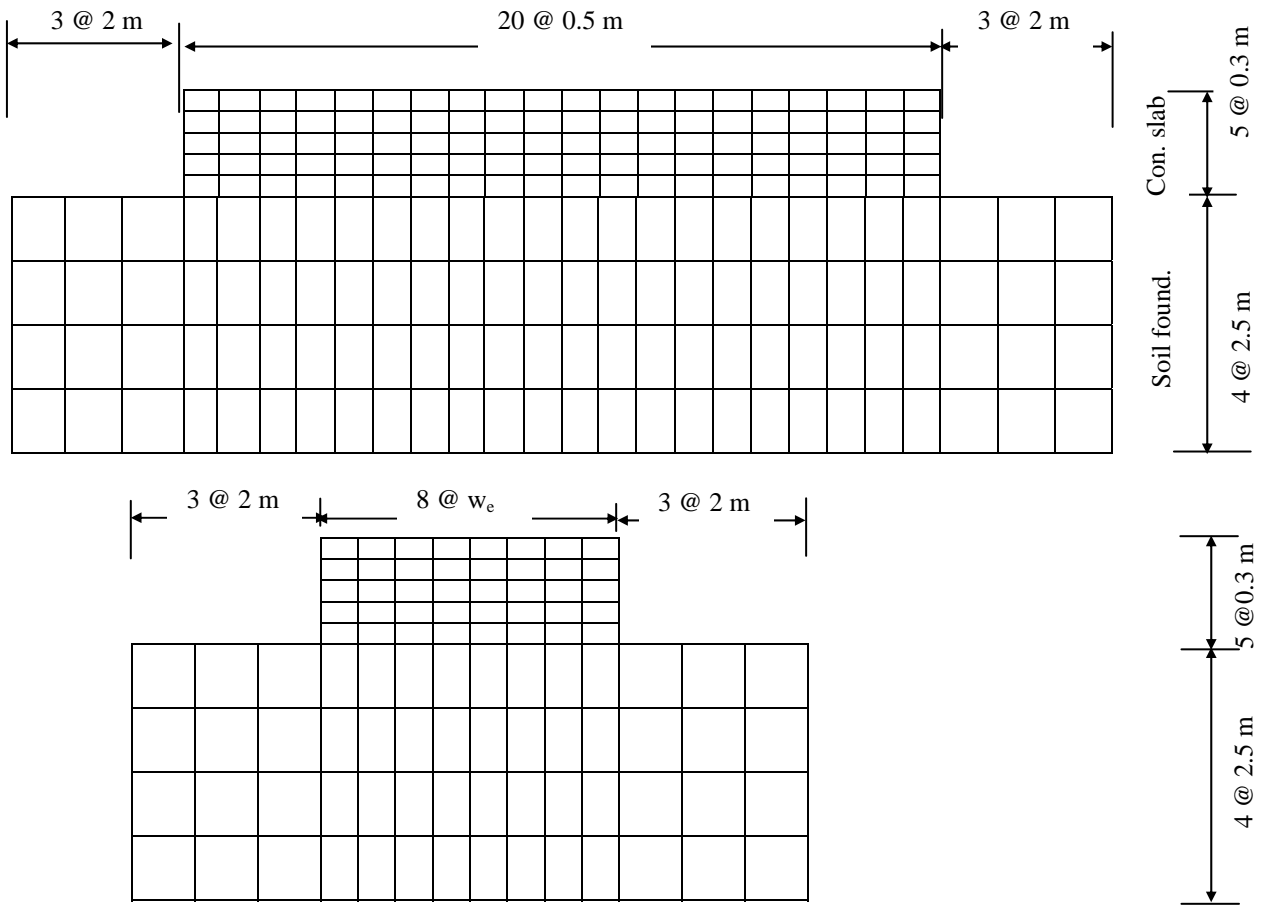


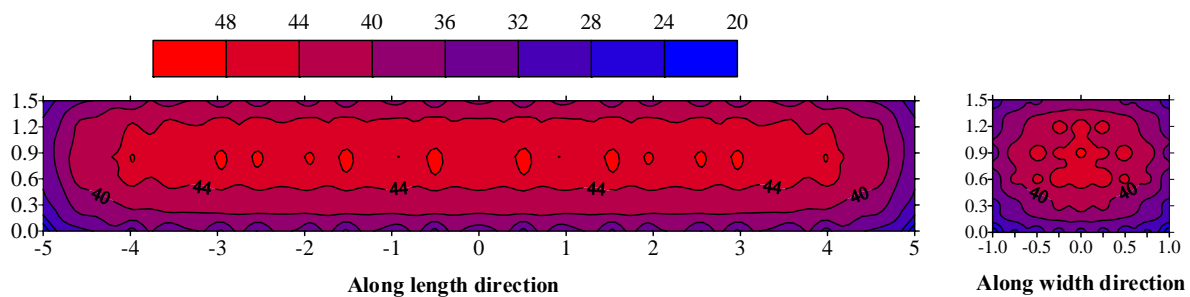
**Fig. (3): Problem Geometry.**



Notes:

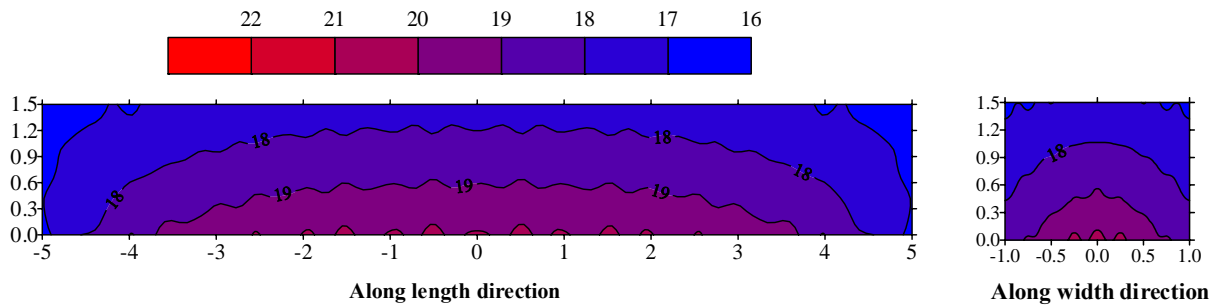
- $w_e$  = concrete element width (variable) = 0.25, 0.5, 1.0, or 1.5 m.
- Dimensions are not to scale.

**Fig. (3): Finite element mesh for a thick concrete slab problem**



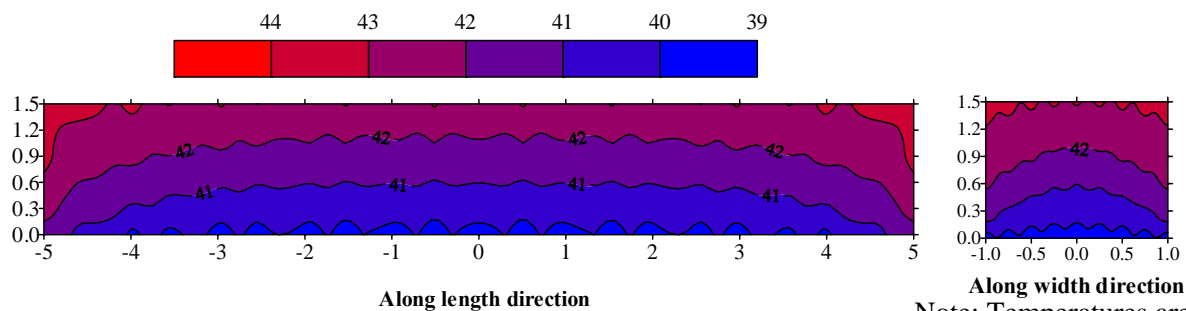
Note: Temperatures are in °C

**Fig. (4): Temperature distribution in a slab with  $B/L=0.2$  (3 days after placement)**



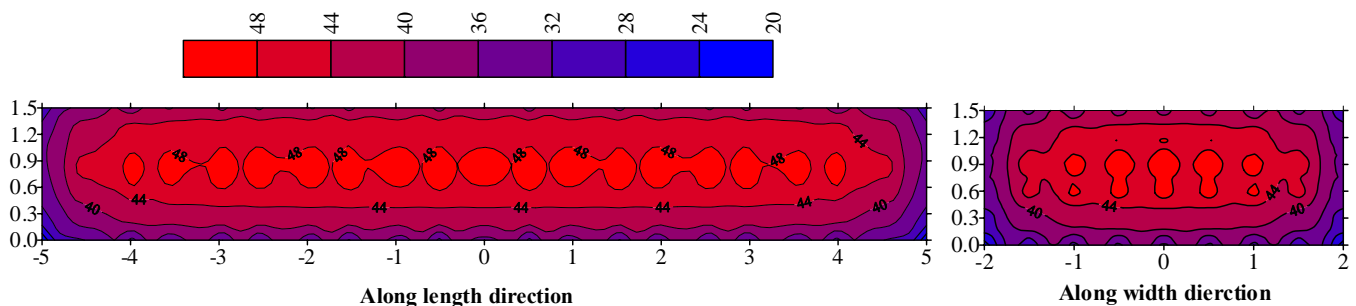
Note: Temperatures are in  $^{\circ}\text{C}$

**Fig. (5): Temperature distribution in a slab with  $B/L=0.2$  (28 days after placement)**



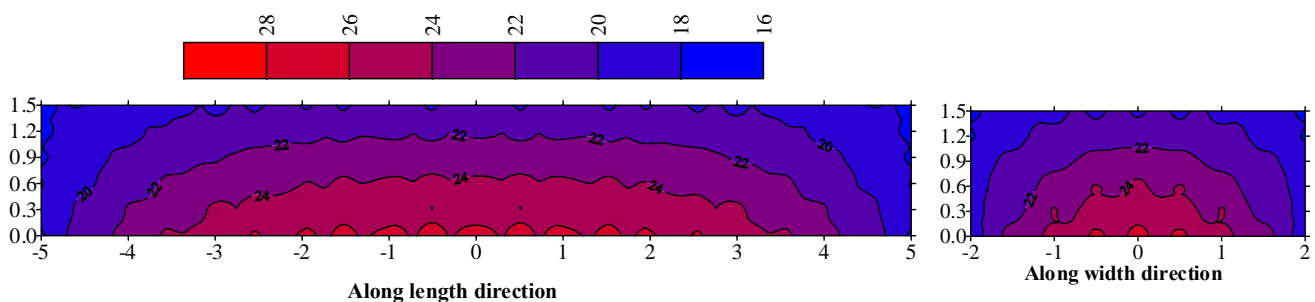
Note: Temperatures are in  $^{\circ}\text{C}$

**Fig. (6): Temperature distribution in a slab with  $B/L=0.2$  (180 days after placement)**



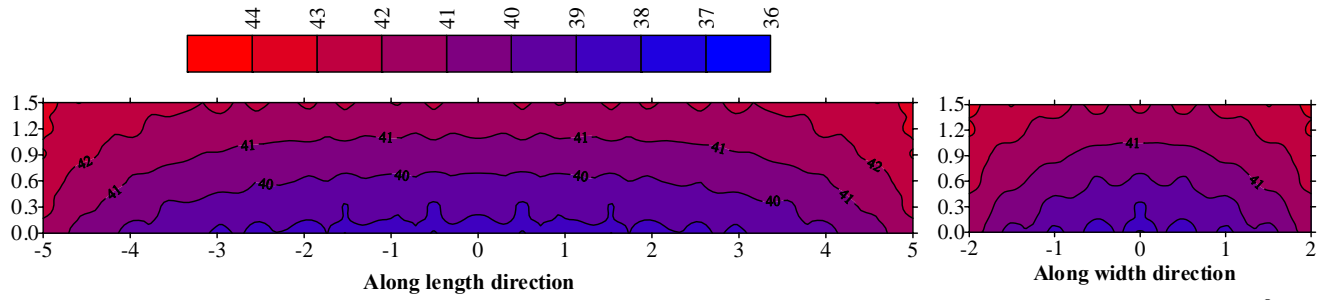
Note: Temperatures are in  $^{\circ}\text{C}$

**Fig. (7): Temperature distribution in a slab with  $B/L=0.4$  (3 days after placement)**



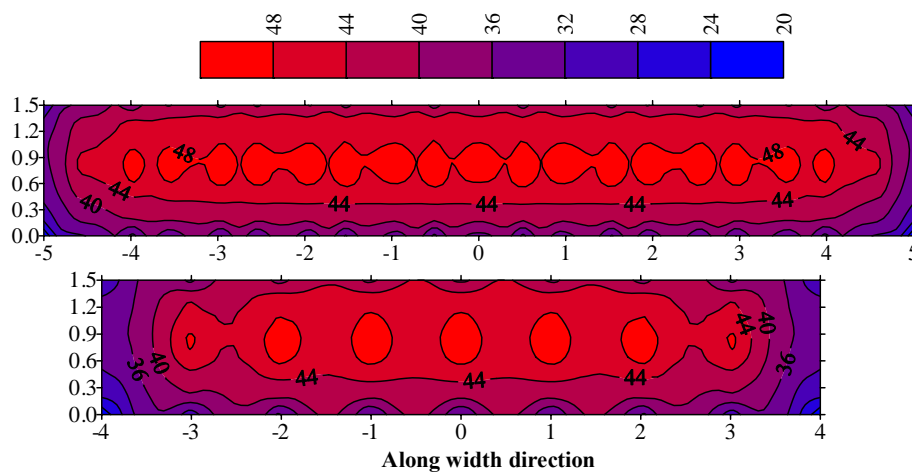
Note: Temperatures are in  $^{\circ}\text{C}$

**Fig. (8): Temperature distribution in a slab with  $B/L=0.4$  (28 days after placement)**



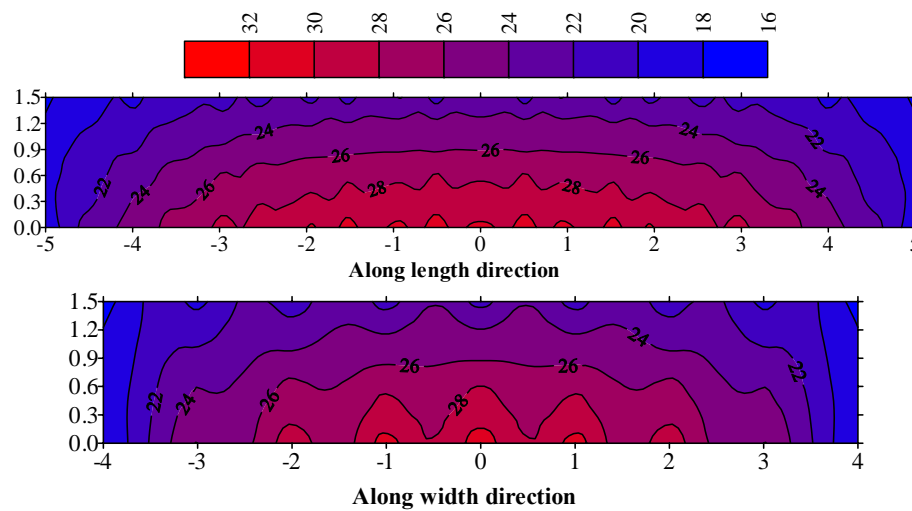
Note: Temperatures are in  $^{\circ}\text{C}$

Fig. (9): Temperature distribution in a slab with  $B/L=0.4$  (180 days after placement)



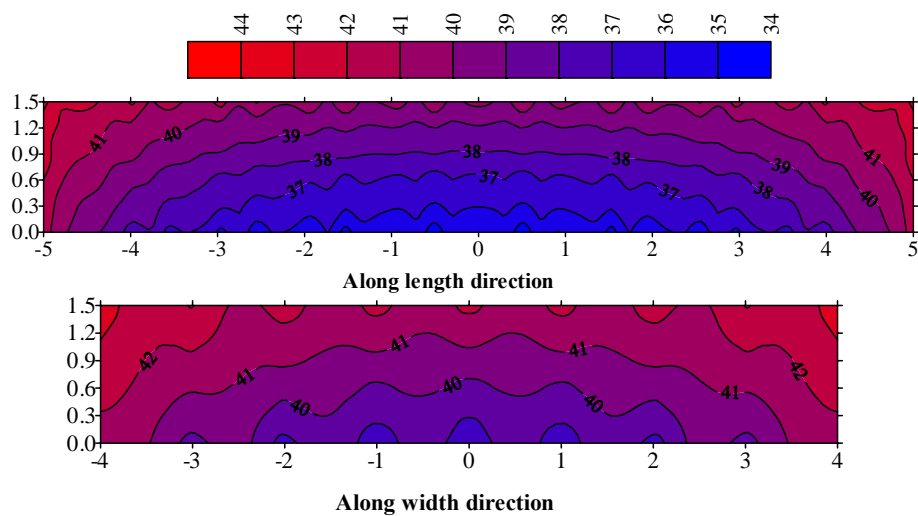
Note: Temperatures are in  $^{\circ}\text{C}$

Fig. (10): Temperature distribution in a slab with  $B/L=0.8$  (3 days after placement)



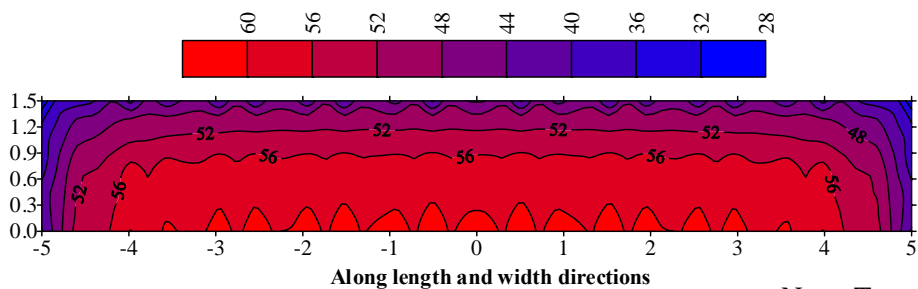
Note: Temperatures are in  $^{\circ}\text{C}$

Fig. (11): Temperature distribution in a slab with  $B/L=0.8$  (28 days after placement)



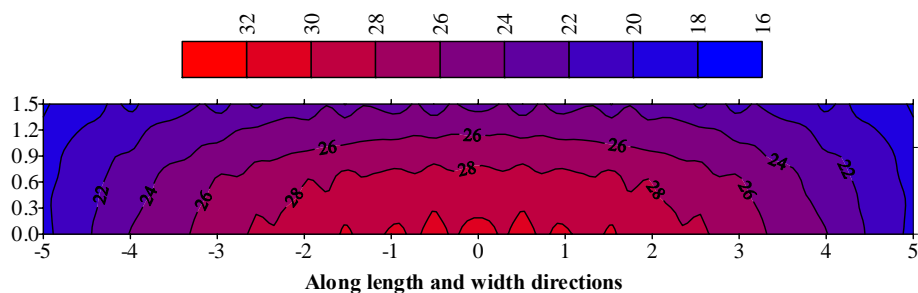
Note: Temperatures are in °C

Fig. (12): Temperature distribution in a slab with  $B/L=0.8$  (180 days after placement)



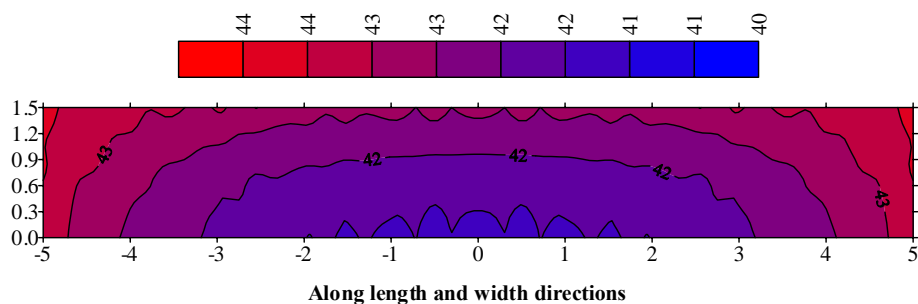
Note: Temperatures are in °C

Fig. (13): Temperature distribution in a slab with  $B/L=1.0$  (3 days after placement)



Note: Temperatures are in °C

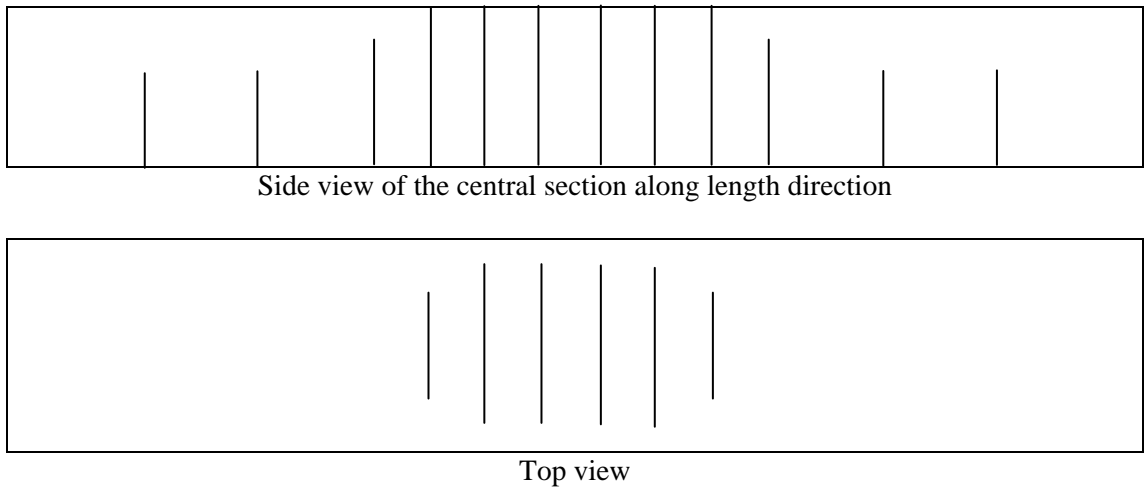
Fig. (14): Temperature distribution in a slab with  $B/L=1.0$  (28 days after placement)



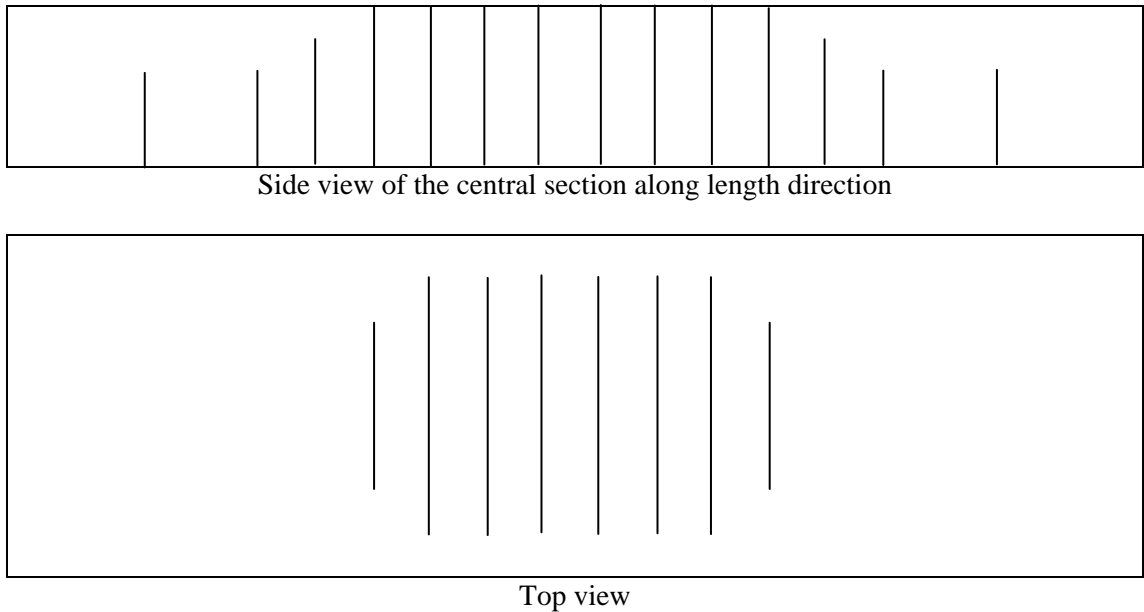
Note: Temperatures are in °C

Fig. (15): Temperature distribution in a slab with  $B/L=1.0$  (180 days after placement)





**Fig. (16): Final cracking pattern for slab cast in winter with B/L=0.2**



**Fig. (17): Final cracking pattern for slab cast in winter with B/L=0.4**

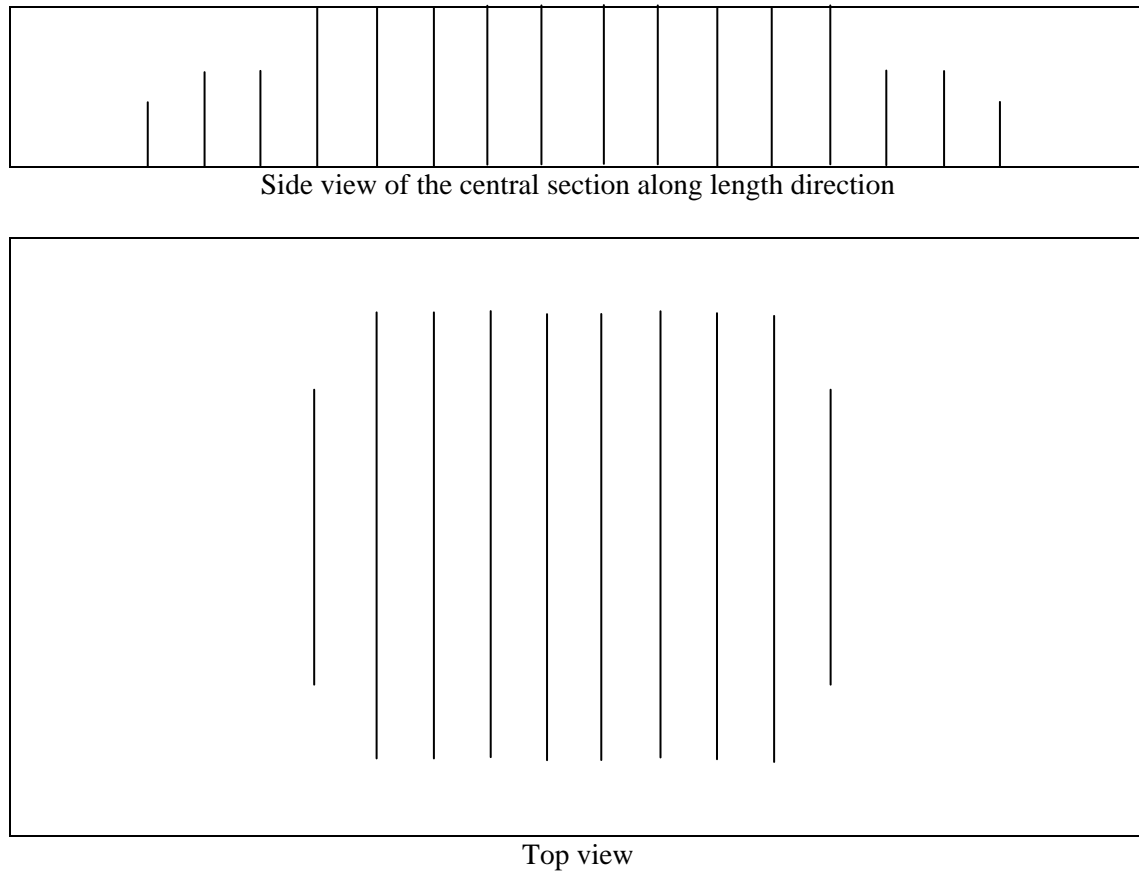


**Fig. (18): Final cracking pattern for slab cast in winter with  $B/L=0.8$**

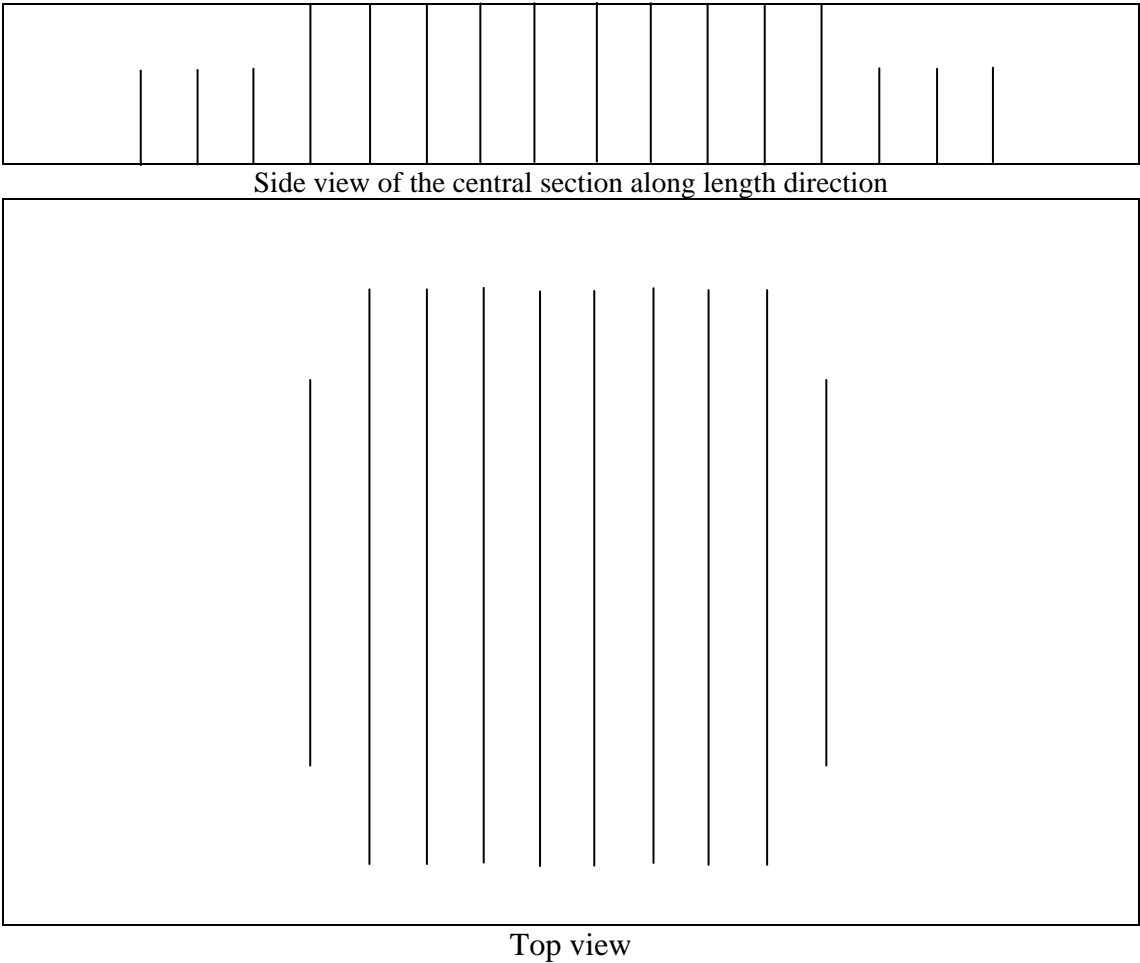


**Fig. (19): Final cracking pattern for slab cast in winter with  $B/L=1.0$**

## Replacement of Line Loads acting on slabs to equivalent uniformly Distributed Loads

Ass.Prof.Dr.AbdulMuttalib

abdmusawi@yahoo.com

Department of Civil Engineering

College of Engineering

University of Baghdad

Dr. Salah Rohaima Obed

Email: salahalzaidee2004@gmail.com

lecturer / Department of Civil Engineering

College of Engineering

University of Baghdad

Salam Mreh Ayez

Email:salamalkhafaji84@yahoo.com

M. Sc. Student

Department of Civil Engineering

College of Engineering

University of Baghdad

### Abstract

This study aims to derive a general relation between line loads that acting on two-way slab system and the equivalent uniformly distributed loads. This relation will be so useful to structural designer that are used to working with a uniformly distributed load and enable them to use the traditional methods for analysis of two-way systems (e.g. Direct Design Method).

Two types of slab systems, Slab System with Beams and Flat Slab Systems, have been considered in this study to include the effect of aspect ratio and type of slab on the proposed relation. Five aspect ratios,  $l_2/l_1$  of 0.5, 0.75, 1.0, 1.5 and 2.0, have been considered for both types of two-way systems.

All necessary finite element analyses have been executed with **SAFE Software**. Data obtained from the F. E. analyses have been used in a statistical analysis using **Statistic Software** to derive the relation based on a Linear Regression Analysis.

**Keywords:** Line Loads, Equivalent Uniformly Distributed Loads, Two-way Slabs, Flat Slabs, SAFE, Finite Element Analysis, Statistical Analysis, Linear Regression Analysis.

### أستبدال الأحمال الخطية المؤثرة على البلاطات الى احمال مكافئة موزعة بانتظام

سلام مريح عايز

طالب ماجستير/مدني

كلية الهندسة/ جامعة بغداد

د. صلاح رحيمه عبيد

مدرس/قسم الهندسة المدنية

كلية الهندسة / جامعة بغداد

### الخلاصة:

تقدم هذه الدراسة بحثاً تحليلياً يخص تحويل الأحمال الخطية المسلطة على السقوف الخرسانية كأحمال الجدران الى أحمال منتشرة وموزعة بانتظام مكافئة للأحمال الأصلية ومؤثرة على كافة مساحة السقف وذلك لتسهيل عملية التصميم لهذه السقوف بطرق التصميم السائدة والمعدة بالاساس للأحمال الموزعة بانتظام كطرق التصميم الموجودة في المدونة الأمريكية (مثل طريقة التصميم المباشر).

تم أخذ نوعين من أكثر أنواع السقوف انتشاراً (السقوف المسندة على أعتاب خرسانية والسقوف المستوية) حيث تم دراسة أهم العوامل المؤثرة على العلاقة بين الحمل الخطي والحمل المنتشر المكافئ له ومن أهمها نسبة طول الفضاء الى طول الفضاء العمودي عليه وكذلك نسبة جساءة العتیب الى جساءة السقف (في النوع الاول فقط) حيث تم أخذ خمسة نسب من نسبة طول الفضاء الى طول الفضاء العمودي عليه (0.5, 0.75, 1.0, 1.5 و 2.0) لكل نوع منهما.

تم تسليط أحمال خطية مرة وموزعة بانتظام مرة أخرى على هذه السقوف وحللت بطريقة العناصر المحددة وبأستخدام برنامج: (SAFE Software V. 12).

ولإيجاد العلاقة بين الحمل الخطي والحمل الموزع بانتظام و المكافئ له تم الاعتماد على طريقة تحليل الانحدار حيث تم ادخال البيانات المستحصلة من تحليل الانظمة أعلاه الى البرنامج الاحصائي: (STATISTIC Software)

**الكلمات الرئيسية:** الأحمال الخطية، الأحمال المكافئة الموزعة بانتظام ، بلاطات ثنائية، بلاطات مستوية، تحليل السقوف بطريقة العناصر المحددة، التحليل بالعناصر المحددة، التحليل الإحصائي، تحليل الارتباط الخطي.

## INTRODUCTION

Line loads, as may be applied by walls, are a special case of loads acting on small areas. It has apparently been customary to take the weight of interior walls into account by adding an addition uniformly distributed loads of  $1.44 \text{ kN/m}^2$  to the dead load of the slab.<sup>(1)</sup>

**Woodring** <sup>(2)</sup> studied the effects of an arbitrary length placed concrete block wall weighing  $4.43 \text{ kN/m}$  ( $304 \text{ lb/ft}$ ) and extending to an arbitrary length. The wall was considered to have zero stiffness and hence to apply a uniform line load to the slab regardless of the slab deflection. Considering a single wall, the  $1.44 \text{ kN/m}^2$  ( $30 \text{ psf}$ ) allowance was more adequate than for any length and placement of the wall as far as the negative moments in beamless slabs were concerned. However, if the wall was placed at midspan and especially if it extends across several panels, the  $1.44 \text{ kN/m}^2$  ( $30 \text{ psf}$ ) allowance was inadequate for positive moments. When the wall extended across the full width of one panel, the required allowance to properly compensate for the effects on midspan moments acting in the direction perpendicular to the wall varied from  $3.2 \text{ kN/m}^2$  when  $l_1 = 6.1\text{m}$  to  $2.1 \text{ kN/m}^2$  when  $l_1 = 9.15\text{m}$ . If the wall extended across more than one panel, the required equivalent loads would be slightly larger. Thus, it may be desirable, if inconvenient; to design the positive-moment sections with one equivalent load and the negative-moment sections for another lower equivalent load. Then the equivalent uniformly distributed load can be computed by using the following equation <sup>(1)</sup>:

$$w^* = \frac{\bar{w}C}{L} \quad (1)$$

Where:

: is the equivalent uniformly distributed load per unit width.

: is the weight of wall per unit length.

: Span of square panel.

C: concentration coefficient, where a positive number indicates moments with the same sign as are caused by distributed loads.

According to Syrian Code<sup>(3)</sup>, the line loads light in weight can be replaced by an equivalent uniformly distributed load when the line loads on slab systems equal to or less than  $1.5 \text{ kN/m}^2$  on the area under wall and as shown in **Fig. 1**.

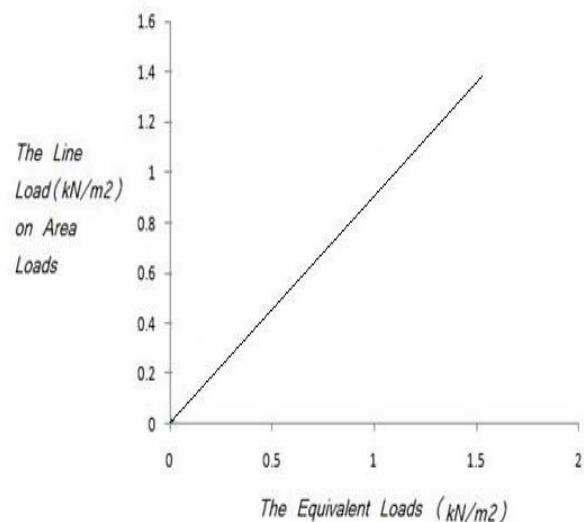


**Fig. 1**  
**Equivalent Uniform Loads to Line Loads <sup>(3)</sup>**

Also when the live load applied on slab systems is greater than a  $6 \text{ kN/m}^2$  the effect of the line loads can be neglected <sup>(3)</sup>.

According to Egyptian Code, when the design live loads is greater than or equal to  $5.0 \text{ kN/m}^2$  and the line loads equal to or less than  $1.0 \text{ kN/m}^2$ , line load effects can be neglected <sup>(4)</sup>.

According to the International Building Code, in the office and other buildings where partition locations are subjected to change, provision for partition weight shall be made, whether or not partitions are shown on the construction documents, unless the specified live load exceeds  $3.83 \text{ kN/m}^2$  (80 psf). Such the partition load shall not be less than a uniformly distributed live load of  $0.96 \text{ kN/m}^2$  (20 psf) (according to **IBC 2003**)<sup>(5)</sup> or  $0.74 \text{ kN/m}^2$  (15 psf) (according to **IBC 2006**)<sup>(6)</sup>.

### EQUIVALENT UNIFORM LOAD:

As discussed in the previous section, most of current methods for estimating the equivalent uniformly distributed load recommend a constant value of the equivalent uniformly distributed load that does not depend neither on the intensity of the original line load nor on system parameters (existence of beams, stiffness of beams, and panel aspect ratio). The main goal of this study is to develop a more rigorous relation that includes these effects into account. This has been started with finite element analyses of the two-way systems under a unit line loads and unit uniformly distributed loads. These finite element results had been used in a linear regression analysis to obtain the required general relation.

### FINITE ELEMENT ANALYSES:

Finite element analyses (executed by **SAFE Software**) for systems with following properties:

1. A Concrete slab of 0.2 m thick.
2. Concrete beams (for slab with beams) with dimensions of 0.4 m by 0.6 m and a relative flexural stiffnesses “ ” greater than two ( $\alpha \frac{I_2}{I_1}$ ).
3. All concrete columns have dimensions of 0.4 m by 0.4 m.

4. A line load of ( 1 ) and uniform distribution load ( $1 \text{ kN/m}^2$ ).
5. A square finite element mesh with dimensions of 20 cm by 20 cm.

Five different aspect ratios have been considered in each case study, namely 0.5, 0.75, 1.0, 1.5, and 2.0. Then the lengths will be  $l_2$  is 4, 3, 5, 6, and 8 and  $l_1$  is 8, 4, 5, 4, and 4.

For each aspect ratio, the system has been subjected to the following two load cases:

First Load Case: This load case intends to simulate the floor systems that subjected to quasi symmetrical line loads. Then in this load case all center lines in the direction under consideration have been subjected to line loads and as shown in **Fig. 2** for slab with beams and in **Fig. 3** for flat slab systems.

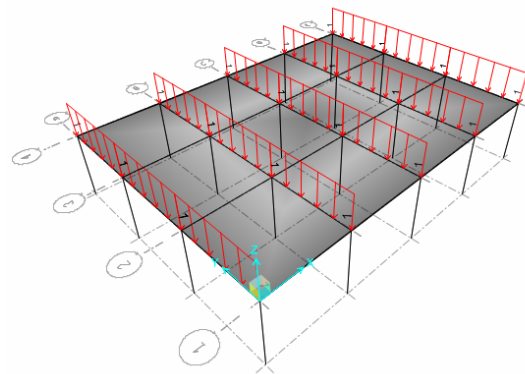


**Fig. 2:**  
Slab with beams subjected to unit line load (kN/m).

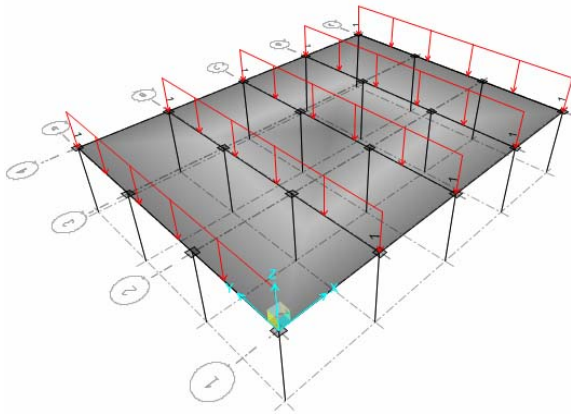


**Fig. 3:**  
Flat slab subjected to unit line load (kN/m).

In the second Load Case the re-analysis of these systems under a uniformly distributed load with unit load value as shown in **Fig. 4** for slab with beams and **Fig. 5** for flat slab systems to obtain the data in **Table 1** for slab with beams and then, to obtain **Table 2** for flat plat slabs.

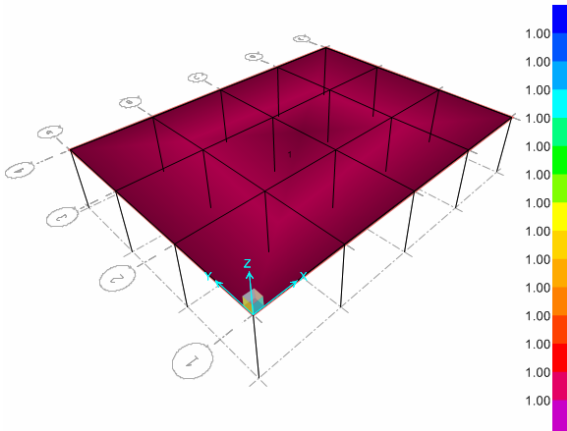


**Fig. 4:**

## Replacement of Line Loads acting on slabs To equivalent uniformly Distributed Loads

Slab with beams subjected to unit uniformly  
Distribution load (kN/m<sup>2</sup>).

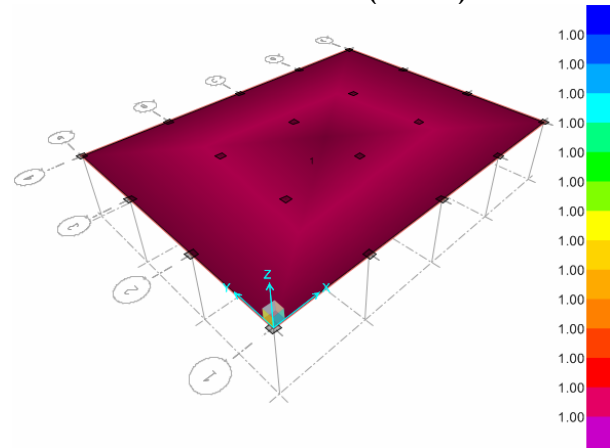


**Fig. 5:**  
Flat slab subjected to unit uniformly  
Distribution load (kN/m<sup>2</sup>).

In these Tables, the ratio  $W_{UDL}/W_{Line}$  Load has been computed as follows:

1. Based on linearity of structure:

$$M_{Due\ to\ Line\ Load} = M_{Unit\ Line\ Load} \times W_{Line}$$

$$M_{Due\ to\ UDL} = M_{Due\ to\ Unit\ UDL} \times W_{UDL}$$

2. Based on definition of the equivalent uniformly distributed load:

$$\therefore M_{Due\ to\ UDL} = M_{Due\ to\ Line\ Load}$$

$$\therefore M_{Unit\ UDL} \times W_{UDL} = M_{Unit\ Line\ Load} \times W_{Line}$$

$$\therefore \frac{W_{UDL}}{W_{Line}} = \frac{M_{Due\ to\ Unit\ Line\ Load}}{M_{Due\ to\ Unit\ UDL}}$$

**Table 1:** Comparison of Moment due to Unit Line Load and Corresponding Unit Uniformly Distributed Load (UDL) for Two-way Slabs with Beams (see Fig. 2 and Fig. 4):

Aspect Ratio	$\alpha$	M <sub>v</sub>	Moments Due to a Unit Line Load ( $kN \times m/m$ )			Moments Due to Unit UDL ( $kN \times m/m$ )			Average  $W_{UDL}/W_{Line}$  = $M_{Line}/M_{UDL}$
			M <sub>beam</sub>	M <sub>cs</sub>	M <sub>ms</sub>	M <sub>beam</sub>	M <sub>cs</sub>	M <sub>ms</sub>	
0.5	4.342	-M <sub>v</sub>	4.24	0.511	0.418	16.19	2.229	2.365	0.248700924
		+M <sub>v</sub>	1.683	0.181	0.159	6.595	0.527	0.905	0.252024418
0.75	5.787	-M <sub>v</sub>	0.877	0.1194	0.0814	2.3515	0.418	0.465	0.333219972
		+M <sub>v</sub>	0.4579	0.0484	0.0345	1.2341	0.0954	0.2793	0.336151169
1.0	3.742	-M <sub>v</sub>	1.451	0.250	0.133	5.676	1.513	1.932	0.201074444
		+M <sub>v</sub>	0.664	0.100	0.043	2.473	0.338	1.108	0.205919878
1.5	2.893	-M <sub>v</sub>	0.849	0.1384	0.0852	3.1297	0.8926	2.3783	0.16757804
		+M <sub>v</sub>	0.4625	0.0597	0.0232	1.487	0.1276	1.606	0.169347327
2.0	2.170	-M <sub>v</sub>	0.845	0.138	0.083	3.405	1.083	3.902	0.127056019
		+M <sub>v</sub>	0.469	0.061	0.022	1.672	0.043	2.710	0.124745763

Where:

M<sub>cs</sub>: Moment in column stripM<sub>ms</sub>: Moment in middle strip



**Table 2:** Comparison of Moment due to Unit Line Load and Corresponding Unit Uniformly Distributed Load (UDL) for Flat Plate Slab (see Fig. 3 and Fig 5):

Aspect Ratio	M <sub>v</sub>	Moments Due to a Unit Line Load ( $kN \times m/m$ )		Moments Due to Unit UDL ( $kN \times m/m$ )		Average  $\frac{W_{UDL}}{W_{Line}}$  = $\frac{M_{Line}}{M_{UDL}}$
		M <sub>cs</sub>	M <sub>ms</sub>	M <sub>cs</sub>	M <sub>ms</sub>	
0.5	-M <sub>v</sub>	2.9947	1.7753	12.541	6.986	0.244277155
	+M <sub>v</sub>	1.1853	1.0940	4.743	4.703	0.2412979040
0.75	-M <sub>v</sub>	0.7746	0.2627	2.3608	0.9114	0.3170038510
	+M <sub>v</sub>	0.3022	0.2068	0.8314	0.7435	0.323195123
1.0	-M <sub>v</sub>	1.380	0.430	7.00	2.027	0.2005095820
	+M <sub>v</sub>	0.553	0.257	2.338	1.716	.199802664
1.5	-M <sub>v</sub>	0.839	0.2791	5.3146	1.2997	0.169042831
	+M <sub>v</sub>	0.347	0.1514	1.3850	1.5686	0.168743229
2.0	-M <sub>v</sub>	0.840	0.278	7.432	1.446	0.125929263
	+M <sub>v</sub>	0.352	0.149	1.392	2.446	0.130536738

Where:

+M<sub>v</sub>: The positive moment

-M<sub>v</sub>: The negative moment

## REGRESSION ANALYSIS

Multiple regressions analysis have been executed to derive required relationship based on finite element results that summarized in Table 1 and Table 2. This has been executed by STATISTICA Software. Using  $\frac{W_{Eq.UDL}}{W_{Actual Line Load}}$  as dependent variable and  $\alpha$  and  $\frac{l_2}{l_1}$  as independent variables, linear regression relation will take the following form:

$$\frac{W_{Eq.UDL}}{W_{Actual Line Load}} = a_0 + a_1 \alpha + a_2 \frac{l_2}{l_1} \quad (2)$$

where:

$\alpha$  is the relative ratio of the stiffness of beam to slab,  $\frac{l_2}{l_1}$  is the aspect ratio.

$W_{UDL}/W_{Line}$  is the ratio of equivalent uniformly distributed load to actual line load.  $a_0$ ,  $a_1$ , and  $a_2$  are regression coefficients.

Based on finite element results and statistical model that proposed in Eq. (2), one can conclude that the general relation between actual line load and the equivalent uniformly distributed will be:

$$\frac{W_{Eq.UDL}}{W_{Actual Line Load}} = 0.32193 + 0.00473\alpha - 0.10175 \frac{l_2}{l_1} \quad (3)$$

It is useful to note that this relation has a multiple correlation coefficients (R) equal to 0.8327334. This gives an indication that there is an actual linear proportionality between the dependent and independent variables. To assess the effect of each one of independent variables, correlation coefficient (r) has been computed as shown in Fig. 6 and Fig. 7 (each Fig. for both types of Slab Systems) below:

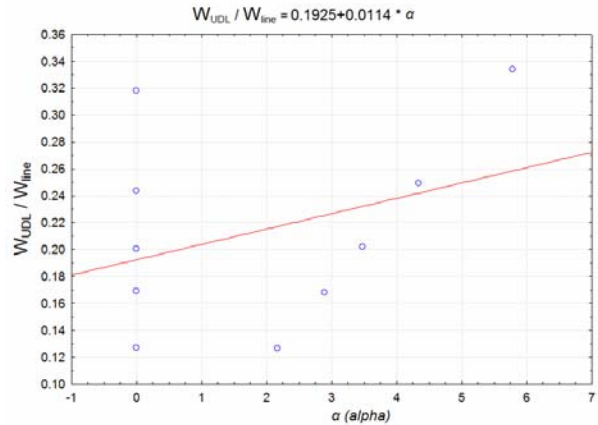


**Fig. 6**  
Relationship Between ( $W_{UDL}/W_{Line}$ ) and  $\alpha$ . (Relative stiffness of beam to slab)

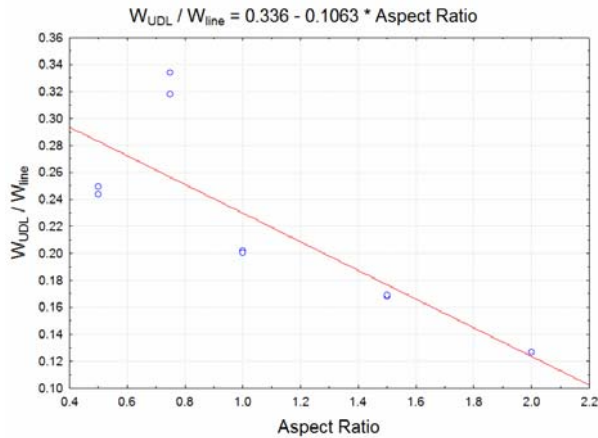


**Fig. 7**  
Relationship Between ( $W_{UDL}/W_{Line}$ ) and Aspect Ratio

## CONCLUSIONS

Based on finite element analyses and regression analyses that have been executed in this study, one can conclude that an accurate estimation of the uniformly distributed load that equivalent to a known line load should include parameters related to system type and beams relative stiffness (in there is any beam in the system) in addition to the value of the line load.

## REFERENCES:

- 1-Park R. and Gamble W. L. "Reinforced Concrete Slabs", John Wiley and Sons, Inc. 1980.
- 2-R. E. Woodring "Analytical Study of the Moments in Continuous Slabs Subjected to Concentrated Loads," Ph. D. thesis, University of Illinois at Urbana-Champaign, 1963, pp. 151.
- 3-الملحق رقم 1 للكوود العربي السوري لتصميم وتنفيذ المنشآت بالخرسانة المسلحة 2006
- 4-الكوود المصري لحساب الاحمال والقوى في الاعمال الانشائية واعمال المباني سبتمبر 2008
- 6-IBC, "International Building Code", 2003.
- 5-IBC, "International Building Code", 2006

## NOTATION:

$l_1$	Span under consideration (m)
$l_2$	Lateral span length (m)
$\bar{w}$	Weight of wall per unit length (kN/m).
$w^*$	Equivalent uniformly distributed load (kN/m <sup>2</sup> )
$\alpha, \beta$ and $\gamma$	Coefficients of regression
C	Concentration coefficient
L	Span of square panel (m).
R	Correlation coefficients
$W_{Line}$	The actual line loads (kN/m)
$W_{UDL}$	Equivalent uniformly distributed load (kN/m <sup>2</sup> ) for the actual line loads
$\alpha$	Relative ratio of the stiffness of beam to slab
$M_{cs}$	Moment in column strip
$M_{ms}$	Moment in middle strip
+M <sub>v</sub>	The positive moment
-M <sub>v</sub>	The negative moment

## Replacement of Line Loads acting on slabs to equivalent uniformly Distributed Loads

Ass.Prof.Dr.AbdulMuttalibI.Said  
abdmusawi@yahoo.com  
Department of Civil Engineering

College of Engineering  
University of Baghdad

Dr. Salah Rohaima Obed  
Email: salahalzaidee2004@gmail.com  
lecturer / Department of Civil Engineering

College of Engineering  
University of Baghdad

Salam Mreh Ayez  
Email:salamalkhafaji84@yahoo.com  
M. Sc. Student  
Department of Civil Engineering  
College of Engineering  
University of Baghdad

### Abstract

This study aims to derive a general relation between line loads that acting on two-way slab system and the equivalent uniformly distributed loads. This relation will be so useful to structural designer that are used to working with a uniformly distributed load and enable them to use the traditional methods for analysis of two-way systems (e.g. Direct Design Method).

Two types of slab systems, Slab System with Beams and Flat Slab Systems, have been considered in this study to include the effect of aspect ratio and type of slab on the proposed relation. Five aspect ratios,  $l_2/l_1$  of 0.5, 0.75, 1.0, 1.5 and 2.0, have been considered for both types of two-way systems.

All necessary finite element analyses have been executed with **SAFE Software**. Data obtained from the F. E. analyses have been used in a statistical analysis using **Statistic Software** to derive the relation based on a Linear Regression Analysis.

**Keywords:** Line Loads, Equivalent Uniformly Distributed Loads, Two-way Slabs, Flat Slabs, SAFE, Finite Element Analysis, Statistical Analysis, Linear Regression Analysis.

### أستبدال الأحمال الخطية المؤثرة على البلاطات الى احمال مكافئة موزعة بانتظام

سلام مريح عايز  
طالب ماجستير/مدني  
كلية الهندسة/ جامعة بغداد

د. صلاح رحيمه عبيد  
مدرس/قسم الهندسة المدنية  
كلية الهندسة / جامعة بغداد

أ.م.د. عبد المطلب عيسى سعيد  
مدرس/قسم الهندسة المدنية  
كلية الهندسة / جامعة بغداد

### الخلاصة:

تقدم هذه الدراسة بحثاً تحليلياً يخص تحويل الأحمال الخطية المسلطة على السقوف الخرسانية كأحمال الجدران الى أحمال منتشرة وموزعة بانتظام مكافئة للأحمال الأصلية ومؤثرة على كافة مساحة السقف وذلك لتسهيل عملية التصميم لهذه السقوف بطرق التصميم السائدة والمعدة بالاساس للأحمال الموزعة بانتظام كطرق التصميم الموجودة في المدونة الأمريكية (مثل طريقة التصميم المباشر).

تم أخذ نوعين من أكثر أنواع السقوف انتشاراً (السقوف المسندة على أعتاب خرسانية والسقوف المستوية) حيث تم دراسة أهم العوامل المؤثرة على العلاقة بين الحمل الخطي والحمل المنتشر المكافئ له ومن أهمها نسبة طول الفضاء الى طول الفضاء العمودي عليه وكذلك نسبة جساءة العتیب الى جساءة السقف (في النوع الاول فقط) حيث تم أخذ خمسة نسب من نسبة طول الفضاء الى طول الفضاء العمودي عليه (0.5, 0.75, 1.0, 1.5 و 2.0) لكل نوع منهما.

تم تسليط أحمال خطية مرة وموزعة بانتظام مرة أخرى على هذه السقوف وحلت بطريقة العناصر المحددة وبأستخدام برنامج: (SAFE Software V. 12).

ولإيجاد العلاقة بين الحمل الخطي والحمل الموزع بانتظام و المكافئ له تم الاعتماد على طريقة تحليل الانحدار حيث تم ادخال البيانات المستحصلة من تحليل الانظمة أعلاه الى البرنامج الاحصائي: (STATISTIC Software)

**الكلمات الرئيسية:** الأحمال الخطية، الأحمال المكافئة الموزعة بانتظام ، بلاطات ثنائية، بلاطات مستوية، تحليل السقوف بطريقة العناصر المحددة، التحليل بالعناصر المحددة، التحليل الإحصائي، تحليل الارتباط الخطي.

## INTRODUCTION

Line loads, as may be applied by walls, are a special case of loads acting on small areas. It has apparently been customary to take the weight of interior walls into account by adding an addition uniformly distributed loads of  $1.44 \text{ kN/m}^2$  to the dead load of the slab.<sup>(1)</sup>

**Woodring** <sup>(2)</sup> studied the effects of an arbitrary length placed concrete block wall weighing  $4.43 \text{ kN/m}$  ( $304 \text{ lb/ft}$ ) and extending to an arbitrary length. The wall was considered to have zero stiffness and hence to apply a uniform line load to the slab regardless of the slab deflection. Considering a single wall, the  $1.44 \text{ kN/m}^2$  ( $30 \text{ psf}$ ) allowance was more adequate than for any length and placement of the wall as far as the negative moments in beamless slabs were concerned. However, if the wall was placed at midspan and especially if it extends across several panels, the  $1.44 \text{ kN/m}^2$  ( $30 \text{ psf}$ ) allowance was inadequate for positive moments. When the wall extended across the full width of one panel, the required allowance to properly compensate for the effects on midspan moments acting in the direction perpendicular to the wall varied from  $3.2 \text{ kN/m}^2$  when  $l_1 = 6.1\text{m}$  to  $2.1 \text{ kN/m}^2$  when  $l_1 = 9.15\text{m}$ . If the wall extended across more than one panel, the required equivalent loads would be slightly larger. Thus, it may be desirable, if inconvenient; to design the positive-moment sections with one equivalent load and the negative-moment sections for another lower equivalent load. Then the equivalent uniformly distributed load can be computed by using the following equation <sup>(1)</sup>:

$$w^* = \frac{\bar{w}C}{L} \quad (1)$$

Where:

: is the equivalent uniformly distributed load per unit width.

: is the weight of wall per unit length.

: Span of square panel.

C: concentration coefficient, where a positive number indicates moments with the same sign as are caused by distributed loads.

According to Syrian Code<sup>(3)</sup>, the line loads light in weight can be replaced by an equivalent uniformly distributed load when the line loads on slab systems equal to or less than  $1.5 \text{ kN/m}^2$  on the area under wall and as shown in **Fig. 1**.

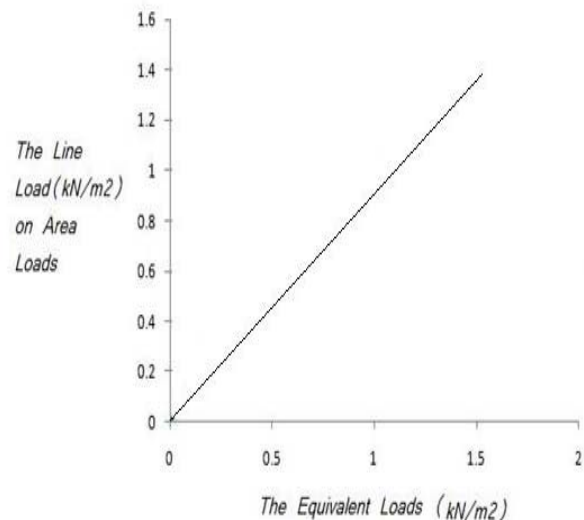


**Fig. 1**  
**Equivalent Uniform Loads to Line Loads <sup>(3)</sup>**

Also when the live load applied on slab systems is greater than a  $6 \text{ kN/m}^2$  the effect of the line loads can be neglected <sup>(3)</sup>.

According to Egyptian Code, when the design live loads is greater than or equal to  $5.0 \text{ kN/m}^2$  and the line loads equal to or less than  $1.0 \text{ kN/m}^2$ , line load effects can be neglected <sup>(4)</sup>.

According to the International Building Code, in the office and other buildings where partition locations are subjected to change, provision for partition weight shall be made, whether or not partitions are shown on the construction documents, unless the specified live load exceeds  $3.83 \text{ kN/m}^2$  (80 psf). Such the partition load shall not be less than a uniformly distributed live load of  $0.96 \text{ kN/m}^2$  (20 psf) (according to **IBC 2003**)<sup>(5)</sup> or  $0.74 \text{ kN/m}^2$  (15 psf) (according to **IBC 2006**)<sup>(6)</sup>.

### EQUIVALENT UNIFORM LOAD:

As discussed in the previous section, most of current methods for estimating the equivalent uniformly distributed load recommend a constant value of the equivalent uniformly distributed load that does not depend neither on the intensity of the original line load nor on system parameters (existence of beams, stiffness of beams, and panel aspect ratio). The main goal of this study is to develop a more rigorous relation that includes these effects into account. This has been started with finite element analyses of the two-way systems under a unit line loads and unit uniformly distributed loads. These finite element results had been used in a linear regression analysis to obtain the required general relation.

### FINITE ELEMENT ANALYSES:

Finite element analyses (executed by **SAFE Software**) for systems with following properties:

1. A Concrete slab of 0.2 m thick.
2. Concrete beams (for slab with beams) with dimensions of 0.4 m by 0.6 m and a relative flexural stiffnesses “ ” greater than two ( $\alpha \frac{I_2}{I_1}$ ).
3. All concrete columns have dimensions of 0.4 m by 0.4 m.

4. A line load of ( 1 ) and uniform distribution load ( $1 \text{ kN/m}^2$ ).
5. A square finite element mesh with dimensions of 20 cm by 20 cm.

Five different aspect ratios have been considered in each case study, namely 0.5, 0.75, 1.0, 1.5, and 2.0. Then the lengths will be  $l_2$  is 4, 3, 5, 6, and 8 and  $l_1$  is 8, 4, 5, 4, and 4.

For each aspect ratio, the system has been subjected to the following two load cases:

First Load Case: This load case intends to simulate the floor systems that subjected to quasi symmetrical line loads. Then in this load case all center lines in the direction under consideration have been subjected to line loads and as shown in **Fig. 2** for slab with beams and in **Fig. 3** for flat slab systems.

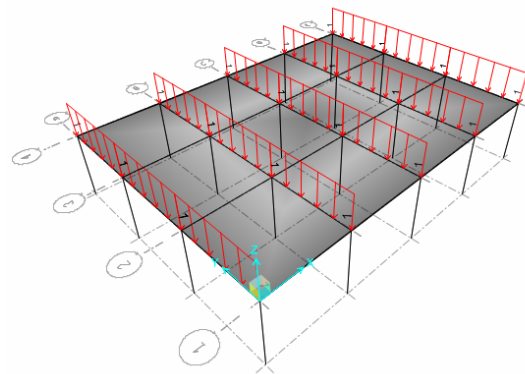


**Fig. 2:**  
Slab with beams subjected to unit line load (kN/m).

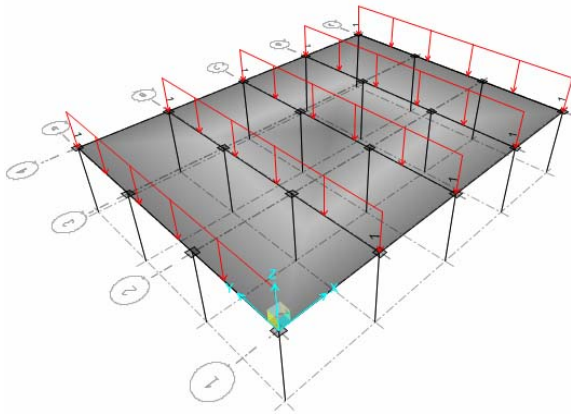


**Fig. 3:**  
Flat slab subjected to unit line load (kN/m).

In the second Load Case the re-analysis of these systems under a uniformly distributed load with unit load value as shown in **Fig. 4** for slab with beams and **Fig. 5** for flat slab systems to obtain the data in **Table 1** for slab with beams and then, to obtain **Table 2** for flat plat slabs.

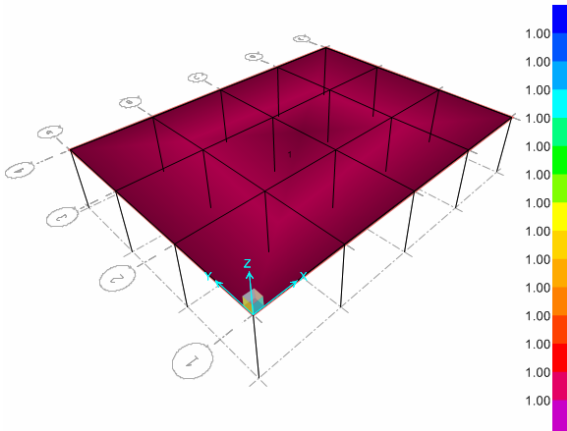


**Fig. 4:**

## Replacement of Line Loads acting on slabs To equivalent uniformly Distributed Loads

Slab with beams subjected to unit uniformly  
Distribution load (kN/m²).

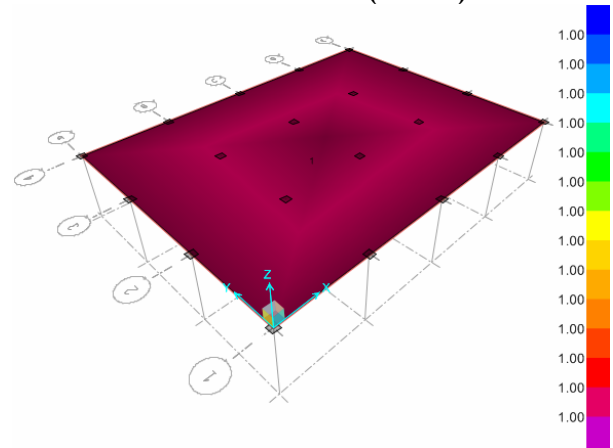


**Fig. 5:**  
Flat slab subjected to unit uniformly  
Distribution load (kN/m²).

In these Tables, the ratio  $W_{UDL}/W_{Line}$  Load has been computed as follows:

1. Based on linearity of structure:

$$M_{Due\ to\ Line\ Load} = M_{Unit\ Line\ Load} \times W_{Line}$$

$$M_{Due\ to\ UDL} = M_{Due\ to\ Unit\ UDL} \times W_{UDL}$$

2. Based on definition of the equivalent uniformly distributed load:

$$\therefore M_{Due\ to\ UDL} = M_{Due\ to\ Line\ Load}$$

$$\therefore M_{Unit\ UDL} \times W_{UDL} = M_{Unit\ Line\ Load} \times W_{Line}$$

$$\therefore \frac{W_{UDL}}{W_{Line}} = \frac{M_{Due\ to\ Unit\ Line\ Load}}{M_{Due\ to\ Unit\ UDL}}$$

**Table 1:** Comparison of Moment due to Unit Line Load and Corresponding Unit Uniformly Distributed Load (UDL) for Two-way Slabs with Beams (see Fig. 2 and Fig. 4):

Aspect Ratio	$\alpha$	M <sub>v</sub>	Moments Due to a Unit Line Load ( $kN \times m/m$ )			Moments Due to Unit UDL ( $kN \times m/m$ )			Average  $W_{UDL}/W_{Line}$  = $M_{Line}/M_{UDL}$
			M <sub>beam</sub>	M <sub>cs</sub>	M <sub>ms</sub>	M <sub>beam</sub>	M <sub>cs</sub>	M <sub>ms</sub>	
0.5	4.342	-M <sub>v</sub>	4.24	0.511	0.418	16.19	2.229	2.365	0.248700924
		+M <sub>v</sub>	1.683	0.181	0.159	6.595	0.527	0.905	0.252024418
0.75	5.787	-M <sub>v</sub>	0.877	0.1194	0.0814	2.3515	0.418	0.465	0.333219972
		+M <sub>v</sub>	0.4579	0.0484	0.0345	1.2341	0.0954	0.2793	0.336151169
1.0	3.742	-M <sub>v</sub>	1.451	0.250	0.133	5.676	1.513	1.932	0.201074444
		+M <sub>v</sub>	0.664	0.100	0.043	2.473	0.338	1.108	0.205919878
1.5	2.893	-M <sub>v</sub>	0.849	0.1384	0.0852	3.1297	0.8926	2.3783	0.16757804
		+M <sub>v</sub>	0.4625	0.0597	0.0232	1.487	0.1276	1.606	0.169347327
2.0	2.170	-M <sub>v</sub>	0.845	0.138	0.083	3.405	1.083	3.902	0.127056019
		+M <sub>v</sub>	0.469	0.061	0.022	1.672	0.043	2.710	0.124745763

Where:

M<sub>cs</sub>: Moment in column stripM<sub>ms</sub>: Moment in middle strip



**Table 2:** Comparison of Moment due to Unit Line Load and Corresponding Unit Uniformly Distributed Load (UDL) for Flat Plate Slab (see Fig. 3 and Fig 5):

Aspect Ratio	M <sub>v</sub>	Moments Due to a Unit Line Load ( $kN \times m/m$ )		Moments Due to Unit UDL ( $kN \times m/m$ )		Average  $\frac{W_{UDL}}{W_{Line}}$  = $\frac{M_{Line}}{M_{UDL}}$
		M <sub>cs</sub>	M <sub>ms</sub>	M <sub>cs</sub>	M <sub>ms</sub>	
0.5	-M <sub>v</sub>	2.9947	1.7753	12.541	6.986	0.244277155
	+M <sub>v</sub>	1.1853	1.0940	4.743	4.703	0.2412979040
0.75	-M <sub>v</sub>	0.7746	0.2627	2.3608	0.9114	0.3170038510
	+M <sub>v</sub>	0.3022	0.2068	0.8314	0.7435	0.323195123
1.0	-M <sub>v</sub>	1.380	0.430	7.00	2.027	0.2005095820
	+M <sub>v</sub>	0.553	0.257	2.338	1.716	.199802664
1.5	-M <sub>v</sub>	0.839	0.2791	5.3146	1.2997	0.169042831
	+M <sub>v</sub>	0.347	0.1514	1.3850	1.5686	0.168743229
2.0	-M <sub>v</sub>	0.840	0.278	7.432	1.446	0.125929263
	+M <sub>v</sub>	0.352	0.149	1.392	2.446	0.130536738

Where:

+M<sub>v</sub>: The positive moment

-M<sub>v</sub>: The negative moment

## REGRESSION ANALYSIS

Multiple regressions analysis have been executed to derive required relationship based on finite element results that summarized in Table 1 and Table 2. This has been executed by STATISTICA Software. Using  $\frac{W_{Eq.UDL}}{W_{Actual Line Load}}$  as dependent variable and  $\alpha$  and  $\frac{l_2}{l_1}$  as independent variables, linear regression relation will take the following form:

$$\frac{W_{Eq.UDL}}{W_{Actual Line Load}} = a_0 + a_1 \alpha + a_2 \frac{l_2}{l_1} \quad (2)$$

where:

$\alpha$  is the relative ratio of the stiffness of beam to slab,  $\frac{l_2}{l_1}$  is the aspect ratio.

$W_{UDL}/W_{Line}$  is the ratio of equivalent uniformly distributed load to actual line load.  $a_0$ ,  $a_1$ , and  $a_2$  are regression coefficients.

Based on finite element results and statistical model that proposed in Eq. (2), one can conclude that the general relation between actual line load and the equivalent uniformly distributed will be:

$$\frac{W_{Eq.UDL}}{W_{Actual Line Load}} = 0.32193 + 0.00473\alpha - 0.10175 \frac{l_2}{l_1} \quad (3)$$

It is useful to note that this relation has a multiple correlation coefficients (R) equal to 0.8327334. This gives an indication that there is an actual linear proportionality between the dependent and independent variables. To assess the effect of each one of independent variables, correlation coefficient (r) has been computed as shown in Fig. 6 and Fig. 7 (each Fig. for both types of Slab Systems) below:

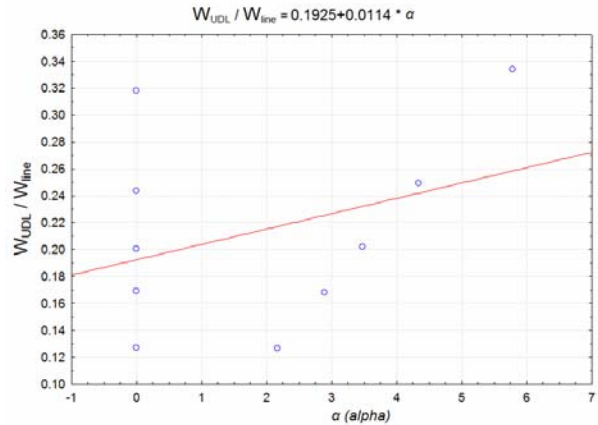


**Fig. 6**  
Relationship Between ( $W_{UDL}/W_{Line}$ ) and  $\alpha$ . (Relative stiffness of beam to slab)

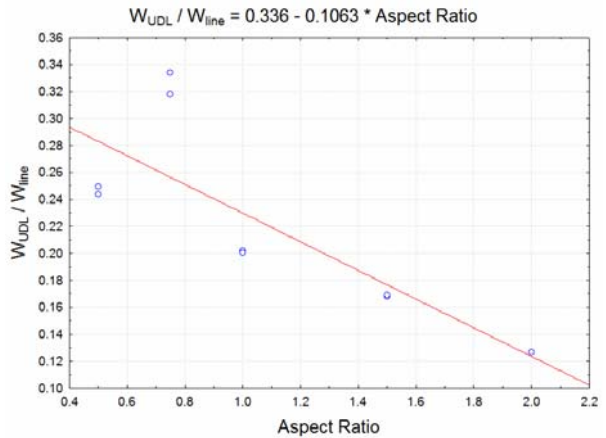


**Fig. 7**  
Relationship Between ( $W_{UDL}/W_{Line}$ ) and Aspect Ratio

## CONCLUSIONS

Based on finite element analyses and regression analyses that have been executed in this study, one can conclude that an accurate estimation of the uniformly distributed load that equivalent to a known line load should include parameters related to system type and beams relative stiffness (in there is any beam in the system) in addition to the value of the line load.

## REFERENCES:

- 1-Park R. and Gamble W. L. "Reinforced Concrete Slabs", John Wiley and Sons, Inc. 1980.
- 2-R. E. Woodring "Analytical Study of the Moments in Continuous Slabs Subjected to Concentrated Loads," Ph. D. thesis, University of Illinois at Urbana-Champaign, 1963, pp. 151.
- 3-الملحق رقم 1 للكوود العربي السوري لتصميم وتنفيذ المنشآت بالخرسانة المسلحة 2006
- 4-الكوود المصري لحساب الاحمال والقوى في الاعمال الانشائية واعمال المباني سبتمبر 2008
- 6-IBC, "International Building Code", 2003.
- 5-IBC, "International Building Code", 2006

## NOTATION:

$l_1$	Span under consideration (m)
$l_2$	Lateral span length (m)
$\bar{w}$	Weight of wall per unit length (kN/m).
$w^*$	Equivalent uniformly distributed load (kN/m <sup>2</sup> )
$\alpha, \beta, \gamma$	Coefficients of regression
C	Concentration coefficient
L	Span of square panel (m).
R	Correlation coefficients
$W_{Line}$	The actual line loads (kN/m)
$W_{UDL}$	Equivalent uniformly distributed load (kN/m <sup>2</sup> ) for the actual line loads
$\alpha$	Relative ratio of the stiffness of beam to slab
$M_{cs}$	Moment in column strip
$M_{ms}$	Moment in middle strip
+M <sub>v</sub>	The positive moment
-M <sub>v</sub>	The negative moment

## Surface Free Energy for the Evaluation of Asphalt Binder Stripping

Prof. Saad Issa Sarsam and Esraa Thamer Al – Azawee  
saadisasarsam@coeng.uobaghdad.edu.iq  
College of Engineering/ University of Baghdad

### Abstract

Stripping is one of the major distresses within asphalt concrete pavements caused due to penetration of water within the interface of asphalt-aggregate matrix. In this work, one grade of asphalt cement (40-50) was mixed with variable percentages of three types of additives (fly ash, fumed silica, and phosphogypsum) to obtain a modified asphalt cement to resist the effect of stripping phenomena. The specimens have been tested for physical properties according to AASHTO. The surface free energy has been measured by using two methods namely, the Wilhelmy technique and the Sessile drop method according to NCHRP-104 procedures.

Samples of asphalt concrete using different asphalt cement and modified asphalt cement percentages (4.1, 4.6 and 5.6) were prepared and tested for stripping phenomena by using Marshall Immersion method (The index of retained stability test (I.R.S)  $\geq 75\%$ ).

When using Sessile drop method the value of surface free energy of asphalt cement grade (40-50) was about  $8.8 \text{ ergs/cm}^2$ , while when using Wilhelmy technique the value of surface free energy of asphalt cement was  $30.71 \text{ ergs/cm}^2$ .

Finally, a mathematical relationship was obtained by using (SPSS) Software between the stripping asphalt concrete using conditioned and unconditioned specimens data (I.R.S) %, the contact angle, the total surface free energy for asphalt cement and modified asphalt cement with fume silica.

**Keywords:** Stripping, surface free energy, modified asphalt, fume silica

### تقييم خصائص التقشر للأسفلت السمنتي باستخدام مبدأ الطاقة السطحية الحرة

تقشر الأسفلت عن الركام هو أحد المشاكل الرئيسية التي تضعف الخرسانة الأسفلتية وذلك بسبب تغلغل الماء إلى سطح الأسفلت والركام. في هذا البحث تم مزج نوع واحد من الأسفلت السمنتي (40-50) مع نسب متغيرة من ثلاثة أنواع من المضافات (الرماد المتطاير والفيوم سليكا والفوسفوجبسوم) للحصول على أسفلت سمنتي محسن.

تم فحص النماذج للخصائص الفيزيائية اتباعاً لمواصفة AASHTO الأمريكية للأسفلت السمنتي والمحسن و تم قياس الطاقة السطحية الحرة باستخدام طريقتي (Wilhelmy Method and Sessile Drop) بموجب مواصفة (NCHRP-104).

تم فحص نماذج الخرسانة الأسفلتية لأنواع الأسفلت السمنتي والأسفلت المحسن بالنسب 4.1, 4.6, 5.6 لقياس ظاهرة التقشر باستخدام طريقة Marshall Immersion لإيجاد مؤشر بقاء الاستقرار (I.R.S. %). ومن نتائج الفحوصات لوحظ أن طاقة الشد السطحي للأسفلت السمنتي (40-50) المحسوب بطريقة Sessile Drop كانت  $8.8 \text{ ergs/cm}^2$  بينما أعطت طريقة Wilhelmy Method طاقة الشد السطحي المحسوبة بمقدار  $30.71 \text{ erg/cm}^2$ . وتم إيجاد علاقات رياضية تربط ظاهرة التقشر للنماذج (Conditioned and unconditioned) و (contact angle) مع طاقة الشد السطحي للأسفلت المحسن بالفيوم سليكا.

**الكلمات الرئيسية:** التقشر ، الطاقة السطحية الحرة ، الأسفلت المحسن ، أبخره السليكا.

## Introduction

### General

Moisture damage in asphalt concrete pavements is considered as primary cause of distresses in the asphalt pavement layers. The exposure of asphalt pavement to water is often one of the major factors affecting the durability of HMA. The water induced damage in HMA layers may be associated with two mechanisms: loss of adhesion and/loss of cohesion. In the first mechanism, the water gets trapped between the asphalt and aggregate and strips the asphalt film away, leaving aggregate without asphalt film coverage. This happens because the aggregates have a greater affinity for water than asphalt binder. The second mechanism includes the interaction of water with the asphalt cement that reduces the cohesion within the asphalt cement. This will lead to a severe reduction in the asphalt mixture strength. (Wasiuddin, (2007)).

Mineral anti-stripping additives and liquid anti-stripping agents are commonly used to modify hot mix asphalt HMA components, asphalt binder and aggregate, to increase the resistance of HMA mixtures to moisture damage. Surface free energy, of a material is the amount of work required to create unit area of the material in vacuum. The total surface energy of a material is divided into three components, namely, the Lifshitz-van der Waals component, the acid component, and the base component. Such components can be used in calculating the free surface energy for asphalt (NCHRP-104), and there are several methods to determine the surface energy.

### Methods for Determination of Surface Free Energy of Asphalt:

- Sessile Drop Method (SDM).
- Wilhelmy Plate Method (WPM).

### Research Objective

The main objectives of this research work are:

(1). Studying the relationship between the surface free energy and stripping properties for asphalt cement and modified asphalt improved by three types of additives (fly ash, phpsphogypsum and fume silica). The source of fly ash is locally from the waste of factories, phospho gypsum from

Phosphate plant usually available as waste, fume silica obtained from local market.

(2). Finding a mathematical relationship between the stripping of asphalt concrete using conditioned and unconditioned specimens data with (I.R.S) and the contact angle and the total surface free energy for asphalt cement and modified asphalt cement.

### Stripping Test

#### Marshall Immersion Test:

Three sets of Marshall Specimens were prepared according to the method described by ASTM D 1559. Each set contains four groups (two Specimens, one dried (control) and another (condition). The Marshall Specimens were used to find the Index of Retained Stability (I.R.S) %. Each group contains two specimens subgroup; one is the average of three specimens (control specimens) which were subjected to immersion in water bath at 60 °C for 30 minute. The second is the average of three specimens (conditioned specimen) and were immersed in water bath at 14±2°C for 24 hrs. Such procedure was also followed by Zhou et al (2009) and Solaimanian et al (2003).

Then the specimens were tested by using Marshall Device .The index of retained stability was calculated as the ratio of stability of water exposed specimens to the stability of control specimens using equation (1).Yousif, (2003).

$$I.R.S (%) = \frac{s_2}{s_1} \times 100 \quad (1)$$

Where:

S<sub>1</sub>=Marshall Stability for control specimen (30 minutes immersion at 60 °C).

S<sub>2</sub>=Marshall Stability for condition specimen (24 hours immersion at 14±2 °C, then 30 minutes immersion in water at 60 °C).

A minimum I.R.S (%) of 75% is often specified for satisfactory resistance to damage by moisture. Yousif (2003).

Figure (1) show the gradation of aggregate used for wearing course(SCRB)

## Test Methods to Measure Surface Energy Components:

Surface energy is defined as the energy needed to create a new unit surface area of material in vacuum condition. Surface energy measurements are used to compute the adhesive bond strength between the aggregates and asphalt and cohesive bond strength in the binder. It is a suitable method for forecasting the moisture damage in asphalt mixtures. Therefore, this method seems to be capable of analyzing the effects of anti-stripping additives on the reduction of moisture damage. The ability to accurately determine surface free energy of asphalt binders and aggregates has been developed based on the **Van Oss theory. Cheng (2002)**. **Table (1)** shows the Surface Energy Components of the Probe Liquids used throughout this investigation. **Figure (2)** shows the flow chart of the surface energy determination.

The total surface energy of a material is divided into three components, namely, the Lifshitz-van der Waals component, the acid component, and the base component **Cheng (2002)**. The surface free energy,  $\gamma^{\text{total}}$  of a material is determined by combining the polar and nonpolar components as follows:

$$\gamma^{\text{total}} = \gamma^{\text{LW}} + 2\sqrt{\gamma^+ \gamma^-} \quad (2)$$

Where:

$\gamma^{\text{total}}$  = is the total surface free energy of the material.

$\gamma^{\text{LW}}$  = the Lifshitz-van der Waals.

$\gamma^+$  = is the Lewis acid component.

$\gamma^-$  = is the Lewis base component.

Several methods are proposed in the literature to measure the surface free energy of the asphalt-aggregate system. **Shah (2003)** studied the surface energy that aimed at assessing moisture damage. **Wasiuddin et al (2005)** studied that (SFE) of A HMA mix and its constituents (aggregate and binder) can be a valuable indicator of moisture damage in HMA. **Hefer; et al (2006)** studied the bitumen surface energy using contact angles measured with various liquids by the Wilhelmy plate.

## Wilhelm Plate Device Method(WPD)

This method is used to measure dynamic contact angles of the asphalt binder with various probe liquids and to determine surface energy components of the binder. A glass slide (25.4mm × 76.2mm × 1mm) coated with the asphalt binder and suspended from a microbalance is immersed in a probe liquid. From simple force equilibrium conditions the contact angle of the probe liquid with the surface of the asphalt binder can be determined. **Bhasin et al (2007)**

The difference between weight of a plate measured in air and partially submerged in a probe liquid,  $\Delta F$ , is expressed in terms of buoyancy of the liquid, liquid surface energy, contact angle, and geometry of the plate **Bhasin et al (2007)**. The contact angle between the liquid and surface of the plate is calculated from this equilibrium as follows:

$$\cos \theta = \frac{\Delta F + V_{im}(\rho_L - \rho_{air}g)}{P_L \gamma_L^{\text{Tot}}} \quad (3)$$

Where:

$P_L$  = is the perimeter of the bitumen coated plate.

$\gamma_L^{\text{Tot}}$  = Is the total surface energy of the liquid.

$\theta$  = The dynamic contact angle between the asphalt binder and the liquid.

$V_{im}$  = The volume immersed in the liquid.

$\rho_L$  = The density of the liquid.

$\rho_{air}$  = The air density.

$g$  = The local acceleration due to gravitation.

The analysis for obtaining the contact angle is usually carried out by using the software of the testing device. Since the testing device was not available in our laboratory, a manual test procedure was followed instead of using the device. The glass slides were of dimensions (25.4mm × 76.2mm × 1mm) each was coated

with asphalt binder or modified asphalt. Each slide was then immersed in the beaker that was filled with the different probe liquids slowly at a



steady speed and then a picture was taken while the slide was in its last position in the liquid.

The digital balance with a capacity of (1000 g) was used having a sensitivity of 0.2gm. The glass beaker that is filled with probe liquid was placed on the balance and then was covered together with the balance to prevent the air effect. Then, the glass slide was linked with a clipper paper and downloaded at slow and steady speed inside the beaker. The balance reading was taken when the slide touches the liquid. However, the balance was not sensitive enough for this measurement and it was not possible to determine the value of the  $\Delta F$  during the immersion and lifting and hence, Equation (3) cannot be used. Therefore the image processing software (**Comef 4.3**) was used to find a dynamic contact angle. A total number of slides were perpetrated of (48) slides. **Arabani (2010)** explained the theoretical and experimental concept of predicting moisture damage in asphalt concrete mixes by using the surface free energy (SFE) concept using dynamic Wilhelmy plate method. **Figure (3)** shows the contact angle between probe liquid and glass slide coated asphalt. A total number of slides were perpetrated of (48) slides.

### Sessile Drop Method(SDM)

A probe liquid is dispensed over a smooth horizontal surface coated with asphalt binder. The image of the drop of liquid formed over the surface of the binder is captured by using a digital camera. Contact angles are obtained by analyzing the image using image processing software (**Comef 4.3**) software. A static Contact angles measured with different probe liquids are used with equations of work of adhesion to determine the three surface energy components of the asphalt binder. [**NCHRP -104(2006)**], A total number of slides were perpetrated of (48) slides.

A drop with a contact angle over 90° is hydrophobic. This condition is exemplified by poor wetting, poor adhesiveness and the solid surface free energy is low. A drop with a small contact angle is hydrophilic this condition reflects better wetting, better adhesiveness, and higher surface energy. **Figure (4)** shows the Output of the Comef 4.3 Software

### Computing Surface Energies from Contact Angles

The surface energy component of a solid surface is determined by measuring its contact angles with various probe liquids. Typically more than three liquids are recommended to determine the three surface energy components of the solid. At least three probe liquids are recommended to be used in this test. These are water, glycerol, and formamid and all reagents must be high-purity grade (>99%). Contact angles must be measured for at least three replicates with each probe liquid for each type of asphalt binder and modifier asphalt. Probe liquids that have been selected not react chemically or dissolve with asphalt binders and are used to measure the contact angles with the binder.

The system of linear equations generated based on the above equations is shown below:

$$A \times B \quad (4)$$

Where:

$$A = \begin{bmatrix} \sqrt{\gamma_{li}^{LW}} & \sqrt{\gamma_{li}^+} & \sqrt{\gamma_{li}^-} \\ \dots & \dots & \dots \\ \sqrt{\gamma_{lm}^{LW}} & \sqrt{\gamma_{lm}^+} & \sqrt{\gamma_{lm}^-} \end{bmatrix} (m \times 3) \quad (5)$$

$$X = \begin{bmatrix} \sqrt{\gamma_s^{LW}} \\ \sqrt{\gamma_s^+} \\ \sqrt{\gamma_s^-} \end{bmatrix} (3 \times 1) \quad (6)$$

$$B = 0.5 \begin{bmatrix} \gamma_{li}(1 + \cos\theta_l) \\ \dots \\ \gamma_{li}(1 + \cos\theta_m) \end{bmatrix} (m \times 1) \quad (7)$$

$$x = A^{-1}B \quad (8)$$

The propagated variance of error in the work of adhesion can be calculated for each liquid as follows in Equation (10) and a reasonable approximation of  $\sigma_y$  is 0.1ergs/cm<sup>2</sup>

$$\sigma_w^2 = \sigma_y^2 \{0.5(1 + \cos\theta)\}^2 + \frac{1}{r} \frac{1}{(r-1)} \sum_{k=1}^r (\theta_k - \bar{\theta})^2 \{-0.5 \gamma \sin \bar{\theta}\}^2 \quad (10)$$

Where,  $\gamma$  is the total surface free energy value of the liquid shown in table (1),  $\bar{\theta}$  is the average contact angle from  $r$  replicate measurements in radian,  $\theta_k$  is the contact angle from  $r$  replicate

measurements.  $\sigma_{\theta}^2$  is the variance  $\theta$  expressed in radians shown in Equation (3.10)

$$\sigma_{\theta}^2 = \frac{1}{r(r-1)} \sum_{k=1}^r (\theta_k - \bar{\theta})^2 \{-0.5 \gamma \sin \theta\}^2 \quad (11)$$

The matrices **A** and **B** are changed as follows:

$$A' = \begin{bmatrix} \frac{\sqrt{\gamma_{11}^{LW}}}{\sigma_1} & \frac{\sqrt{\gamma_{11}^+}}{\sigma_1} & \frac{\sqrt{\gamma_{11}^-}}{\sigma_1} \\ \dots & \dots & \dots \\ \frac{\sqrt{\gamma_{1m}^{LW}}}{\sigma_m} & \frac{\sqrt{\gamma_{1m}^+}}{\sigma_m} & \frac{\sqrt{\gamma_{1m}^-}}{\sigma_m} \end{bmatrix} (m \times 3) \quad (12)$$

$$B' = 0.5 \begin{bmatrix} \frac{\gamma_{11}(1+\cos\theta_1)}{\sigma_m} \\ \dots \\ \frac{\gamma_{11}(1+\cos\theta_1)}{\sigma_m} \end{bmatrix} (m \times 1) \quad (13)$$

Then, determine the  $(A'^T A')^{-1}$  matrix for each asphalt binder. The three diagonal elements of this matrix ( $c_{ii}$ ) represent the variance of the square roots of the surface energy components (Lifshitz-van der Waals, base and acid component, respectively).

The variance estimate of the errors in the surface free energy components is obtained by propagation of errors as follows:

$$\gamma_{LW}^2 = 4X_i^2 C_{ii} \quad (14)$$

$$\gamma_{base(\gamma^-)}^2 = 4X_i^2 C_{ii} \quad (15)$$

$$\gamma_{LWacid(\gamma^+)}^2 = 4X_i^2 C_{ii} \quad (16)$$

Where,  $c_{ii}$  are diagonal elements of the  $(A'^T A')^{-1}$  matrix.

### Determination of Physical Properties:

In table (3) shows the physical properties of asphalt cement and modified asphalt cement were determined by using the following equations and shell nomograph. The table below illustrates such properties, Sarsam et al (2000).

$$\text{Penetration Index (P.I.)} = \left[ \frac{30}{(1+90k)} \right] - 10 \quad (17)$$

$$k = \frac{\log 800 - \log \text{penetration at } 77^\circ F}{[\text{ring and ball (softening point } ^\circ F) - 77^\circ F]} \quad (18)$$

The value of penetration index indicates greater temperature susceptibility. Stiffness modules (SM) defines as the ratio stress/strain was obtained from shell nomograph at  $T_{R\&B}$  75°C and temperature of asphalt at 25°C and a frequency of 10 Hz.

### Effect of Additives on Calculated Surface Free Energy by Sessile Drop Method

Surface free energy was determined for each type of asphalt binder based on Van Oss theory which separates the surface energy of asphalt into three components, namely, the Lifshitz-Van Der Waals component, the acid component, and the base component. Figures (5), (6) and (7) show the histograms of surface free energy of asphalt and modified asphalt. The surface free energy calculated was randomly when using asphalt modified with fly ash, fume silica and phosphor gypsum.

### Effect of Additives on Calculated Surface Free Energy by Wilhelmy Plate Method

Surface free energy was determined for each type of asphalt binder based on Van Oss theory which separates the surface energy of asphalt into three components, namely, the Lifshitz-Van Der Waals component, the acid component, and the base component. Figures (8), (9) and (10) show the histograms of surface free energy of asphalt and modified asphalt. The surface free energy calculated was randomly when using asphalt modified with fly ash, fume silica and phosphor gypsum.

### Effect of Additives on Stripping Potential Using Marshall Immersion Test

The index of retained stability (I.R.S) % was calculated as the ratio of stability of water exposed specimens to the stability of dry specimens. A minimum I.R.S (%) of 75% is often specified for satisfactory resistance to damage by moisture. Figures (11),(12),(13) ,(14) ,(15) and (16) show the relationship between contact angle of water and (I.R.S) % and total surface free energy of asphalt cement (40-50) modified with fumesilica



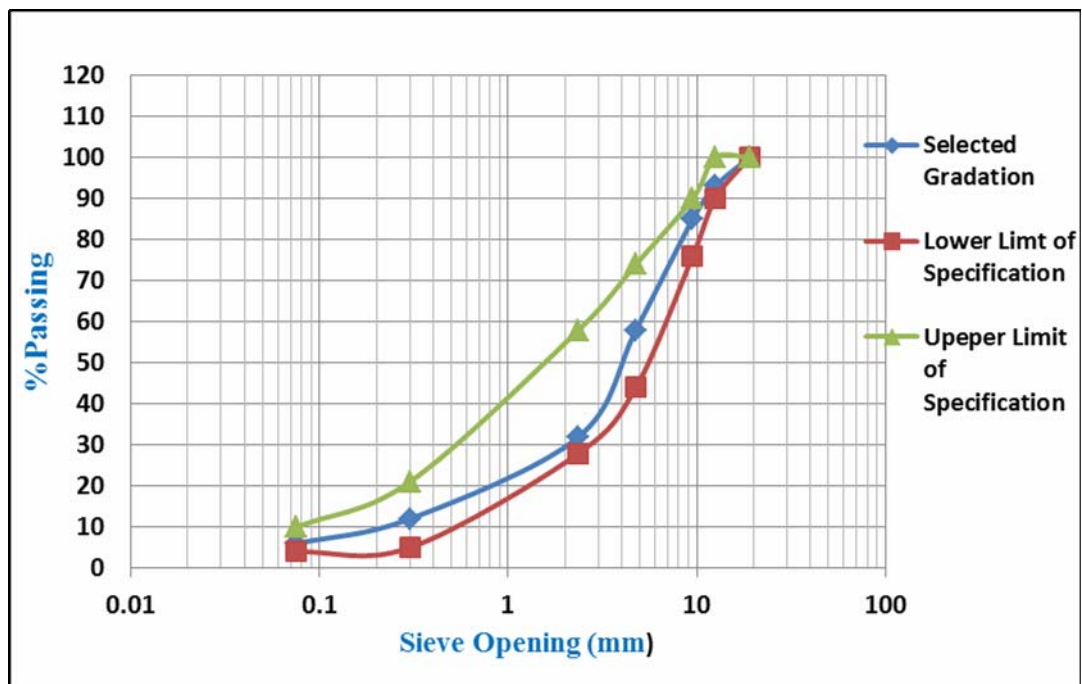


**Figure (1)** Gradation Curve of Aggregate Used for Wearing Course(SCRB)

### *Flow Chart of the Surface Energy Determination*

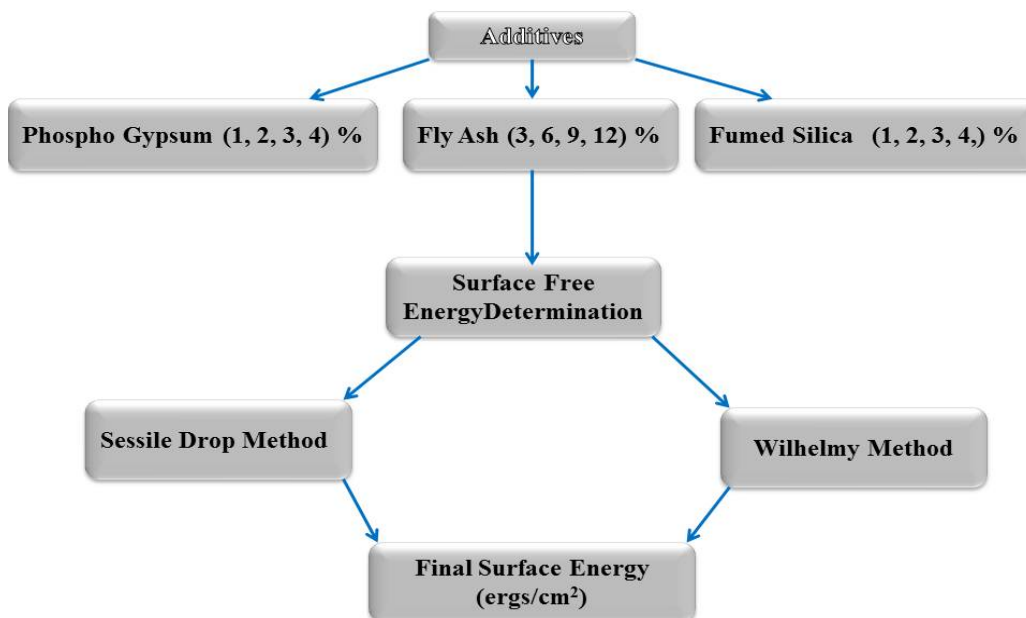


**Figure (2)** Flow Chart of the Surface free Energy Determination.

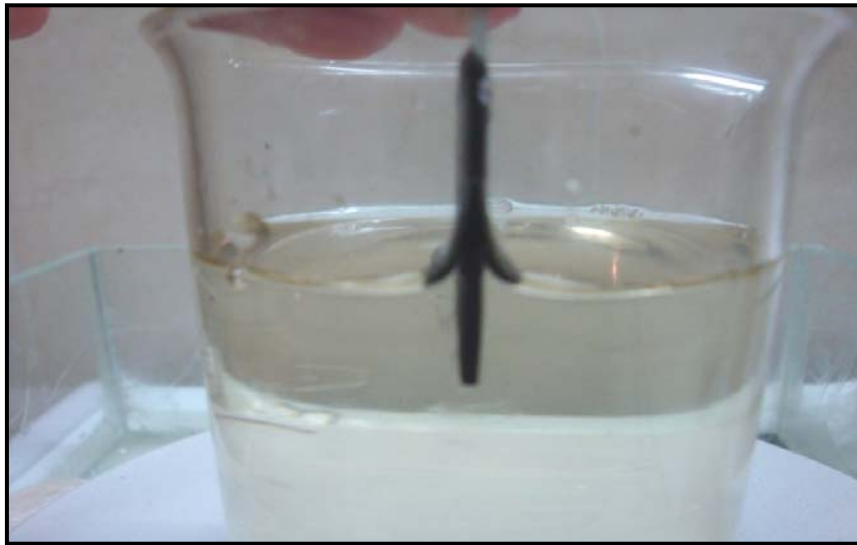


**Figure (3)** Contact Angle between Probe Liquid and Glass Slide Coated Asphalt

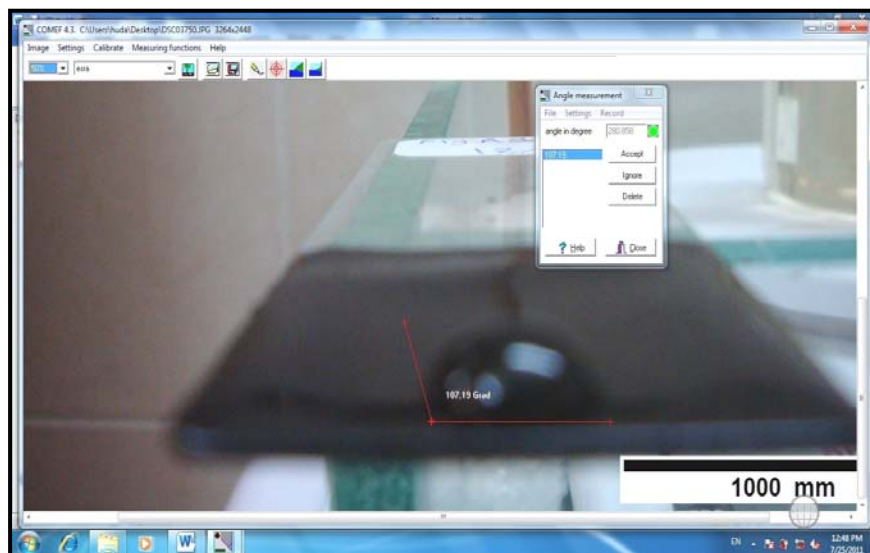


**Figure (4)** Output of the Comef 4.3 Software

**Table (1)** Surface Energy Components of the Probe Liquids [NCHRP 104 (2006)]

Probe Liquid	$\gamma_{\square\square}$	$\gamma^+$	$\gamma^-$	$\gamma^{\text{Total}}(\text{ergs/cm}^2)$	Density $\text{g/cm}^3$
Water	21.8	25.5	25.5	72.80	0.997
Formamid	39.0	2.28	39.6	58.00	1.134
Glycerol	34.0	3.92	57.4	64.00	1.258

**Table (2)** Physical properties of Modified Asphalt Grade (40-50)

Asphalt(40-50)	penetration	Softening point (C°)	PI	SM(N/m <sup>2</sup> )
<b>control</b>	46	51	-0.022	1.0x10 <sup>8</sup>
<b>Fume Silica 1%</b>	62	52	0.722	8x10 <sup>7</sup>
<b>2%</b>	47	51	-0.193	1.8x10 <sup>8</sup>
<b>3%</b>	37	57	0.491	9x10 <sup>7</sup>
<b>4%</b>	39	58	0.798	0.5x10 <sup>8</sup>
<b>Phospho1%</b>	26	52	-1.198	5.5x10 <sup>8</sup>
<b>2%</b>	30	53	-0.728	3.0x10 <sup>8</sup>
<b>3%</b>	33	55	-0.138	2.0x10 <sup>8</sup>
<b>4%</b>	44	57	0.889	6x10 <sup>7</sup>
<b>Fly ash 3%</b>	49.6	51.5	0.0671	1.9x10 <sup>8</sup>
<b>6%</b>	55.41	52	1.0517	4.3x10 <sup>7</sup>
<b>9%</b>	62	53.5	1.0517	5.0x10 <sup>7</sup>
<b>12%</b>	61.5	53.7	1.107	4.8x10 <sup>7</sup>

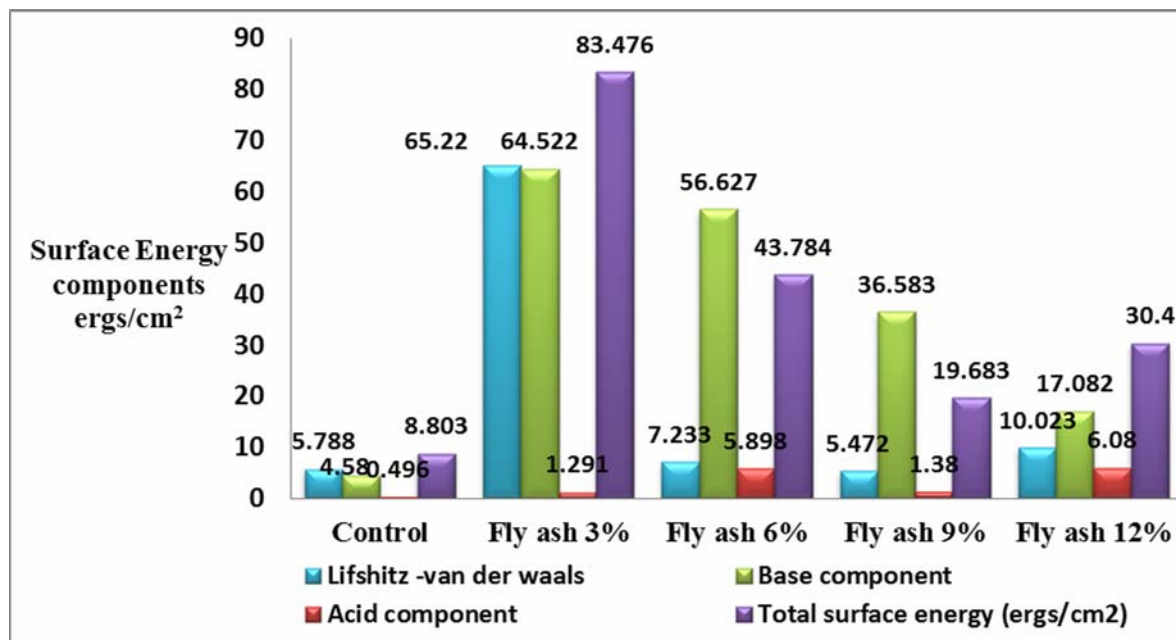


**Figure (5)** Effect of Fly ash on Surface Energy component of Asphalt binder by Sessile Drop Method

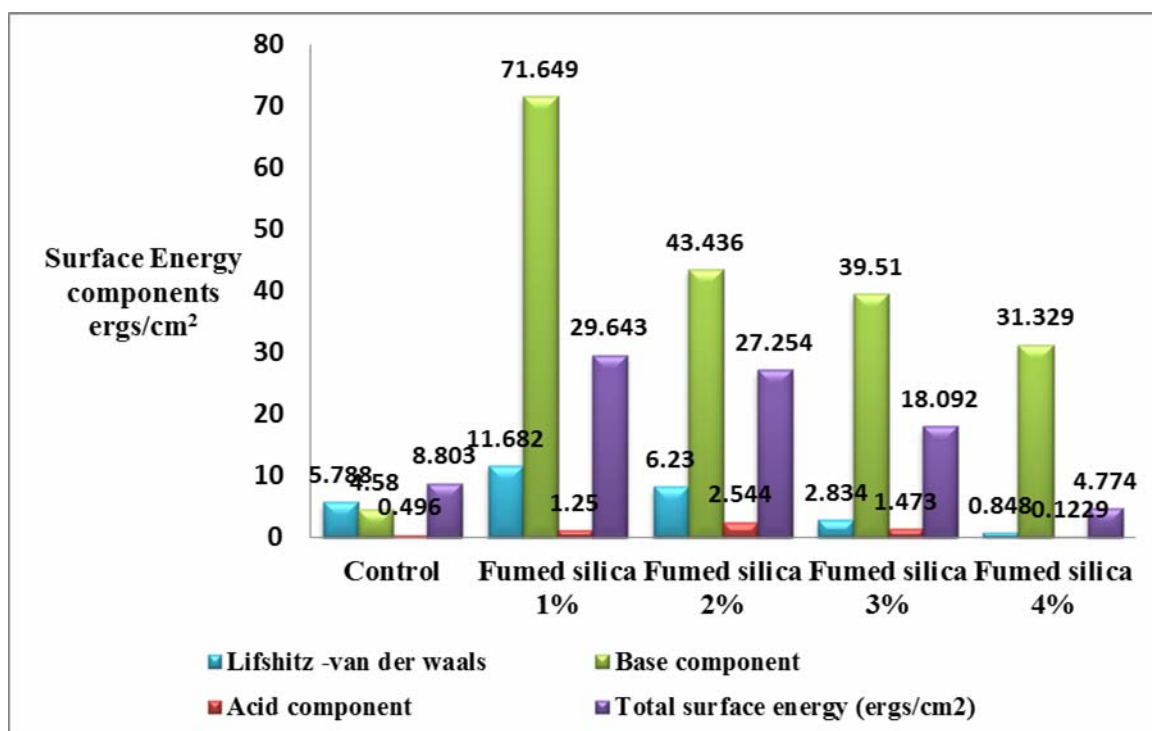


**Figure (6)** Effect of Fumed silica on Surface Energy component of asphalt binder by Sessile Drop Method

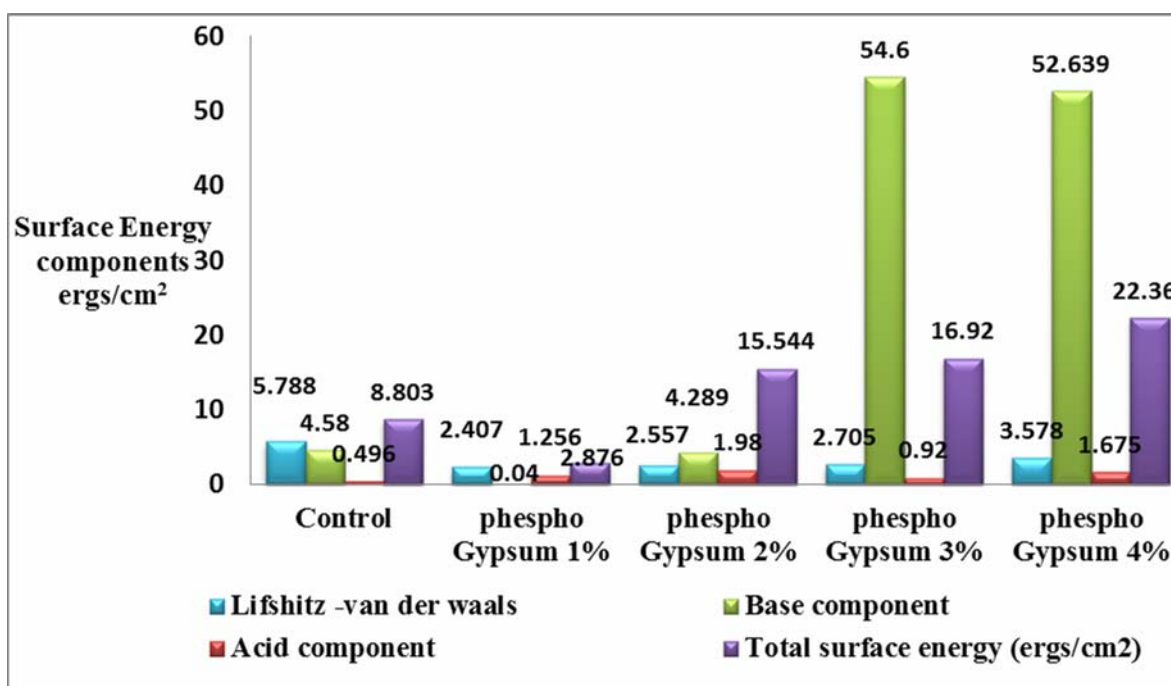


**Figure (7)** Effect of Phospho Gypsum on Surface Energy component of asphalt binder by Sessile Drop Method

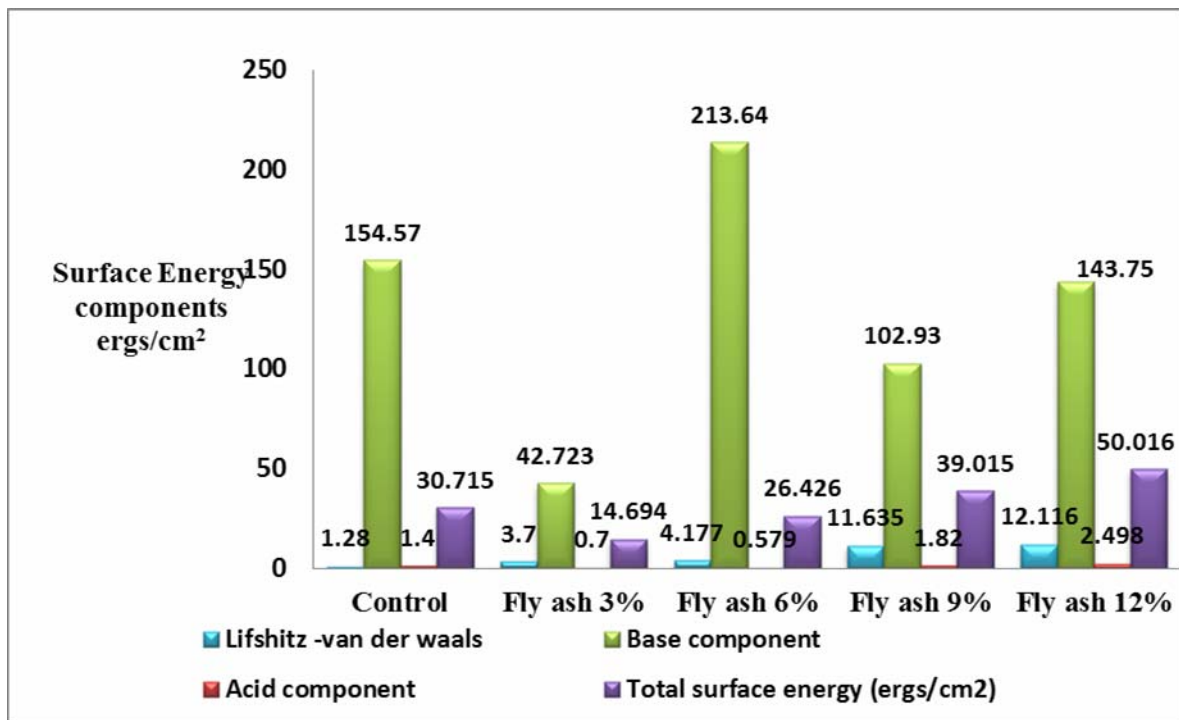


**Figure (8)** Effect of Fly ash on Surface Energy component of Asphalt binder by Wilhelmy Method

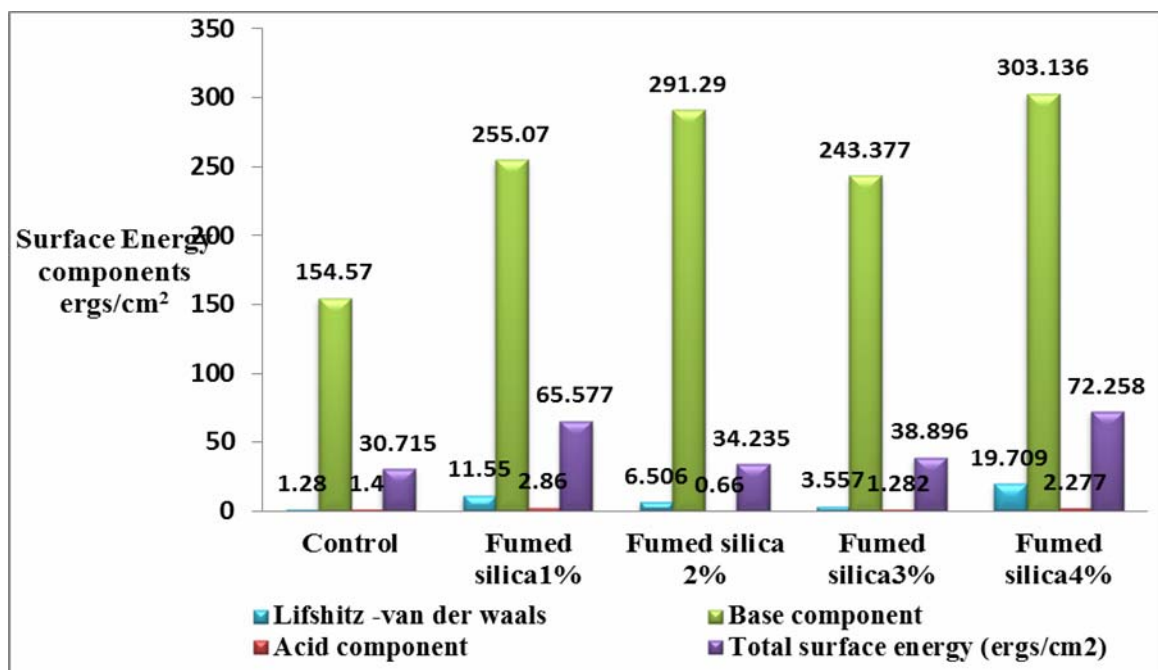


**Figure (9)** Effect of Fumed silica on Surface Energy components of Asphalt binder by Wilhelmy Method

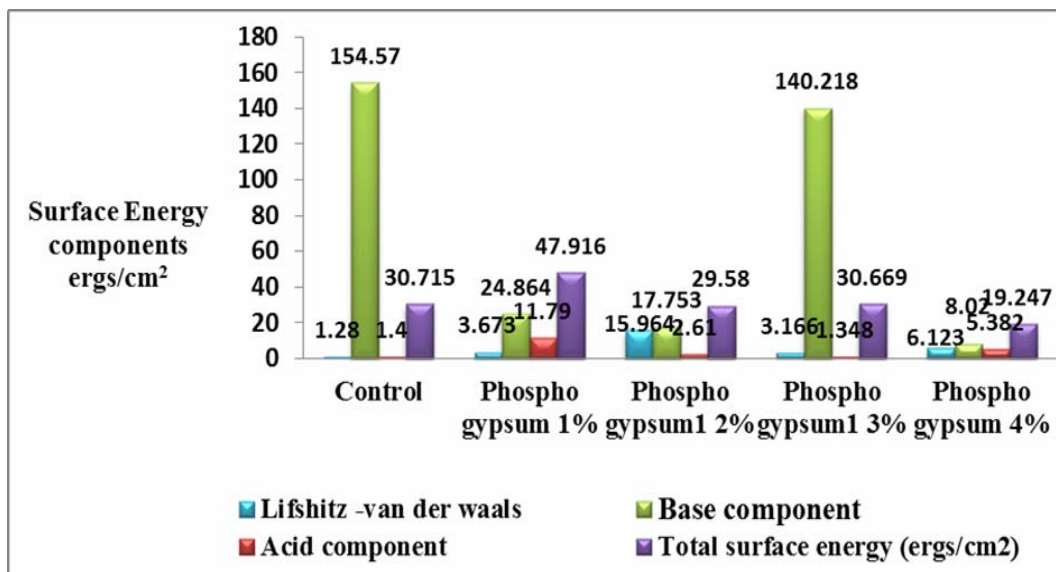
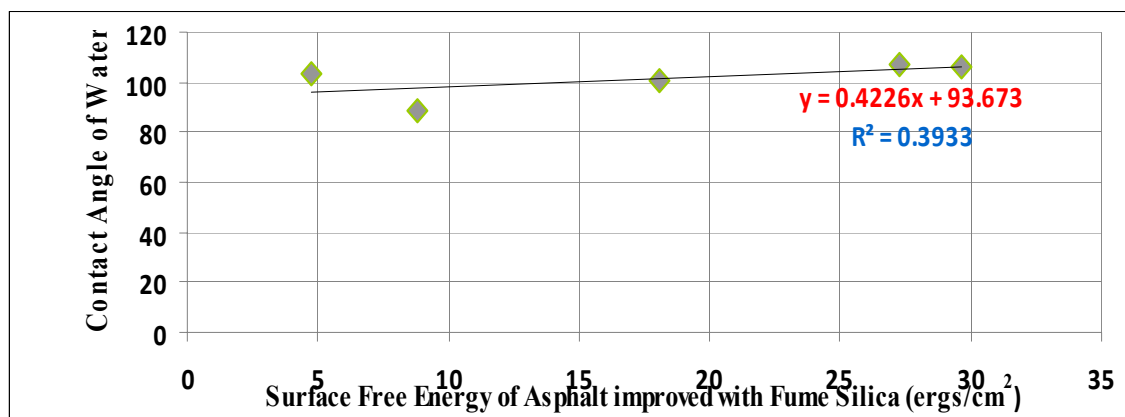


**Figure (10)** Effect of Phospho on Surface Energy components of Asphalt binder by Wilhelmy Method



**Finger (11)** Effect of fumed silica on contact angle

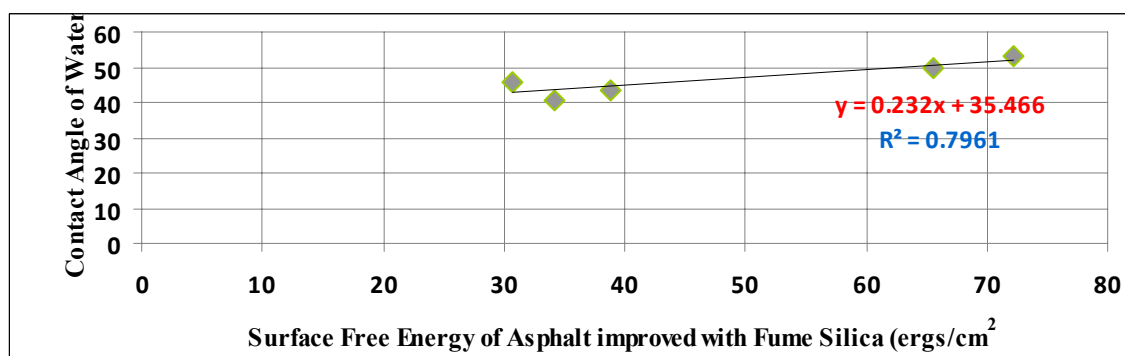


**Figure (12)** Effect of surface free energy on index of retained strength

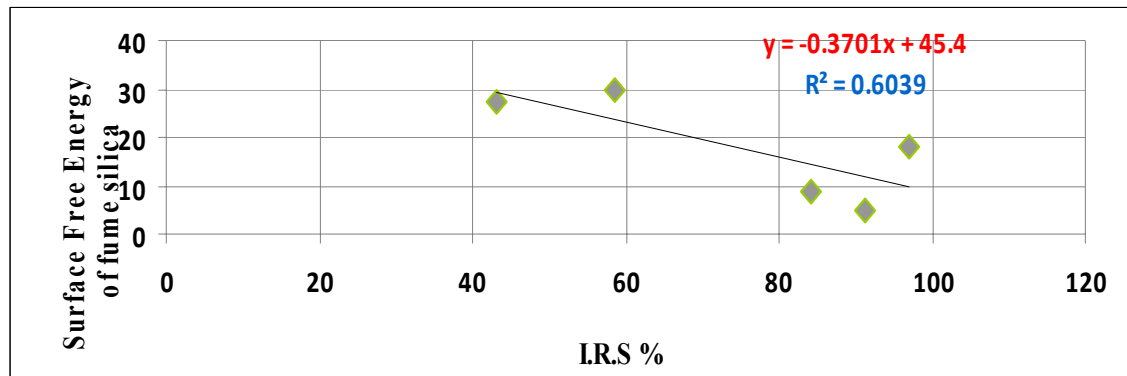


**Figure ( 13 )** Surface Free Energy and I.R.S. % Relationship Using Sessile Drop Method

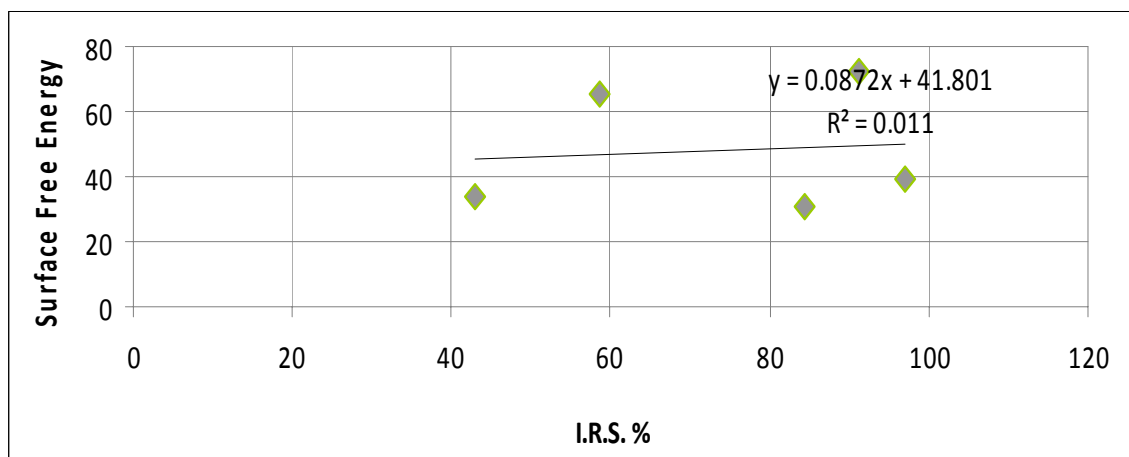


**Figure ( 14 )** Surface Free Energy and I.R.S. % Relationship Using Wilhelmy Method

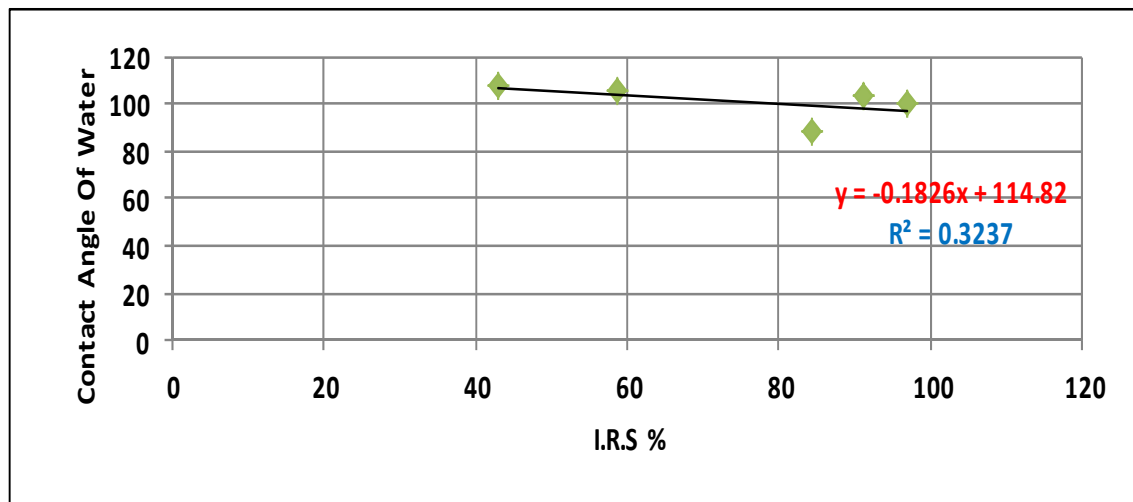


Figure ( 15) Contact Angle and I.R.S. % Relationship Using Sessile Drop Method

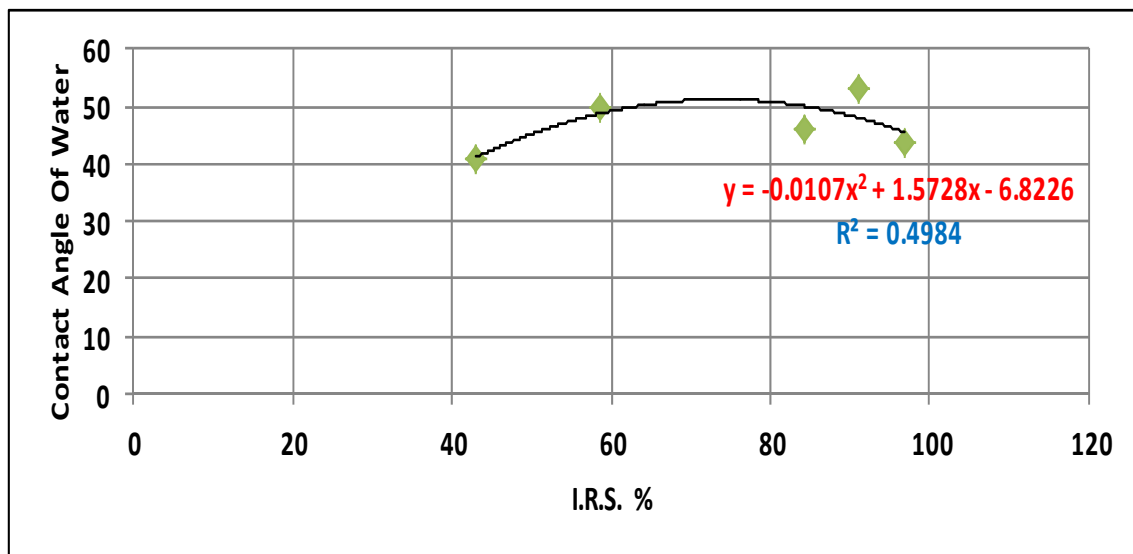


Figure (16) Contact Angle and I.R.S. % Relationship Using Wilhelmy Method



### Modeling of Stripping Potential Using Surface Energy (Sessile Drop)

Linear regression is used to develop model for stripping (I.R.S. %), physical and rheological properties using SSPS statistics 17.0.

The dependent variable is % Index of Retained Stability (%I.R.S).

The independent variables are SFESD, S.P, P, PVN, P. I,  $\theta_w$ ,  $\theta_F$ ,  $\theta_G$ , SM.

SFESD: Total surface free energy by sessile drop (ergs/cm<sup>2</sup>).

P.I= penetration Index.

S.P =Softening point of asphalt cement (°C).

P=Penetration of asphalt cement.

$\theta_w$  =Average contact angle when using water as probe liquid(°).

$\theta_F$ =Average contact angle when using Formamid as probe liquid(°).

$\theta_G$ =Average contact angle when using Glycerol as probe liquid(°).

SM=stiffness modules of asphalt cement and modified asphalt (N/m<sup>2</sup>).

It has been found that this model has an R<sup>2</sup> value of 0.871 and R of 0.933and the standard error of the estimated value of (42.70). The developed statistical model using SPSS software V. 17 is shown below in Eq.(19)

$$Y = -109816.12 + 2.4 \text{SFESD} + 217.2 \text{S.P} - 55.48 \text{P} - 941.89 \text{P.I} - 3.484 \theta_w + 1.271 \theta_F - 1.865 \theta_G + 8.28 \times 10^{-5} \text{SM} \quad (19)$$

### Modeling of Stripping Potential Using Surface Energy (Wilhelmy Method)

The following variables will be included in the prediction of the model:

The dependent variable is % Index of Retained Stability (%I.R.S).

The independent variables are SFEW, S.P, P, PVN, P. I,  $\theta_w$ ,  $\theta_F$ ,  $\theta_G$ , SM.

SFEW: Total surface free energy by Wilhelmy Method (ergs/cm<sup>2</sup>).

P.I= penetration Index.

S.P =Softening point of asphalt cement (°C).

P=Penetration of asphalt cement.

$\theta_w$  =Average contact angle when using water as probe liquid(°).

$\theta_F$ =Average contact angle when using Formamid as probe liquid(°).

$\theta_G$ =Average contact angle when using Glycerol as probe liquid(°).

SM=stiffness modules of asphalt cement and modified asphalt (N/m<sup>2</sup>).

It has been found that this model has an R<sup>2</sup> value of 0.827 and R of 0.909 and the standard error of the estimated value of (49.58).The developed statistical model is shown below in Eq.(20).

$$Y = -81267.65 - 2.16 \text{SFEW} + 45.3 \text{S.P} - 67.5 \text{P} -$$

$$109.44 \text{P.I} + 1.9 \theta_w - 4.778 \theta_F + 3.96 \theta_G$$

$$+ 1.18 \times 10^{-7} \text{SM} \quad (20)$$

It can be noticed that the following variables have the most positive effect on (I.R.S) % for both methods of surface energy. Table (3) shows the significance of such variables in descending order for Sessile drop and Wilhelmy Method.

**Table (4.21)** The Significant of such variables in descending order for both Method

Variable	Constant of (SDM)	Variable	Constant of (WPD)
<b>P.I</b>	941.89	P.I	109.44
<b>S.P</b>	217.20	P	67. 50
<b>P</b>	55.48	S.P	45.30
<b><math>\theta_w</math></b>	3.48	<b><math>\theta_F</math></b>	4.77
<b>SFE</b>	2.47	<b><math>\theta_G</math></b>	3.96
<b><math>\theta_G</math></b>	1.86	SFE	2.16
<b><math>\theta_F</math></b>	1.27	<b><math>\theta_w</math></b>	1.90
<b>SM</b>	$8.28 \times 10^{-7}$	SM	$1.11 \times 10^{-7}$

When using Sessile drop method the effect of surface free energy is significant as supported by high constant value of (2.47), while when using

Wilhelmy technique the effect of surface free energy is less significant due to a lower constant value (2.16).

## Conclusions

Based on the limitation of materials and test procedure in this work the following conclusions are drawn:

1. When using Sessile drop method the value of surface free energy of asphalt cement grade (40-50) was about  $8.8 \text{ ergs/cm}^2$ , while when using Wilhelmy technique the value of surface free energy of asphalt cement was  $30.71 \text{ ergs/cm}^2$ .
2. The surface free energy values as calculated by Sessile drop method are higher than the values calculated by using Wilhelmy technique for both asphalt cement and modified asphalt when using fly ash. While the surface free energy values calculated by using Wilhelmy method are greater than those values calculated by using sessile drop method for both asphalt cement and modified asphalt when using fumed silica and phospho gypsum.
3. Higher surface free energy values were obtained when using base component of Van Oss theory as compared to the acid

and Lifshitz -Van Der Waals for both methods.

4. Higher contact angle can be obtained when using sessile drop method and lower surface energy, while when using Wilhelmy technique we obtained lower contact angle and higher surface energy.
5. From the relationship between surface energy of the asphalt modified with fumed silica and the I.R.S. % when using sessile drop method it was found that the coefficient of determination ( $R^2$ ) was 0.6.
6. From the relationship between the contacts angle of the asphalt modified with fumed silica and the I.R.S. % when using Wilhelmy technique it was found that the coefficient of determination ( $R^2$ ) was 0.5.
7. The surface free energy concept should be considered when the stripping of asphalt concrete is under question.

## LIST OF ABBREVIATION

I.R.S %: The index of retained stability.

SDM : Sessile Drop Method.

SFE: Surface Free Energy.

WPM: Wilhelmy Plate Method.

## REFERENCE

- Arabani, M. and Hamed, Gh.(2010). "Using the Surface Free Energy Method to Evaluate the Effects of Polymeric Aggregate Treatment on Moisture Damage in Hot Mix Asphalt" (ASCE), volume No.23, pp. (802-811).

- Bhasin, A.; Little, D., Vasconcelos, K. and Masad, E. (2007). **“Surface Free Energy to Identify Moisture Sensitivity of Materials for Asphalt Mixes”**, (TRB), volume 2001, pp. (37-45).
- Cheng, D.; Little, D.; Lytton, R.; and Holste, J. (2002) **“ Surface Free Energy Measurement of Aggregates and Its Application to Adhesion and Moisture Damage of Asphalt aggregate Systems”** AAPT, Vol.71, pp.( 59-88).
- Little, D. and Bhasin, A. (2006). **“Using Surface Energy Measurements to Select Materials for Asphalt Pavement”**, Final Report for National Cooperative Highway Research program NCHRP Project 9-37(W104).
- State Commission of Roads and Bridge (SCRB) (2003): **“ Hot Mix Asphalt Concrete Pavement”**, Iraq Standard Specification, Ministry of Housing and Construction, Department of Design and Study ,Section R9.
- Shah, B. (2003). **“Evaluation of Moisture Damage within Asphalt Concrete Mixes”**, M.Sc Thesis, Texas A&M University.
- Wasiuddin, N. (2007). **“Effect of Additives on Surface Free Energy Characteristics of Aggregates and Binders in Hot Mix Asphalt”**, the Texas Transportation Institute (TTI).
- Yousif, S., (2003), **“Improving Bituminous Material Properties to Reduce the Effect of Stripping”** M.Sc thesis, University of Technology/Baghdad.
- Zhou, L.; Chen, F.; Jiang, Y.; and Qi Xie.(2009).**“ Influence of Water Saturated State on Moisture Susceptibility of Asphalt Mixture”** ,ASCE Performance Modeling and Evaluation of Pavement Systems and Materials (GSP 195) Proceedings of Selected Papers from the 2009, No.354,issue No.16.



## Multiwavelet based-approach to detect shared congestion in computer networks

Ass. Prof. Dr. Tarik Zeyad Ismaeel  
University of Baghdad  
Electrical Engineering Department

Eng. Ahmed A. Mahdi A. Kareem  
University of Baghdad  
Electrical Engineering Department

### Abstract

Internet paths sharing the same congested link can be identified using several shared congestion detection techniques. The new detection technique which is proposed in this paper depends on the previous novel technique (delay correlation with wavelet denoising (DCW) with new denoising method called Discrete Multiwavelet Transform (DMWT) as signal denoising to separate between queuing delay caused by network congestion and delay caused by various other delay variations. The new detection technique provides faster convergence (3 to 5 seconds less than previous novel technique) while using fewer probe packets approximately half numbers than the previous novel technique, so it will reduce the overload on the network caused by probe packets. Thus, new detection technique will improve the overall performance of computer network.

**Keywords:** congestion, computer network, shared congestion, DMWT, DWT.

### Introduction

Congestion in computer networks is becoming an important issue due to the increasing mismatch in link speeds caused by Intermixing between old and new technology of computer networks (CHIU, 1989). Flow control, congestion control and congestion avoidance are algorithms that have been addressed by several researchers in the past which are used to process congestion phenomena in computer network (Ramakrishnan, 1990). Generally speaking, there are two types of congestion that may occur in the computer network: first, *Independent congestion* may occur in the terminal of the network caused by one source which sends data through the links associated with it exceeds the capacity of these links or caused by two sources send data exceeds the capacity of individual link which is connect between them (Fall, 2009, Kim, 2003). The second type is *shared congestions* which occurs when two or more

flows sharing the same link in the network and these flows send data exceeds the capacity of shared link (Balakrishnan, 1999, Rubenstein, 2000). All algorithms used to manage the performance of computer networks will first need algorithms to detect the level of congestion in these networks, thus detecting congestion became very important issue in the field of computer network. Better utilization of network resources is achievable with cooperation between flows. For example, the Congestion Manager examines all flows of the host where it resides, and groups flows passing through the same bottleneck link into a single flow aggregate. By performing congestion control over flow aggregates, rather than over each individual flow separately, the Congestion Manager can improve fairness and efficiency significantly (CHIU, 1989, Kim, 2003).

Ass. Prof. Dr. Tarik Zeyad Ismaeel  
Eng. Ahmed A. Mahdi A. Kareem

The basic primitive required for cooperative congestion control is to decide whether two flows are sharing a bottleneck link or not. Techniques for inferring shared congestion use two kinds of information from feedback: packet loss and delay. Techniques based on packet loss assume bursty packet loss (Rubenstein, 2000), thus they work well with drop-tail queues and lossy links but it slow and inaccurate with low loss rate or with other queueing disciplines, such as RED. Techniques based on delay (Rubenstein, 2000, Katabi, 2001) show more robust behavior in such an environment.

This paper will propose previous novel technique (delay correlation with wavelet denoising or DCW) with new denoising technique (discrete multiwavelet transform or DMWT) to detect shared congestion between two computer network paths. Like previous techniques, it is based on a simple observation: two paths sharing congested links (as shown in figure 1) have high correlation between their one-way delays. However, naive correlation measurements may be inaccurate, due to random fluctuation of queuing delay and mild congestion on non-shared links. In new proposed technique, these interfering delay variations are filtered out with *multiwavelet denoising*, which is signal processing method to separate signal caused by shared congestion delay from other delay signals (noise).

New detection technique is evaluated through extensive simulation by using the following programming languages: network simulation ver.2 (NS2) (Fall, 2010), AWK ver.2 (Close, 1995), MATLAB ver. R2008b. It takes at most 5 s to detect shared congestion with both drop-tail and RED queues, while previous techniques often takes longer time or fail.

## Multiwavelet based-approach to detect shared Congestion in computer networks

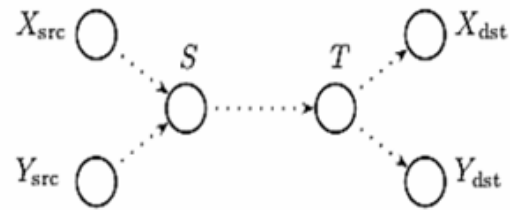


Fig. 1 Two paths sharing same link

## Metrics Used To Detect Shared Congestion

There are two important metrics used with most techniques to detect shared congestion in computer network.

- **One-way delay time:**  
Time needed to send each packet from source to destination (Wen, 2008).
- **One-way Packet Loss:**  
Represents the number of packets lost from overall packets sent from source to destination (Wen, 2008).

## Related Work

Rubenstein *et. al* (2000) (Rubenstein, 2000). Proposed two techniques to detect shared congestion in computer network, one based on one-way delays and the other is based on packet losses. The delay-based technique uses to generate a sequence of delay samples. An auto-measure Ma (auto correlation coefficients) is computed from pairs of adjacent packets of the first sequence. A cross measure Mx (cross correlation coefficients) is computed from a new delay sequence obtained by merging the two delay sequences. If  $Ma < Mx$ , it is mean that there is shared congestion. In their loss-based technique, Ma and Mx are conditional probabilities that a packet is lost when its following packet is lost.

Harfoush *et. al* (2001) (Harfoush, 2000). Harfoush technique explores the effects of concurrency on diagnosing network conditions. In this technique, a common source sends a packet pair back to back at 15 Hz. The probability that only the second packet is lost is computed from packet losses. If the probability exceeds the threshold (0.4), two paths are sharing a bottleneck.

Katabi *et. al* (2002) (Katabi, 2001). The approach of this technique relies on the observation that the correct clustering minimizes the entropy (Entropy: The concept of entropy is used as a measure of the uncertainty in a random variable) of the inter-packet spacing seen by the observer. This technique is highly accurate for detecting shared bottlenecks when the observer is strategically located, otherwise it becomes inaccurate.

Min S. Kim *et. al* (2003) (Kim, 2003). Proposed a novel technique (delay correlation with wavelet denoising or DCW) to detect shared congestion in Internet paths. Like previous techniques, it is based on a simple observation: two paths sharing congested links have high correlation between their one-way delays. If the correlation converges to 1, this means that there is shared congestion and other wise there is no shared congestion.

O. Younis and S. Fahmy (2005) (Fahmy, 2005). This technique is called Flowmate which uses the comparison test for delay based techniques from Rubenstein. At their development status they got the data from TCP (Transmission Control Protocol) flows only, since the majority of Internet traffic is TCP. The accuracy of bottleneck detection strongly depends on the lifetime of the TCP connections. The longer the lifetime of a connection the better the detection results are.

## Simulation Procedure

Block diagram shown in figure (2) is represents the procedures of new shared congestion detection technique.

## Delay Sampling Stage

Represents the first stage which will be used to get delay samples signal for path 1 and 2 for two types of queue (RED and DropTail). This stage is implemented on network topology shown in figure (3) which is created by NS2 program with the following parameters (Kim, 2003):

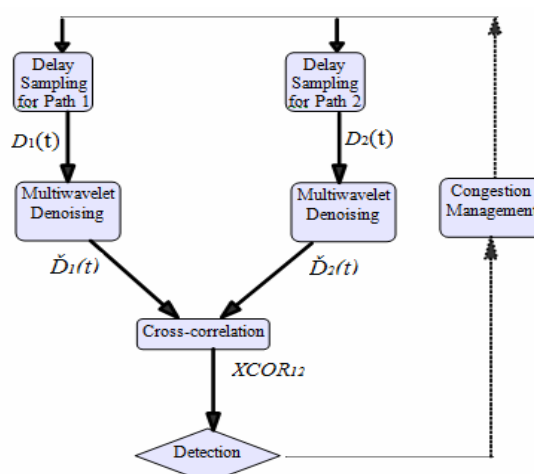


Fig. 2 Shared congestion detection

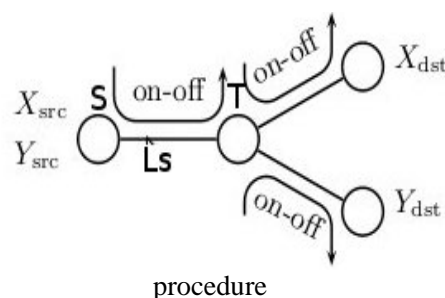


Fig. 3 Simple topology with a common source



(1) Each link has a bandwidth of 1.5 Mb/s. This value is chosen depending on real network measurements (Kim, 2003).

(2) The propagation delay of each link was chosen randomly between 20 and 30 ms for each simulation to make the behavior of simulation links similar to the behavior of real network links.

(3) Pareto ON-OFF constant-bit-rate (CBR) flows were used as background traffic, so that the congestion level could be controlled easily by changing the number of CBR flows. Background traffic will make some load on the simulation network links to make it near from the real network (Kim, 2003, Singh, 2004). The average ON and OFF states (ON-time is the time interval of sending packets by background traffic and OFF-time is the time interval of stopped (idle) sending packets) where selected uniformly between 0.2 and 3s. This step makes the behavior of simulation network near from the behavior of real network to increase the reliability of simulation results.

(4) The CBR rate was selected uniformly between 20 and 40 kb/s, and its pareto shape parameter was 1.2.

(5) Put 100 ON-OFF CBR flows on the shared link and 60 ON-OFF CBR on the independent links. With 60 flows, no congestion occurred and no packet loss was observed but the congestion will occur with 100 flows as well as the loss rate will be varied between 2% and 12%.

(6) The source node have two sources Xscr and Yscr which sends CBR packets through shared link to destination nodes Xdst and Ydst respectively at constant rate 10Hz (10 packets/S) in all simulations.

(7) The size of probe packet is 500 kB. (kB = kByte)

(8) The queueing size at each node is 50 packets.

(9) Background flows will start sending data

at time 0 and after 1 second the sources Xscr and Yscr will start sending probe packets to ensure that the links are not empty.

(10) The time of each simulation starts from 0 to 105 s.

### DMWT Denoising Stage

The block diagram shown in figure (4) shows the procedure of denoising stage by DMWT.

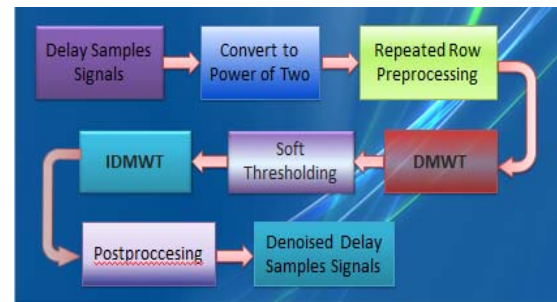


Fig. 4 Procedure of DMWT denoising stage

The important sub stages in the DMWT denoising stage is: DMWT, soft thresholding and IDMWT (inverse of DMWT). The other sub stages are assistant stages.

### DMWT Operation

DMWT sub stage will analyze the input signal to two types of coefficients, the first one is approximation coefficients (represent the main information about original signal) which can be obtained by the following equation (Strela, 1998):

$$v_{j,k} = \sum_m G_{m-2k} v_{j-1,m} \quad (1)$$

Where

$v_{j,k}$  = approximation coefficients

$G_{m-2k}$  = low pass filter of DMWT

$v_{j-1,m}$  = samples of input signal

The second one is detail coefficients (represent noise components) which can be obtained it by the following equation (Strela, 1998):

$$w_{j,k} = \sum_m H_{m-2k} v_{j-1,m} \quad (2)$$

Where

$w_{j,k}$  = detail coefficients

$H_{m-2k}$  = high pass filter of DMWT

### Soft Thresholding Operation

This sub stage is very important because it is used to remove noise from analyzed signal to get original signal. To get denoised signal, soft thresholding algorithm should be applied on the detail coefficients only for each decomposition level. Threshold value  $T$  is needed to apply thresholding algorithm. The idea of universal thresholding for scalar sequence of white noise wavelet coefficients with mean zero and variance  $\sigma^2$  as in equation (3) (Strela, 1998).

$$T = \sigma \sqrt{2 \log_e N} \quad (3)$$

where  $N$  is the length of original input signal and  $\sigma$  represents the variance of input signal.

The universal threshold is attractively simple, but it is strictly suitable only when thresholding a gaussian scalar sequence of white noise wavelet (detail) coefficients of mean zero and variance  $\sigma^2$ . The repeated row preprocessing and the DMWT will change substantially the variances of the wavelet coefficients  $w_{j,k}^{(0)}$  and  $w_{j,k}^{(1)}$ , thus 'average variances' have been defined ; for example, GHM filter banks with repeated row preprocessing the noise variance  $\sigma^2$  is deflated by a factor  $c = 0.75$  to  $0.75 \sigma^2$ . Hence, for GHM with repeated row preprocessing,  $\tilde{N} = 2N$ ,  $T$  will be calculated

by the following equation (Strela, 1998):

$$T = \sqrt{2 * 0.75 \sigma_e^2 \log (2N)} \quad (4)$$

### IDMWT Operation

This sub stage will use approximation coefficients and denoised detail coefficients to create denoised delay samples signal for path 1 and 2 by the following equation (Strela, 1998):

$$v_{j-1,k} = \sum_m \tilde{G}_{k-2m}^T v_{j,m} + \sum_m \tilde{H}_{k-2m}^T w_{j,m} \quad (5)$$

Where

$v_{j-1,k}$  = approximation and denoised detail coefficients for  $j-1$  of decomposition level. If  $j=1$  then  $v_{j-1,k}$  will represent denoised delay samples signal.

### Cross-Correlation Stage

In signal processing, cross-correlation is a measure of similarity of two waveforms as a function of a time-lag (Wikipedia, 2010). The general shared congestion detection technique is based on the observation that measured delays of two paths showing strong correlation if the paths share one or more congested links, and little correlation if they don't share any congested links. Cross-correlation coefficients are calculated between delay samples signal for path 1 and 2 by the following equation (Rubenstein, 2000):

$$XCOR_{XY} = \frac{\sum_{i=1}^n (X_i - \bar{X})(Y_i - \bar{Y})}{\sqrt{\sum_{i=1}^n (X_i - \bar{X})^2 \sum_{i=1}^n (Y_i - \bar{Y})^2}} \quad (6)$$

Where

$X_i$  and  $Y_i$  are represent one way delay signals for path X and path Y.



Ass. Prof. Dr. Tarik Zeyad Ismaeel  
Eng. Ahmed A. Mahdi A. Kareem

$\bar{X}$  and  $\bar{Y}$  represent the average of one way delay signals for path X and path Y.

### Detection Stage

This stage depends on the value of cross-correlation coefficients obtained from cross-correlation stage to decide whether shared congestion occurred or not in the tested path. If the values of cross-correlation coefficients converge to {1}, this leads that shared congestion occurred in the tested path of computer network, while if the cross-correlation coefficients converge to {0}, this leads that there is no shared congestion in the tested path of computer network.

### Limitation

The important limitation for the new detection technique is *synchronization offset* which is defined as the time difference between arrivals of two probe packets at  $S$  (see figure 3), one sent by  $X_{src}$  at time  $t$  with  $X_{src}$ 's clock and the other by  $Y_{src}$  at time  $t$  with  $Y_{src}$ 's clock. As shown in figure (5), when synchronization offset increases, the delay sequences collected by the two nodes show less and less correlation. Figure (5) plots the cross-correlation coefficients without using any denoising signal techniques for two paths sharing a congested link as synchronization offset rises from 0 to 1s (Kim, 2003).

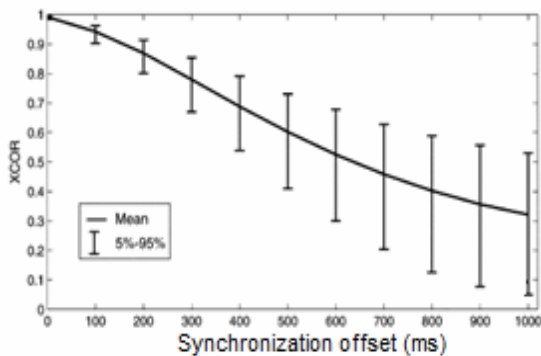


Fig. 5 Cross-correlation coefficient between two delay sequences versus synchronization

## Multiwavelet based-approach to detect shared Congestion in computer networks

### Simulation Results

After implementing the steps in delay sampling stage with RED queue technique and the source codes were co-located and their clocks were synchronized, the following signals will be obtained as shown figures (6) and (7) which represent the one way delay samples D1 and D2 of two sources  $X_{src}$  and  $Y_{src}$  sharing the same bottleneck  $L_s$  as shown in figure (3) for 100 seconds simulation. Each sample in the two delay signals represents the average of 500 simulations as explained in delay sampling stage to make the new detection technique is similar to the real network behavior.

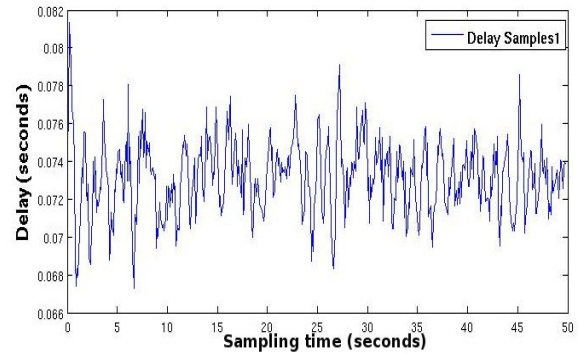


Fig. 6 Delay samples signal for path 1

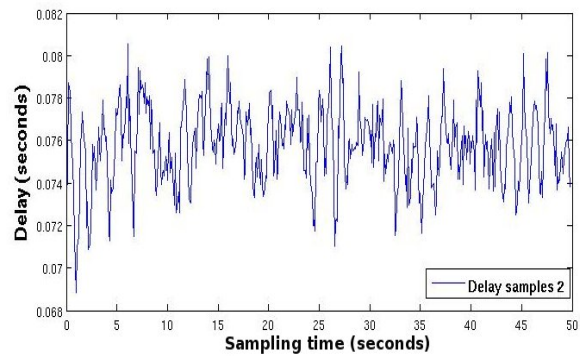
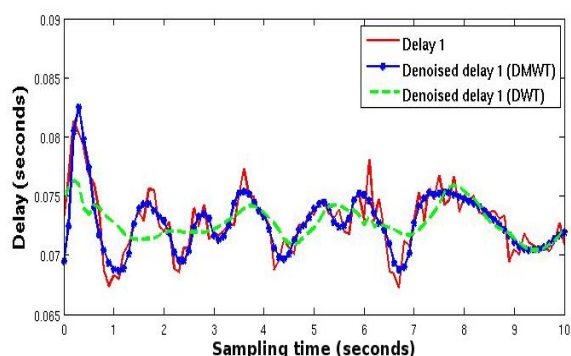


Fig. 7 Delay samples signal for path 2

To show if there is a shared congestion in the link  $L_s$  or not, these two signals D1 and D2 will be denoised by discrete multiwavelet denoising technique to get denoised signals  $\tilde{D}1$  and  $\tilde{D}2$  then calculating series of cross-correlation

coefficients by using these two denoised signals. If cross-correlation coefficients converge to one, this indicates that there is a shared congestion and if cross-correlation coefficients converge to zero, this indicates that there is no shared congestion.

Figures (8) and (9) show the denoised of delay samples signals for path 1 and path 2 which are obtained from DWT and DMWT for three levels of decomposition. From these two figures, it can be shown that the power dropped from denoised signal by DMWT (star curve) is smaller than the one from signal denoised by DWT (dotted curve). This property is useful to keep fluctuations larger than noise in delay samples similar or near from fluctuations in original signal.



**Fig. 8** Part of denoised delay 1 by DWT and DMWT

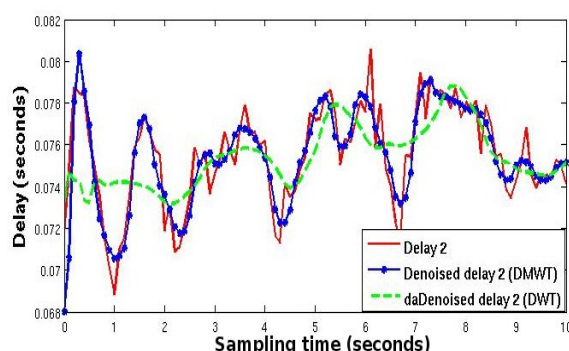


**Fig. 9** Part of denoised delay 2 by DWT and DMWT

There is small difference between delay samples 1 and delay samples 2 caused by the behavior of RED queue technique which is used by network devices (router, switch, etc). DMWT will decrease the effect of this difference on the new detection technique by removing noise from these two delay signals and increase the similarity between them better than DWT does. Cross-correlation technique is used to calculate the similarity between the two collected signal, thus, DMWT will detect shared congestion faster than DWT because DMWT increases the similarity between the two collected signal and makes cross-correlation coefficients converge to one faster than coefficients obtained from DWT with small number of collected samples.

Figure (10) shows the mean of cross-correlation coefficients over 500 experiments with sending rate of 10Hz and three level of decomposition for delay samples which denoised by DWT and DMWT.

Figure (10) shows that the cross-correlation coefficients calculated from two delay samples which denoised by DMWT (continuous curve) is better and faster to converge to 1 than the cross-correlation coefficients calculated from same delay samples which is denoised by DWT (dotted curve).

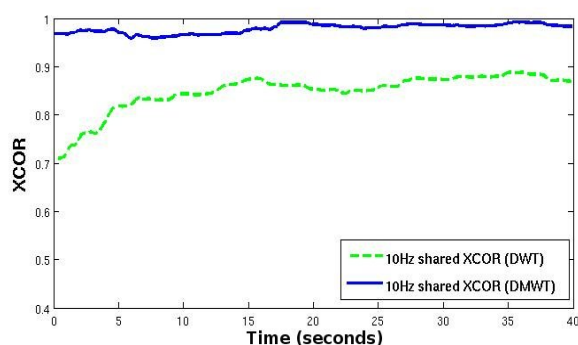


**Fig. 10** Shared cross-correlation coefficients with RED queue

**Ass. Prof. Dr. Tarik Zeyad Ismaeel**  
**Eng. Ahmed A. Mahdi A. Kareem**

This means that the new detection technique is faster from previous novel technique (DCW) and need less than 7 seconds to detect shared congestion and this will improve overall network management.

Now we will test the new detection technique if there is independent congestion in the tested path.

Figures (11) and (12) represent mean of independent congestion delay samples of 500 simulations.

It can be shown that the two delay samples signals in figures (11) and (12) are not similar especially in large fluctuation as shared congestion because delay samples that flow through independent link 1 (from node T to Xdst node in figure (3)) will be exposed to situations differs from delay samples flow through independent link 2 (from node T to Ydst node in figure (3)).

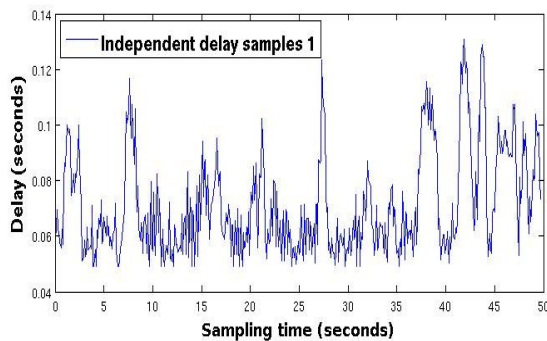


**Fig. 11** Mean of independent congestion delay samples for path 1

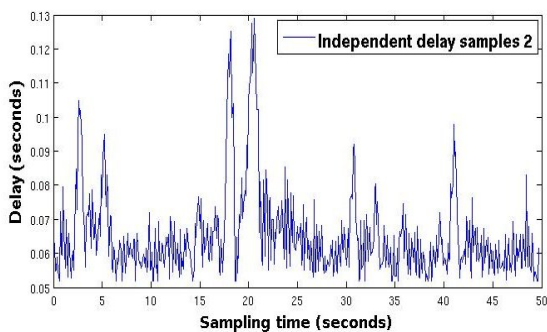


**Fig. 12** Mean of independent congestion delay samples for path 2

### **Multiwavelet based-approach to detect shared Congestion in computer networks**

Figure (13) shows cross-correlation coefficients between delay samples 1 and delay samples 2. Figure (13) shows that both cross-correlation coefficients obtained from denoising independent delay samples 1 and delay samples 2 by DWT and DMWT are reliable, similar and converge to zero after 3 seconds but cross-correlation coefficients obtained by DMWT are more stable from cross-correlation coefficients obtained by DWT.

The important factor which has a negative effect on the new detection technique and previous novel technique is synchronization offset which was explained in limitation section. When synchronization offset increases, the negative effect on both DWT and DMWT will be increased. Figure (14) shows the negative effects of increasing of synchronization offset on cross-correlation coefficients and make both new detection technique and previous novel technique less reliable.

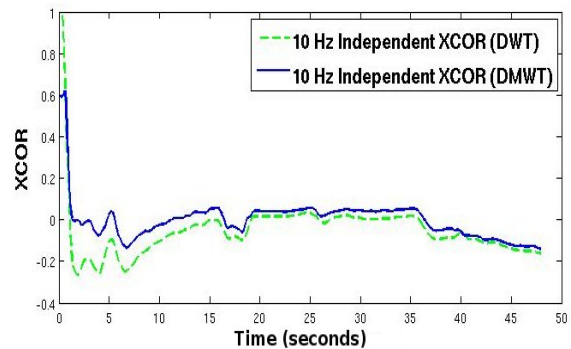


**Figure 13** Independent cross-correlation coefficients

Figure (14) shows the effect of synchronization offset on the cross-correlation coefficients calculated from delay sequences 1 and 2 and how denoising techniques improves the algorithm of detecting a shared congestion in computer network by decreasing the effect of synchronization offset. Red dotted curve represents the mean of cross-correlation coefficients for non denoised delay samples which shows fast decays with the increase of synchronization offset and with 500 ms

offset, the mean coefficient approaches to (0.5) which is the cut off values.

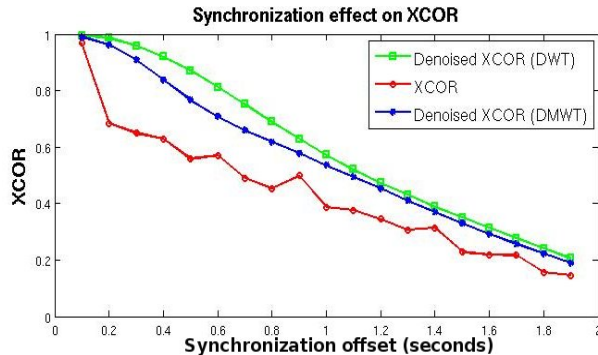


**Figure 14** The effects of DWT and DMWT On the synchronization offset

It can be shown, with denoised cross-correlation coefficients by DWT and DMWT, the technique became more reliable and robust with 1 second of synchronization offset. So the maximum offset is roughly the maximum round-trip time (RTT) on the computer network. Measurement studies including one done by CAIDA (CAIDA, 1999) confirm that round-trip time is less than 1 second for the majority of paths on the computer network.

From all previous results, It can be shown that DMWT improves the new detection technique and make it faster from previous novel technique (DCW) to detect shared congestion in computer networks.

## Conclusions

A new shared congestion detection technique based on the previous novel technique except DWT is replaced with DMWT which has more robust properties than wavelet transform in signal denoising and image compression. DMWT improve signal denoising technique in new detection technique and makes it faster (need less than 7 second) from previous novel technique (DCW) to detect shared congestion in computer network with approximately half number of probe packets which is needed with previous novel

technique. Thus, new detection technique will decrease the effect of overload on the network caused by probe packets.

## References

CAIDA, "The Cooperative Association for Internet Data Analysis", Source: CAIDA, skitter-f.isc.org, available at

<http://www.caida.org/tools/measurement/skitter/RSSAC/>, 8 October 1999.

D. B. Close, et al., "The AWK Manual", Free Software Foundation, Inc, Edition 1.0, December 1995.

D. CHIU, *et al.*, "Analysis of the Increase and Decrease Algorithms for Congestion Avoidance in Computer Networks", Digital equipment corporation, computer network and ISDN systems, Elsevier science publishers, 1989.

D. Katabi, et al., "A passive approach for detecting shared bottlenecks", In Proceedings of the 10th IEEE International Conference on Computer Communications and Networks, Oct. 2001.

D. Rubenstein, et al., "Detecting Shared Congestion of Flows Via End-to-end Measurement ", Working draft of version to appear in ACM SIGMETRICS'00, University of Massachusetts at Amherst, Department of Computer Science, June 2000.

H. Balakrishnan, et al., "An Integrated Congestion Management Architecture for Internet Hosts", technical report, M.I.T. Laboratory for Computer Science and IBM T. J. Watson Research Center, 1999.

H. C. Wen, et al., "method for detecting congestion in internet traffic", Technical report, United States Patent (San Jose, CA, US), 2008.

**Ass. Prof. Dr. Tarik Zeyad Ismaeel**  
**Eng. Ahmed A. Mahdi A. Kareem**

**Multiwavelet based-approach to detect shared  
Congestion in computer networks**

H. Tammerle, "Implementation and Evaluation of a Shared Bottleneck Detection System in Computer Networks", Master Thesis, University of Innsbruck, Institute of Computer Science, June 19, 2009.

K. Fall, et al., "The ns Manual", The VINT Project A Collaboration between researchers at UC Berkeley, LBL, USC/ISI, and Xerox PARC, 2010.

K. Harfoush, et al., "Robust Identification of Shared Losses Using End-to-End Unicast Probes", In Proceedings of the 8th IEEE International Conference on Network Protocols, Nov. 2000.

K. K. Ramakrishnan, et al., "A Binary Feedback Scheme for Congestion Avoidance in Computer Networks", ACM Transactions on Computer Systems, Vol. 8, No. 2, May 1990, Pages 158-181.

M. S. Kim, et al., "A Wavelet-Based Approach to Detect Shared Congestion", Technical Report, University of Texas at Austin, Electrical and Computer Engineering, 2003.

M. Singh, P. Pradhan, P. Francis, "MPAT: Aggregate TCP Congestion Management as a Building Block for Internet QoS", International conference, Cornell University, IBM T.J. Watson Research Center, 2004.

O. Younis and S. Fahmy, "FlowMate: Scalable On-line Flow Clustering", Networking, IEEE/ACM, University of Purdue, Department of Computer Science, 2005.

V. Strela, A. T. Walden, "Orthogonal and Biorthogonal Multiwavelets for Signal Denoising and Image Compression", Department of Mathematics, Dartmouth College, USA, 1998.

Wikipedia, "Cross-correlation", Available at <http://en.wikipedia.org/wiki/Cross-correlation#Properties>, September 2010.





## Experimental Investigation into the Heat and Mass Transfer in an Indirect Contact Closed Circuit Cooling Tower

Asst. Prof. Dr. Najim Abid Jassim <sup>a</sup>, Mohammed A. Al-Tayyar <sup>b</sup>

<sup>a</sup> Univ. of Baghdad, College of Eng., Mech. Dept., [najmosawe@yahoo.com](mailto:najmosawe@yahoo.com),

<sup>b</sup> M.Sc. Student, Univ. of Baghdad, College of Eng., Mech. Dept. [mohammed\\_tayyar@yahoo.com](mailto:mohammed_tayyar@yahoo.com)

### Abstract

The heat and mass transfer coefficients of the indirect contact closed circuit cooling tower, ICCCT, were investigated experimentally. Different experiments were conducted involving the controlling parameters such as air velocity, spray water to air mass flow rate ratio, spray water flow rate, ambient air wet bulb temperature and the provided heat load to investigate their effects on the performance of the ICCCT. Also the effect of using packing on the performance of the ICCCT was investigated. It was noticed that these parameters affect the tower performance and the use of packing materials is a good approach to enhance the performance for different operational conditions. Correlations for mass and heat transfer coefficients are presented. The results showed a good agreement with other published works. Correlations are showed that the spray heat transfer coefficient is a function flow rates of spray water and air as well as spray water temperature while mass transfer coefficient is a function of spray water and air flow rates only.

### Keywords

Closed Circuit Cooling Tower, Experiments, Heat & Mass Transfer Coefficients, Correlations

### التحقق العملي من انتقال الحرارة والكتلة في برج تبريد نوع مغلق و ذي اتصال غير مباشر

استاذ مساعد د. نجم عبد جاسم، محمد عبد الخالق الطيار

### الخلاصة

تضمن هذا البحث دراسة معاملي إنتقال الحرارة والكتلة لبرج تبريد من النوع المغلق ذي الإتصال غير المباشر عملياً. حيث تم إجراء عدد من التجارب بتغيير العوامل الحاكمة في أداء برج التبريد كسرعة الهواء، نسبة معدل التدفق الكتلي بين ماء الرش والهواء، معدل تدفق ماء الرش، درجة حرارة البصلة الرطبة للهواء الخارجي و الحمل الحراري المجهز من أجل تحري تأثيرات هذه العوامل على أداء البرج. كذلك فقد تم أيضاً تحري تأثير إستخدام الحشوات على الأداء الحراري للبرج. لقد بينت النتائج أن لهذه العوامل تأثيرات واضحة على أداء البرج وإن استخدام الحشوات طريقة جيدة لتحسين الأداء ولظروف تشغيلية مختلفة. تم تقديم معادلات تجريبية لمعاملي إنتقال الكتلة والحرارة وأظهرت هذه المعادلات توافقاً جيداً مع الأعمال المنشورة في الأدبيات. بينت المعادلات التجريبية أن معاملي إنتقال الحرارة يعتمد على معدل تدفق كل من ماء الرش والهواء إضافة إلى درجة حرارة ماء الرش في حين إن معاملي إنتقال الكتلة يعتمد على معدل تدفق ماء الرش والهواء فقط.

## Introduction

Cooling towers are heat exchangers which are used to dissipate large heat loads to the atmosphere. They are equipments used to reduce the temperature of a water stream by extracting heat from water and emitting it to the atmosphere. Heat is transferred in a cooling tower by two major mechanisms as sensible heat from water to air (convection) and latent heat transfer by the evaporation of water (diffusion). These mechanisms operate at the air-water interface. The total heat transfer is the sum of the effect of these mechanisms.

One considers an elementary control-volume as that shown in **Fig. 1**. This is crossed by a water flow, an air flow and a water spray flow. At the interface between the air and the water spray, there is a film of saturated air, in close contact with the water. This film of saturated air is at the average temperature of the water spray film in this small element of volume. Since the water-vapor partial-pressure at this interface is higher than the water-vapor partial pressure in the air, there is a transfer of water-vapor towards the air. This mass transfer brings a heat transfer related to the water vaporization, called transfer of latent heat. At the same time, because of the difference in temperature between surface of the water and the air, there is transfer of heat by convection (Stabat & Marchio 2004). Radiation effect is likely to be very small at normal conditions and it is generally neglected.

There are numerous types of cooling towers according to the conditions such as climate, place, capacity...etc. The indirect contact closed type cooling tower has been traditionally used in various industrial and HVAC systems. It contains two separate fluid circuits: (1) an external circuit, in which water is exposed to the atmosphere as it cascades over the tubes of a coil bundle, and (2) an internal circuit, in which the fluid to be cooled circulates inside the tubes of the coil bundle. In operation, heat flows from the internal fluid circuit, through the tube walls of the coil, to the external water circuit and then, by dual heat & mass transfer, to the atmospheric air.

The main advantageous of this type compared with an open cooling tower are the contamination risks with airborne dusts & corrosion

are limited since the process water never contacts the outside air, the possibility of using it to cool

Fluids other than water as the internal fluid never contacts the atmosphere and it minimizes contamination and maintenance of heat exchangers, chiller condensers and other equipments. The main drawback compared to an open cooling tower is that the cost & the size are increased since a large heat exchange is required to reach the same heat transfer.

The objective of this work is to investigate the thermal performance of the ICCCT experimentally. This was represented by the mass transfer coefficient between spray water interface and air,  $\alpha_m$ , and the heat transfer coefficient between tubes and spray water,  $\alpha_s$ .

## 1. Literature Review

The first basic theory of cooling tower was proposed by Walker in 1923. Several authors presented some correlations of mass transfer coefficient between air and spray water film and heat transfer coefficient between tube external surface and spray water film that take place in closed circuit cooling tower and evaporative cooler.

Parker & Treybal in 1961 were the first researchers presented a detailed analysis of counter flow evaporative liquid coolers. The analysis assumed that the amount of water evaporated is negligibly small. Empirical correlations for heat & mass transfer were presented for 19mm outside diameter staggered tubes as in equs. (1) & (2), respectively. They assumed that the Lewis factor is equal to unity.

$$\alpha_s = 704(1.39 + 0.022T_{sp}) \left(\frac{\Gamma}{D}\right)^{\frac{1}{3}} \quad (1)$$

$$\alpha_m = 0.049G_{air}^{0.049} \quad (2)$$

Mizushinha et al., in 1967, conducted tests on an evaporative cooler for three different tube diameters 12.7, 19.05 and 40 mm to predict the effect of tube diameter variation on heat & mass transfer coefficients. An assumption of constant spray water temperature inside the tower was applied. The results of mass transfer coefficient were presented as a function of air Reynolds



number ( $Re_{air}$ ) and spray water Reynolds number ( $Re_{sp}$ ) while heat transfer coefficient was presented as a function of spray water flow rate per unit length ( $\Gamma$ ):

$$\alpha_s = 2100 \left( \frac{\Gamma}{D} \right)^{\frac{1}{3}} \quad (3)$$

$$\alpha_m A_v = 5.028 * 10^{-8} Re_{air}^{0.9} Re_{sp}^{0.15} D^{-0.26} \quad (4)$$

where  $A_v$  is the contact area per unit volume and these correlations are valid for the ranges of  $1.5 * 10^3 < Re_{air} < 8 * 10^3$  and  $50 < Re_{sp} < 240$ .

Nistu et al. in 1969 suggested the heat and mass transfer correlations of an evaporative cooler having both smooth and finned tubes with 16 mm outside diameter in a staggered arrangement. The correlations for plain tubes were as shown below:

$$\alpha_s = 990 \left( \frac{\Gamma}{D} \right)^{0.46} \quad (5)$$

$$\alpha_m = 0.076 G_{air}^{0.8} \quad (6)$$

Hasan & Sirén in 2002 developed a computational model for a 10 kW nominal power CWCT with chilled ceilings consisted of 19 tubes of 10 mm outside diameter arranged in 12 rows in a staggered arrangement. They also presented a correlation for the mass transfer coefficient concluded for a total of 60 sets of measurements as shown in equ. (7).

$$\alpha_m = 0.065 \dot{G}_{air}^{0.778} \quad (7)$$

Oliveira & Facao in 2004 tested a small-size indirect contact cooling tower and correlations for heat & mass transfer were experimentally determined. Experimental results obtained heat transfer coefficient as a function of spray flow rate as shown in equ. (8), while mass transfer coefficients was presented as a function of air flow as shown in equ. (9). The model showed that the correlations have a good degree of accuracy when applied to all possible operating conditions.

$$\alpha_s = 602 \left( \frac{\Gamma}{D} \right)^{0.358} \quad (8)$$

$$\alpha_m = 0.064 \dot{G}_{air}^{0.81} \quad (9)$$

Gyu-Jin Shim et al. in 2008 investigated experimentally the effect of changing the heat exchanger in a CWCT on the heat & mass transfer coefficients and also on cooling capacity. Two heat exchangers consisting of bare-type copper tube of 15.88mm & 19.05mm were used with multi path. It was found that the range of CWCT using two paths is higher approximately 20% than those using one path.

Heyns & Kroger in 2010 investigated the thermal-flow performance characteristics of an evaporative cooler consisting of 15 tube rows with 38.1 mm outer diameter galvanized steel tubes. From the experimental results, correlations for the water film heat transfer coefficient, air–water mass transfer coefficient were developed. Their results showed that the spray water mass flow rate has the greatest influence on the spray heat transfer coefficient but this coefficient is also a function of the air mass flow rate and the spray water temperature as given by equ. (10). It was also found that the air–water mass transfer coefficient is a function of the air mass velocity and the spray water mass velocity as given by equ. (11).

$$\alpha_s = 470 \dot{G}_{air}^{0.1} \left( \frac{\Gamma}{D} \right)^{0.1} T_{sp}^{0.8} \quad (10)$$

$$\alpha_m = 0.038 \dot{G}_{air}^{0.778} \left( \frac{\Gamma}{D} \right)^{0.2} \quad (11)$$

Yoo et al. in 2010 analyzed the performance of the heat exchanger for the CWCT. Two heat exchangers in inline arrangement were investigated: a 22 row by 11 column with diameter of 9.52 mm (heat exchanger 1) and an 8 row by 5 column with diameter of 25.4 mm (heat exchanger 2). They indicated that the heat transfer coefficient can be obtained from the equation for external heat transfer of tube banks and the mass transfer coefficient was affected by the air velocity and spray water flow rate. This study provides the correlation equation for mass transfer coefficient based on the analogy of the heat and mass transfer and the experimental data. The result from the correlation equation showed accuracy within 5% with the experimental data.



The objects of this study is to analyze the influence of inlet cooling water temperature, inlet air wet and dry bulb temperatures, spray water and air flow rates and heat load on the thermal performance of the indirect contact closed circuit cooling tower. The mass transfer coefficient calculated from heat and mass transfer analogy was compared with experimental data. The regulated correlation was obtained from the result of the comparison. The cooling capacity and thermal efficiency of the closed wet cooling tower were calculated from provided equation and the performance of the tower were investigated.

## 2. Experimental Apparatus And Method

The system that used in the experimental tests is a (WL 320 Demo cooling tower, made by Gunt company in Germany). It was an open circuit direct contact counter flow forced draft cooling tower. This cooling tower was modulated to be used as an indirect contact closed type cooling tower by adding several components such as a bare-tube heat exchanger & the cooling water circuit. The heat exchanger was designed and then manufactured according to the procedure that presented by (Kern in 1978). It was consisted of 8 mm outside copper tube diameter with 6 rows and 12 columns in an inline arrangement. The experimental apparatus consists generally of the cooling column, cooling water circuit, spray water circuit & the air circuit. A schematic diagram & a photograph of the experimental apparatus are shown in **Figs. 2 & 3**, respectively.

The cooling column is the most important portion in the experimental apparatus where the cooling process takes place inside it. It is a duct made from transparent glass with (150\*150\*800 mm) to allow the spray water paths inside it to be observed.

Cooling water circuit transfers the water that to be cooled through the tower inside the heat exchanger. After it reheated, the cooling water is recirculated through this circuit to cool again. This circuit consists of tank with a heater to reheat the cooling water, pump and the heat exchanger.

Spray water circuit transfers the spray water through the tower to enable the tower from operating in wet mode operation. This circuit consists of tank, pump and spray nozzle.

By the air circuit the air is brought into the cooling tower and it is then blow through the

cooling column to absorb heat from the other process fluids. This circuit consists of a blower to blow the air and humidifier and dehumidifier to adjust the conditions of the supplied air such as relative humidity, dry and wet bulb air temperatures.

Measuring devices were used to sense the variations of cooling water temperatures & flow rate, spray water temperatures, flow rate, air temperatures, relative humidity, air velocity, flow rate and electrical voltage and current.

Several experiments were conducted by changing the controlling parameters involving air velocity, spray water to air mass flow rate ratio, spray water flow rate, ambient air wet bulb temperature and the provided heat load to investigate their effects on the performance of the ICCCT. In addition to this, each experiment was repeated twice changing the above parameters, first without using packing and then packing were fixed inside the cooling column above the heat exchanger to study the effect of packing on the tower transfer coefficients.

After all the experimental data for each experiment were collected and recorded, a set of calculations was started to obtain the experimental mass and heat transfer coefficients for the ICCCT.

The mass transfer coefficient of water vapor between spray water film and air was calculated after experimental measurements using eq. (12) which was presented by Olivera & Facao 2004:

$$G(h_{air,out} - h_{air,in}) = \alpha_m A LMhD \quad (12)$$

where,  $\alpha_m$  is the mass transfer coefficient ( $\text{kg/m}^2 \text{ s}$ ),  $A$  is the surface area of the heat exchanger equal to  $0.226 \text{ m}^2$ , and  $LMhD$  is the logarithmic mean enthalpy difference ( $\text{kJ/kg}$ ) defined as:

$$LMhD = \frac{h_{air,outi} - h_{air,in}}{\text{Lin} \frac{h_{sat,Ti} - h_{air,in}}{h_{sat,Ti} - h_{air,outi}}} \quad (13)$$

where  $h_{sat,Ti}$  is the specific enthalpy of the saturated air at the interface temperature ( $\text{kJ/kg}$ ).

The average of spray water temperatures was taken as the interface temperature according to Olivera & Facao 2004 as well as Stabat & Marchio 2004 while the inlet and outlet air enthalpies were taken from the psychrometric chart according the measured data.

Spray heat transfer coefficient which takes place between tubes external surface and spray water was calculated by equ. (16) which presented by Olivera & Facao, 2004. Experimental data were used to calculate this coefficient after calculating the overall heat transfer coefficient,  $U_o$ , between water inside tubes and the interface based on the outer area of the tube according to equ. (14):

$$Q = \dot{m}_{cw} C_{p,cw} dT_{cw} = U_o A LMTD \quad (14)$$

where LMTD: is the logarithmic mean temperature difference ( $^{\circ}\text{C}$ ) defined as:

$$LMTD = \frac{T_{CW,out} - T_{CW,in}}{\ln \frac{T_{CW,out} - T_{sp,av}}{T_{CW,in} - T_{sp,av}}} \quad (15)$$

where  $T_{sp,av}$  is the average spray water temperature,  $^{\circ}\text{C}$ .

After the overall heat transfer coefficient was calculated, it was used to calculate the spray heat transfer coefficient between the tubes external surface and spray water film:

$$\alpha_s = \left[ \frac{1}{U_o} - \frac{D}{\alpha_w \cdot d} - \frac{D}{2k_{tube} \ln D} \right]^{-1} \quad (16)$$

where  $\alpha_w$  is the heat transfer coefficient for water inside the tubes ( $\text{W}/\text{m}^2 \cdot ^{\circ}\text{C}$ ) and it was calculated according to Stabat & Marchio 2004 by the following equation:

$$\alpha_w = 0.023 \text{Re}^{0.8} \text{Pr}^{0.3} k_{cw} / d \quad (17)$$

Reynolds number and Prandtl number were taken for the water inside tubes with values of 7.13 and 11767 respectively.

## 4. Results And Discussion

### 4.1 Spray Heat Transfer Coefficient, $\alpha_s$

Fig. 4 shows the effect of air velocity on the spray heat transfer coefficient,  $\alpha_s$ . It is clear that spray heat transfer coefficient increased slowly with increasing of air velocity. This is because that when

air velocity increases, the cooling water range increases and this leads to increase the overall heat transfer coefficient and then to increase the spray heat transfer coefficient. This figure shows that the use of packing has a good effect in enhancing the spray heat transfer coefficient because the packings make the cooling water range to be larger. A correlation for spray heat transfer coefficient was concluded from the experimental results for the case of cooling tower without packings and it conforms well to the experimental values of this experiment as seen in this figure. This correlation is given by:

$$\alpha_s = 555 (\dot{G}_{air})^{0.075} \left( \frac{r}{D} \right)^{0.48} (T_{sp,ave})^{0.1} \quad (18)$$

Fig. 5 shows the effect of the ratio of L/G on the spray heat transfer coefficient. This figure illustrates that the spray heat transfer coefficient decreases with increasing of L/G. This can be attributable to the fact that when L/G increases; the air flow becomes insufficient to transfer the same amount of heat. In case of using packing in the tower operates the spray heat transfer coefficient is increased due to increasing of the surface area.

Fig. 6 indicates that the heat transfer coefficient increases with increasing spray water flow rate. This can be explained by equ. (14). When spray flow rate increases, the cooling capacity increases too leads to increase the overall heat transfer coefficient,  $U_o$ , and then  $\alpha_s$  increases according to equ. (16). This figure also shows that the presented correlation of spray heat transfer coefficient conforms well to the values of spray heat transfer coefficient of this experiment when packing were not used. If this figure compared with Fig. 4, it can be noticed that the spray heat transfer coefficient depends greatly on spray flow rate and little on air velocity, this is clear by the difference between the exponents of spray and air flow rates in equ. (18). The average spray water temperature changes with respect to spray flow rate; this makes spray water temperature affects the spray heat transfer coefficient as it is clear in the presented correlation and this is conform with the correlation of the spray heat transfer coefficient that presented by Heyns & Kroger 2010.

When the wet bulb temperature increases, the spray heat transfer coefficient decreases as

shown in **Fig. 7**. This is simply because of the fact that the cooling capacity decreases with respect to the wet bulb temperature which leading to decrease the overall heat transfer coefficient and thus the spray heat transfer coefficient decreases. Spray heat transfer coefficient becomes larger with using packing as it compared with that when packing were not used as shown in this figure, but the difference in the values between the two cases decreases for high wet bulb temperatures.

Spray heat transfer coefficient influenced by the heat load as shown in **Fig. 8**. When the load increases the cooling water range was increased leading to increase the overall heat transfer coefficient according to equ. (14) consequently the spray heat transfer coefficient was increased. This figure also shows that the spray heat transfer coefficient as the packing used is 10.25 % higher than its values when the packing were not used.

In **Fig. 9** the spray heat transfer coefficient correlation which concluded in the present work, equ. (18), is compared with other previous works conducted by Nistu et al. 1969 for plain tubes of 16 mm outside diameter in a staggered arrangement and Olivera & Facao, 2004 for 222 staggered tubes of 10 mm outside diameter. This figure shows that the presented correlation falls with about to 11.6 % from Nistu et al. correlation and rises with about to 26.6 % above Olivera & Facao correlation .

#### 4.2 Mass Transfer Coefficient, $\alpha_m$

In **Fig. 10** it is shown that the mass transfer coefficient for water vapor between spray water film and air increases greatly as air velocity increases. This increasing in mass transfer coefficient can be attributable to the increase of water evaporation rate as air flow increases. When the packing added to the tower, mass transfer coefficient shows increasing in its values because of increasing in the surface area of mass transfer. A correlation for mass transfer coefficient was concluded from the experimental results for the case of cooling tower without packing as in equ. (19). This correlation conforms well to the experimental values seen in this figure.

$$\alpha_m = 0.063 (\dot{G}_{air})^{0.81} \left( \frac{L}{D} \right)^{0.1} \quad (19)$$

The mass transfer coefficient of water vapor between spray water and air with respect to the ratio of mass flow rate of spray water and air,  $L/G$ , is shown in **Fig. 11**. The experiment was conducted

keeping  $L$  constant and letting  $G$  to vary. From this figure, it is evident that mass transfer coefficient decreases with increasing of  $L/G$ . This is mainly return to that when  $L/G$  increases this means that air flow inside the tower will be unproportionate with spray flow which leads to decrease the capability of air to gain more water vapor and this decreases the mass transfer coefficient.

**Fig. 12** indicates that the mass transfer coefficient is influenced by spray water flow rate. As spray flow increases the mass transfer coefficient increases too. This mainly because that the increasing in spray flow means there is a large amount of water droplet could be evaporated and transferred to the air stream. This figure also shows that the presented correlation of mass transfer coefficient, equ. (19), conforms well to the values of this experiment when the tower operates without packing. The increasing rate in mass transfer coefficient with respect to spray flow is much less than that with respect to air flow, as seen in figure (10) and this is clear by the difference between the exponents of spray and air flow rates in the presented correlation of mass transfer coefficient equ. (19). This figure also shows that mass transfer coefficient increases when the tower operates with using packing material, due to increase the surface area of mass transfer.

When the wet bulb temperature of the inlet air increases, mass transfer coefficient increases slightly as shown in **Fig. 13**. But when the wet bulb temperature increased the difference between the outlet and inlet air enthalpy,  $\Delta h_{air}$ , is decreased with a rate less than that in the logarithmic mean enthalpy difference,  $LMhD$ , causing in increasing mass transfer coefficient. For example, for the case without packing, when wet bulb temperature increased from 20 to 32°C,  $\Delta h_{air}$  decreased from 39.75 to 5.6 kJ/kg with a ratio of 7.1 while  $LMhD$  decreased from 21.88 to 2.536 kJ/kg with a ratio of 8.63 and this was the reason to increase mass transfer coefficient from 0.241 to 0.293 kg/m<sup>2</sup>.s. This figure shows also that the tower operates with packing has higher values for mass transfer coefficient as it operates without packing.

In **Fig. 14** the influence of the heat load on the mass transfer coefficient is shown. It is clear that mass transfer coefficient increases slightly with increasing the heat load. This can be attributable to the increase in the outlet air enthalpy as heat load

increases which increasing the difference between the outlet & inlet air enthalpies which then affects the mass transfer coefficient according to equ. (12). This figure indicates that the mass transfer coefficient increases with about 7.78 % in case of the tower operates using packing.

In Fig. 15 the mass transfer coefficient correlation which concluded in the present work, eq. (19), is compared with other previous works conducted by Parker and Treybal, 1961 for 19 mm outside diameter staggered tubes, and Hasan and Serin, 2002 for 34 mm outside diameter staggered tubes arranged in 13 rows\*20 columns, and Olivera and Facao, 2004 for 222 staggered tubes of 10 mm outside diameter. This figure shows that the presented correlation falls within the range of other correlations and it conforms well to them especially Hasan and Serin 2002.

## 5 CONCLUSIONS

The thermal performance of a small size indirect contact closed type cooling tower was investigated experimentally. It was found that the spray water flow rate has the greatest influence on the spray heat transfer coefficient,  $\alpha_s$ , but it is also a function of the air flow rate and the spray water temperature. In addition to this, both air and spray water flow rate affect the mass transfer coefficient,  $\alpha_m$ , but the great effect belongs to the air flow rate. The results of increasing the ratio of spray water to air mass flow rate indicate that it decreases the tower transfer coefficient. Correlations for spray heat transfer coefficient and mass transfer coefficient for ICCCT were concluded. These correlations was found to represent the experimental results very and also in a good agreement with the previous works. Wet bulb temperature was found to have a great influence on the characteristics of the tower. It decreases spray heat transfer coefficient while it increases mass transfer coefficient. The cooling water heat load increases both heat and mass transfer coefficients. The effect of packing material and then repeated using packing was found to have a relatively good enhancement on the cooling tower performance.

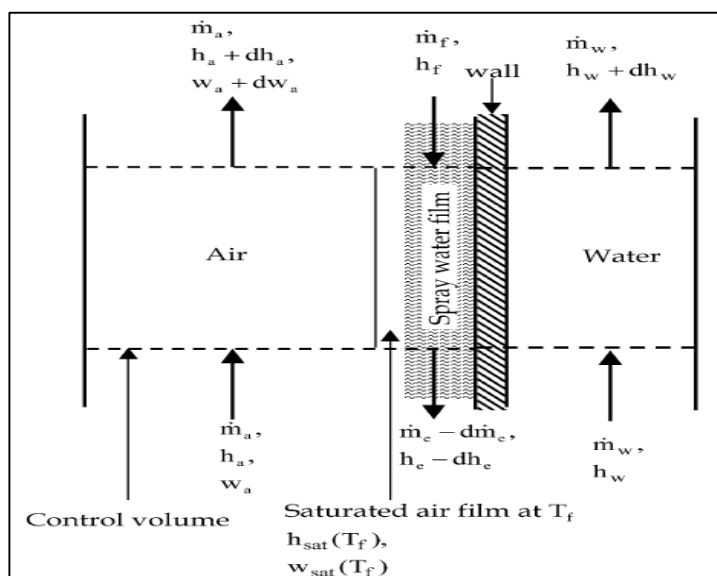


**Fig. 1** Heat & mass transfer mechanisms in the Indirect contact cooling tower

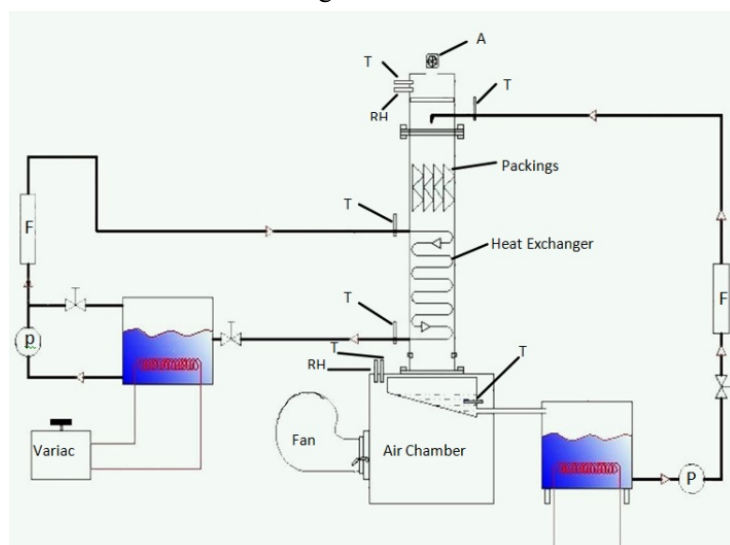


**Fig. 2** Schematic representation of the experimental apparatus

A: Anemometer    T: Thermocouple    RH: Relative Humidity Sensor    F: Flow Meter    P: Pump





Fig. 3 Photograph of the experimental apparatus

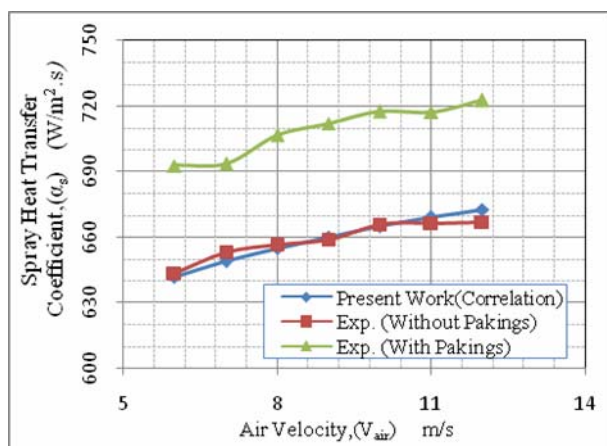


Fig. 4 Influence of the air velocity on spray heat transfer coefficient

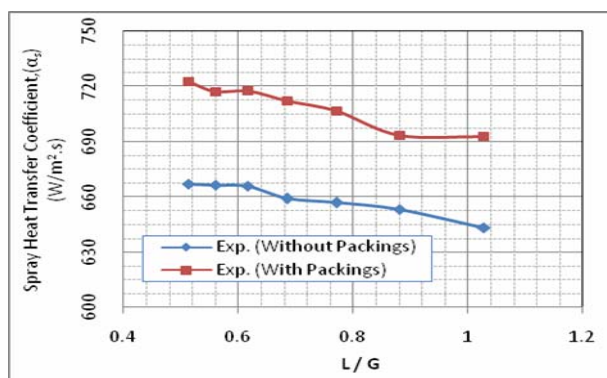


Fig. 5 Influence of spray water to air mass flow rate ratio on spray heat transfer coefficient

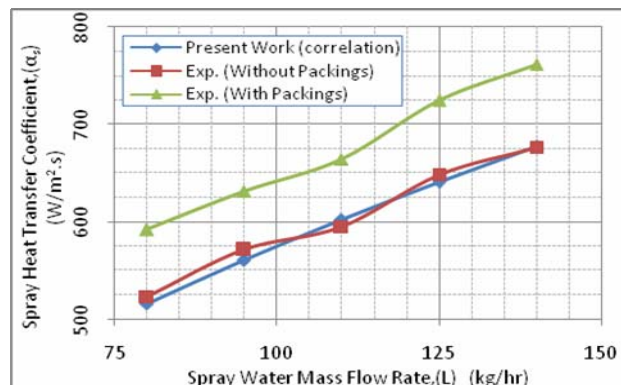


Fig. 6 Influence of the spray water mass flow rate on spray heat transfer coefficient

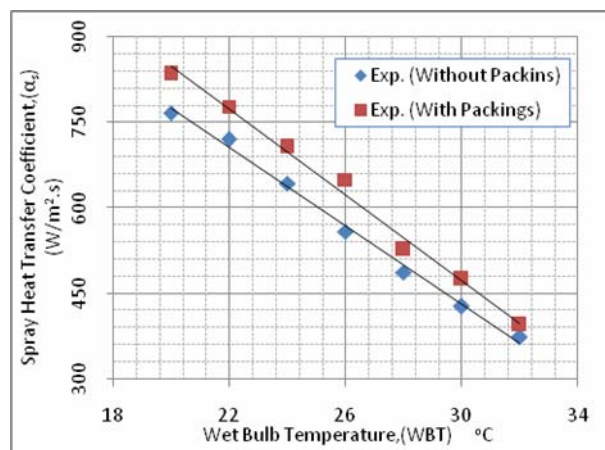


Fig. 7 Influence of the inlet air wet bulb temperature on spray heat transfer coefficient

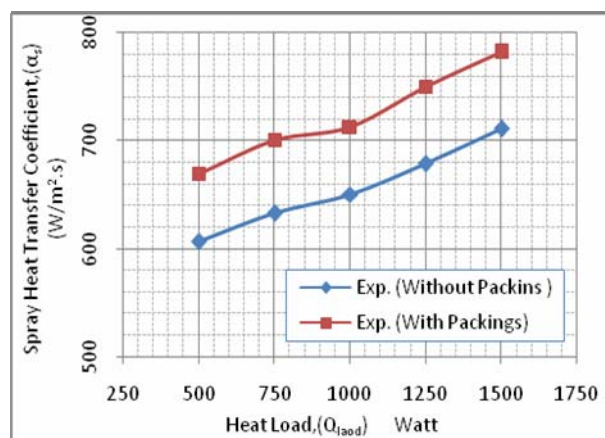
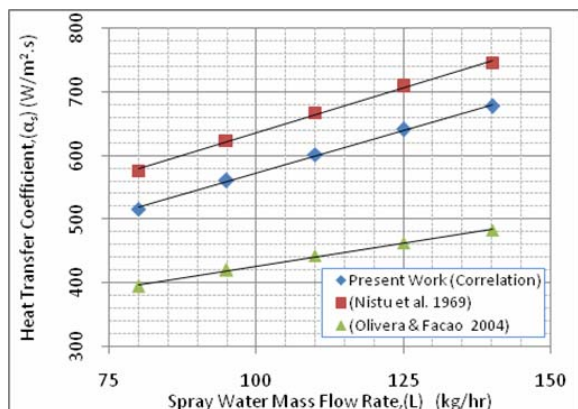
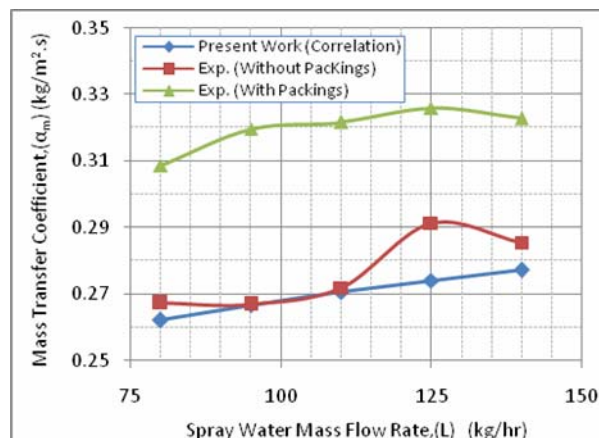


Fig. 8 Variation of spray heat transfer coefficient with respect to the heat load



**Fig. 9** Comparison of the presented correlation for the spray heat transfer coefficient with other works



**Fig. 12** Influence of the spray water mass flow rate on mass transfer coefficient

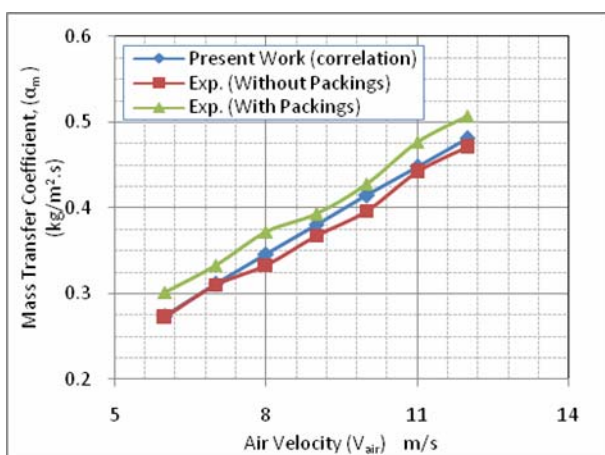


**Fig. 10** Influence of the air velocity on mass transfer coefficient

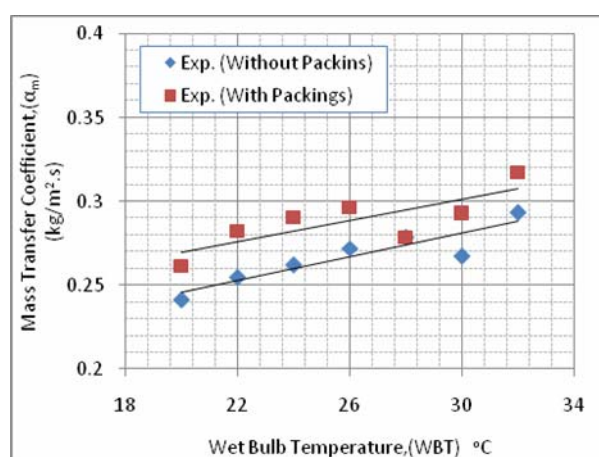


**Fig. 13** Influence of the inlet air wet bulb temperature on mass transfer coefficient

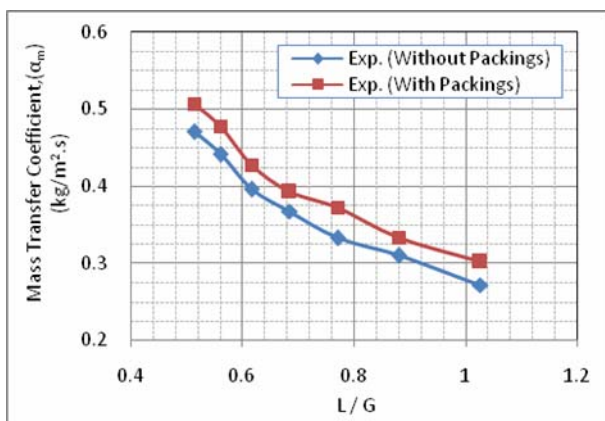


**Fig. 11** Influence of spray water to air mass flow rate ratio on mass transfer coefficient

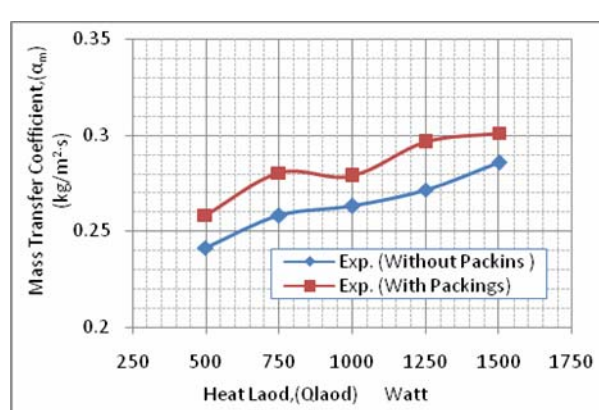


**Fig. 14** Variation of mass transfer coefficient with respect to the heat load

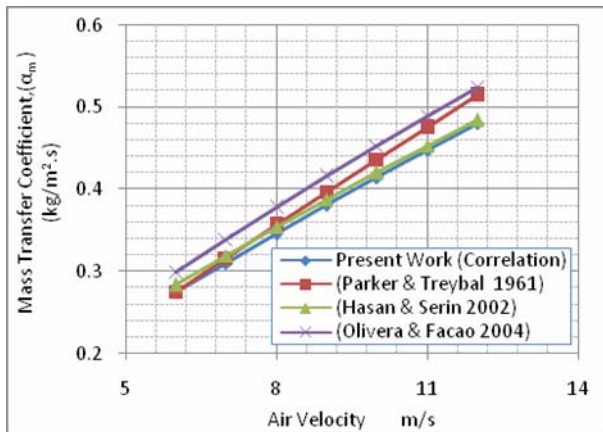


**Fig. 15** Comparison of the presented correlation for the mass transfer coefficient with other works

## REFERENCES

Oliveira A., and Facao J., 2004, "Heat and Mass Transfer Correlations for the Design of Small Indirect Contact Cooling Towers", *Applied Thermal Engineering*, Vol. 24, pp: 1969–1978.  
ASHRAE, 2000, *Equipment and Applications*.

Shim G.J., Baek S.M., Moon C.G., Lee H.S., and Yoon J.I., 2008. "Performance Characteristics of a Closed Circuit Cooling Tower with Multi Path". *World Academy of Science, Engineering and Technology*, Vol. 46, pp: 310-314.

Hasan A., and Sirén K., 2002, "Theoretical and Computational Analysis of Closed Wet Cooling Towers and Its Application in Cooling of Buildings", *Energy and Buildings*, Vol. 34, pp: 477 – 486.

Heyns J.A., and Kroger D.G., 2010, "Experimental Investigation into the Thermal-Flow Performance Characteristics of an Evaporative Cooler", *Applied Thermal Engineering*, Vol. 30, pp: 492–498.

Kern D. Q., 1978, "Process Heat Transfer". McGraw-Hill book company, USA.

Mizushima T., Ito R., and Miyashita H., 1967, "Experimental Study of an Evaporative Cooler", *International Chemical Engineering*, Vol. 7, No.4, pp: 727–732.

Nistu Y., Niato K., and Anzai T., 1969, "Studies on Characteristics & Design Procedure of Evaporative Cooler", *Journal of ASHREA, Japan*, Vol. 43, No. 7, pp: 581-590.

Parker R.O., and Treybal R.E., 1961, "The Heat Mass Transfer Characteristics of Evaporative Coolers", *Chemical Engineering Progress Symposium Series*, Vol. 57, No. 32, pp: 138–149.

Stabat P., and Marchio D., 2004, "Simplified Model for Indirect-Contact Evaporative Cooling-Tower Behaviour", *Applied Energy*, Vol. 78, pp: 433–451.

Yoo S.Y., Kim J.H., and Han K.H., 2010, "Thermal Performance Analysis of Heat Exchanger for Closed Wet Cooling Tower", *Journal of Mechanical Science and Technology*, Vol. 24, No. 4, pp: 893-898.

Walker W.H., and Lewis W.K., Mcadams W.H., Gilliland ER, 1923. *Principles of Chemical Engineering*. 3rd Ed. New York: McGraw-Hill Inc.

## NOMENCLATURE

A	Area (m <sup>2</sup> )
C <sub>p</sub>	Specific heat at constant pressure (kJ/kg °C)
D	Outer tube diameter (m)
d	Inner tube diameter (m)
G	Air mass flow rate (kg/hr)
$\bar{G}$	Air mass velocity based on minimum Section = $\rho v$ (kg/m <sup>2</sup> .s)
h	Specific enthalpy (kJ/kg)
k	Thermal conductivity (W/m °C)
L	Spray water mass flow rate (kg/hr)
$\dot{m}$	Mass flow rate (kg/hr)
Q	Cooling capacity (Watt)
Pr	Prandtl number
Re	Reynolds number
T	Temperature (°C)
U <sub>o</sub>	Overall heat transfer coefficient (W/m <sup>2</sup> °C)
v	Velocity (m/s)

## Greek letter

$\alpha_m$	Mass transfer coefficient for water vapor, between spray water film and air (kg/m <sup>2</sup> s)
$\alpha_s$	Heat transfer coefficient between tube surface and spray water film (W/m <sup>2</sup> °C)
$\alpha_w$	Heat transfer coefficient for water inside the tubes (W/m <sup>2</sup> °C)
$\Gamma$	Spray water mass rate per length of tube (kg/m s)
$\rho$	Density (kg/m <sup>3</sup> )

**Sub-Script**

ave	Average
air	Air flow (a)
cw	Cooling water
in	Inlet
out	Outlet
i	Interface between spray water film & air
f	saturated air-spray water film
sat	Saturation properties
sp	Spray water (w)

**Abbreviations**

LMhD	Logarithmic mean enthalpy Difference (kJ/kg)
LMTD	Logarithmic mean temperature Difference (°C)
CWCT	Closed wet cooling tower
ICCCCT	Indirect contact closed circuit cooling tower
HVAC	Heating ventilation air conditioning



## Data Acquisition System for Wind Speed, Direction and Temperature Measurements

**Dr. Fouad Sh. Tahir**  
Lecturer

**Ayad M. Salman**  
Asst. Lecturer

**Dr. Jabbar K. Mohammed**  
Lecturer

**Wahab K. Ahmed**  
Engineer

**Energy and Renewable Energies Technology Center  
University of Technology  
Iraq-Baghdad**

### Abstract:

This paper describes the use of microcomputer as a laboratory instrument system. The system is focused on three weather variables measurement, are temperature, wind speed, and wind direction. This instrument is a type of data acquisition system; in this paper we deal with the design and implementation of data acquisition system based on personal computer (Pentium) using Industry Standard Architecture (ISA) bus.

The design of this system involves mainly a hardware implementation, and the software programs that are used for testing, measuring and control. The system can be used to display the required information that can be transferred and processed from the external field to the system. A visual basic language with Microsoft foundation classes (MFC) is the fundamental tool for windows programming. It has been used to build a Man-Machine Interface (MMI), which was used for processing and monitoring acquisition data from environment weather.

### الخلاصة

تتناول الدراسة الحالية توصيف لاستخدام الحاسوب كأداة مختبرية حيث تركز هذه المنظومة على قياس متغيرات الطقس كدرجة الحرارة وسرعة الرياح واتجاهها، إذ تمثل هذه الأداة المختبرية نوع من أنظمة استخلاص البيانات. لقد تناولت هذه الدراسة التعامل مع تصميم وبناء منظومة رقمية لاستخلاص البيانات تعتمد على الحاسوب الشخصي نوع (بننتيوم) من خلال استخدام معمارية الناقل الصناعي القياسي (ISA).

يتضمن تصميم المنظومة بشكل رئيسي من بناء الكيان المادي والكيان البرمجي الذي يستخدم لأغراض الفحص والقياس والسيطرة. للنظام القدرة على عرض المعلومات المطلوبة والتي يتم نقلها ومعالجتها من الحقل الخارجي إلى داخل المنظومة. لقد تم استخدام لغة فبجوال بيسك المصنفة كأساس الميكروسوفت كأداة أساسية لبرمجة النوافذ. حيث استخدمت هذه اللغة لبناء الربط البيئي لرجل الماكينة (MMI) والذي استخدم للمعالجة ومشاهدة البيانات المستخلصة من الطقس.

## 1. Introduction

Data acquisition systems is an interfacing unit between the real world of physical parameters, which are analog, and the artificial world of digital computation and control. With current emphasis on digital systems, the interfacing function has become an important one; digital systems are used widely because complex circuits are low cost, accurate, and relatively simple to implement. In addition, there is rapid growth in the use of microcomputers to perform difficult digital control and measurement functions (Gerd 2005).

Sensors are essential components in many applications, not only in the industries for process control but also in daily life for building's safety and security monitoring, traffic flow measuring, weather condition monitoring and etc. In weather monitoring, for instance, parameters such as wind speed, wind direction and temperature need to be measured ( $\pm$ ) thus sensors have always assigned the task for doing so.

Weather or climate plays an important role in human life. The thermal comfort of human being is known to be influenced mostly by six parameters, i.e., air temperature, radiation, air flow, humidity, activity level and clothing thermal resistance. The advancement in technology has made these small and reliable electronic sensors capable of monitoring environmental parameters more favorably (Kamarul and Chow 2006).

## 2. Type of Instruments for Wind Speed and Direction Measurement

The two instruments commonly used to measure wind speed and wind direction are the anemometer (wind speed) and the wind vane (wind direction).

### 2-1.Wind Direction Ssensor

The wind vane, illustrated in Fig. 1, measuring wind direction sensors are generally some variant of the familiar weather vane. Sensitivity is maintained by constructing the weather vane to rotate on bearings with minimal resistance. Electronic readout can be achieved using a potentiometer (a "wiper" contact connected to the vane slides over a wire-wound resistor). The resistance between the contact and one end of the wire resistor indicates the position of the vane. Alternative methods of readout

include optical and magnetic position sensors. Positional accuracy is  $\pm 5\%$  (John 2000).

### 2-2. Rotational Anemometer

Weather stations commonly employ a 3-cup anemometer. This consists of a vertical axis rotating collar with three vanes in the form of cups. The rotation speed is directly proportional to wind speed as shown in Fig.2. An alternative to the cup anemometer is a propeller anemometer in which the wind causes a propeller to rotate. There are several ways to obtain an electrical signal indicating the speed: a magnet attached to the rotating shaft can induce a sinusoidal electrical impulse in a pickup coil; a Hall effect sensor can be used; or the rotating shaft can interrupt a light beam, generating an electric pulse in a photo detector. Rotating anemometers can measure wind velocities from close to 0 up to  $70 \text{ m s}^{-1}$  (150 mph) (Ian 2001)

### 3. Integrated Circuit Temperature Sensor

This very cheap, simple means of temperature measurement or compensation for temperature in the range  $-40^{\circ}\text{C}$  to  $+110^{\circ}\text{C}$ . The integrated circuit, which looks like a small transistor, operates on a power supply between 4 to 30 volts, giving a linear output of 10 mV  $^{\circ}\text{C}^{-1}$ , with an accuracy of  $\pm 0.4^{\circ}\text{C}$  (Telemetry Group 2005).

## 4. Computer Measurement and Control Hardware Requirement of the Present Work

The computer interface system hardware comprises mainly of the following unit:

- Input and output interface circuit.
- Data acquisition system.
- Transducer.

### 4-1. Input and Output System Hardware

The system hardware was designed and built for real time computer control and measurement operation. The designed process system is interfaced to (Pentium 1) microprocessor system via a group of buffering and latching gate, each having 8-bit I/O port which are used to adapt with other external hardware system as shown in the detailed interface circuit diagram of Fig.3 (Telemetry Group 2005 and K. Lacanette1997). The address that are used and the functions performed by each unit are mapped in Table 1.

## 4-2. Data Acquisition System

The data acquisition system was designed to transfer 8-bit data system variable (temperature, direction, and wind speed) to the microcomputer system.

An 8-bit, 8-channel unipolar (ADC0808) analog to digital converter based on successive approximation is used for measuring three different variable (wind direction, wind speed, and weather temperature) each one of the measured variable use a separated input channel in the analog to digital chip.

The data acquisition is started by selecting the required channel to be converted, the selector line come from one bit in the output port. The conversion is initiated by start conversion pulse that is applied from the computer through another bit of the same selector output port. Then the status of the A/D is read by means of input port to ensure the conversion is complete. The basic units of data acquisition system are interconnected as shown in details of **Fig.4 (D.C. Ramsay 1996 and Chuck Hellebuyck, 2003)**.

## 4-3. The Transducer (Gods Atul P., 2008 and Patil C. Y., 2008)

The wind-vane transducer shaft is internally coupled to 20k $\Omega$  potentiometer for measuring shaft position and wind direction; this potentiometer has a complete 360° rotation with no rotation stop.

The anemometer shaft is internally coupled to magnetic reed switch. Each revolution of the anemometer produces one contact closure of the reed switch.

The data acquisition system has a number of 8-analogue channels inputs designed to be connected to analogue type measurement sensor. Other analog inputs can be added if we use network modules, these analog inputs are designed to interface to ground-referenced (0-5) VDC analog signals. The interfacing is capable of measuring the frequency of a periodic input signal (digital) with the accruing required for this interface. To be compatible with interface analog input, a signal is needed that varies from 0 to 5 VDC and is proportional to wind direction. The wind-vane shaft is directly connected to the wiper of 20-k potentiometer. Therefore the position of the pot wiper always indicates wind direction.

It's a simple matter to connect the ends of the potentiometer to ground and to +5VDC. The wiper voltage then varies from 0V(0 degree) to 5V(360 degree) as the wind vane is rotated. The

relationship between the wiper output voltage and wind direction can be determined by:

$$\text{Wind Direction} = \frac{V_{\text{out}}}{5V} \times 360^\circ \quad (1)$$

This relationship assumes that the potentiometer is completely linear. The first step in the design of the wind speed interface is to calibrate the anemometer to correlate wind speed versus switch-closure frequency. To accomplish this step, we mounted the wind transducers to the spare tire carrier at the rear of our truck. Then, we drove the vehicle on a virtually windless morning at speeds spanning the input range of the anemometer while measuring the switch-closer frequency. Before attempting this experiment we also had our vehicles speedometer professionally calibrated since our new tire diameter differed from the original tires. The recalibration resulted in a fixed indicted speed offset of about +3MPH. The results of our data collection which has measured experimentally are presented in **Fig.5**. The manufacturer subsequently verified our finding-one switch closure per second (or 1 Hz) equaled 2.33MPH. Thus, over the wind speed range of interest (0-115MPH) the switch closure frequency varies from (1Hz=2.3MPH) to (50Hz=115MPH).

There are many ways to convert a variable frequency signal in to DC voltage. This type of circuit, often known as a tachometer circuit is implemented most often using a single-chip FN converter integrated circuit. The circuit consists of an input comparator, one-shot, and integrator.

Each time the input signal crosses the comparator threshold; it activates the one-shot, which switches a precise amount of charge in to the integrator input for a measured time period. As the input signal increases in frequency, the charge injected into the integration capacitor increase proportionally. The result is an average output voltage from the integrator proportional to the input signal frequency.

Obviously, this job was better suited to a digital counter or micro controller. We choose microchips PIC16C54 due to the circuit designs simplicity, low parts count, and program flexibility. In the approach we followed, the wind speed transducer is connected directly to an input bit of the PIC micro-controller.

An 8-bit D/A configured for an output range 0-5 volts DC is connected to eight of the PIC general-purpose I/O bits, which are configured as outputs.

To measure wind speed, the PIC simply counts the number of anemometer switch closures during a predetermined time period (frequency). This count is then scaled to obtain the 8-bit digital value, which drives the DAC. The scale factors ensure that the digital output is equal to 225 when the input frequency is equal to 50 Hz (115 MPH).

The DAC output voltage is always proportional to the wind speed as measured by the anemometer. The software programmed to measured frequencies up to 50 Hz in 1Hz increments. Thus, wind speeds up to 115 MPH can be measured in increments of 2.3 MPH. Therefore, at a wind speed of 0 MPH, the output voltage of the circuit is 0 volt, and it is 5 volt with a wind speed of 115 MPH.

The relationship between the DAC output voltage and wind speed can be found by the following equation:

$$windspeed = \frac{V_{out}}{5V} \times 115 \quad (2)$$

By using a micro-controller, we can measure switch closure frequency (and thus, wind speed) with greater resolution than 1 Hz. in our application, however, this level of precision was unwarranted. The circuitry required to interface the wind speed and direction transducers is shown in **Fig.6**.

For weather temperature measurement we need a transducer to sense this temperature. For our work we use LM334 a three terminal adjustable current source, as a temperature sensor because it is reliable, economical and compact in size. The output current  $I_{set}$  of the LM334 is directly proportional to absolute temperature in Kelvin (k) and is given by

$$I_{set} = \frac{(227uv/k)(T)}{R_{set}} \quad (3)$$

where:

$I_{set}$ = output current of the LM334.

$R_{set}$ =resistor that determines  $I_{set}$  and is connected between R and V terminals of LM334.

T=temperature in Kelvin.

To express the output voltage  $V_o$  of the LM334 in terms of  $I_{set}$  and  $R_L$  we will use the connection diagram of the LM334 shown in **Fig. 7**. And equation (3). In other words the output voltage will be.

$$V_o \approx I_{set} R_L$$

$$V_o \approx 10m \text{ V} / K \quad (4)$$

To condition the output signal of the temperature transducer to make it suitable for the ADC o8o8 we will use a voltage follower and differential amplifier as shown in **Fig.8**. Because the voltage follower eliminate loading and differential amplifier provides the gain necessary to make the signal suitable for the ADC.

## 5. System Software (Barry B. Brey, 2007)

The software of the system consists of two main parts: Man-Machine Interface software and control software. Man-Machine interface software is application independent. And it plays the role of an interface between the operator and the system. While the control software is application dependent and must be written specially for the used control hardware (plug-in card).

The control software is lightly linked to the Man-Machine interface software, and the two must be worked together to make the system software function. The system software was implemented by using visual basic language, which is fundamental programming for windows. We deals with visual basic software programming because it is easy to use and has a speed adequate for most application (the exception is control of the analog-digital-converter, a process which requires precise timing).

The program begin with an initialization procedure which configures the computer for the correct channel of the variable measurements, setup the necessary data array-and performs other housekeeping chores. The user is then given the opportunity to plot data stored on a hard-disk from a previous measurements, or to run the operation of measurement itself, if the user chooses to begin the measurement task the program immediately goes in to the data acquisition software which acts as controller, prompting other program which collect the data, manipulated data, and display the variables on user window as a real value or display it as graphics. The user window which represent the Man-Machine interface software is shown in **Fig. 9**.

The procedure represents the main program which was used to initialize the procedure of measuring the weather variables is illustrated in following steps:

- 1- Start.
- 2- initialize the input ports of the system.
- 3- select the digital to analog (ADC) input port.
- 4- Send start conversion signal to ADC unit.

- 5- Check the ADC status , If it is true then end the conversion operation and input the binary data to the computer system and go to step 6 .Else take few second and return to check the ADC status.
- 6- Manipulated the digital raw input data.
- 7- save the information in specific array on hard disc and display the weather variable on the user window.
- 8- If you want to repeat the weather variables measuring go to step 3, else go to step 9.
- 9- End.

## 6. Results and Discussion

The proposed system was calibrated through using advanced equipment meter type PROVA, which contains a thermometer and anemometer sensor.

The results which were obtained from the proposed system for five days were plotted in **Figs. 10** and **11** for temperature and wind speed measuring results and the wind direction results for five days are put it in table 2.

The measurements of the variables have been compared with the same variables value obtained from portable measurement equipment type PROVA (AVM-07) and the results which observed in **Figs. 12** and **13**. From this comparison show us very good level of stability as well as accuracy.

## 7. Conclusions

The focus of the paper is in using digital data acquisition system based on microcomputer for measuring a multi type of variable.

The following points are the most important outline which obtained from this paper.

1. The system usefulness is as a teaching tool that let engineers and scientific user to exercise their programming skills in order to

Acquire and store, process data and display the process in to engineering form.

2. Data acquisition system based on microcomputer is more efficient and economical than conventional system because it can be programmed at predetermined time.
3. The graphics capabilities of the microcomputer have been exploited so that several system variables can be observed simultaneously. Consequently, no additional recording instruments are required.(Hence the computer will store all the data on hard disk, and we don't need an external storage devices.
4. The general purpose nature of the microcomputer based system has been demonstrated and also we have been considered for illustrating basic important concept of data acquisition for real-time multi-variable measurement system.
5. Data acquisition system based on microcomputer provides the user with flexibility of selecting various variable type of process measurement. The system has the ability to deal with multi-variable at the same time.
6. The use of digital techniques for data acquisition system makes these systems more accurate, reliable, and simpler.

**Dr. Fouad Sh. Tahir**  
**Ayad M. Salman**  
**Dr. Jabbar K. Mohammed**  
**Wahab K. Ahmed**  
**References**

## **Data Acquisition System for Wind Speed, Direction and Temperature Measurements**

Ian R.Sinclair"sensors and transducers", Butterworth-heinemann,2001.

John D .Garrison,"Environmental Measurement.",CRC Prees.2000.

K. Lacanette, "National Temperature Sensor Handbook.",Nattional Semiconductor Corporation,1997.

Kamarul Ariffin , Chow Chee,"Microcontroller-based Weather Monitoring System", university of mallaya ,CMU.gournal,VOL 5,2006.

Patil C. Y., "8-Bit Microprocessor Microcontroller", Delhi Satya Prakashan, 2008.

Telemetry Group, "Instrumentation Engineers Handbook", December, 2005.

Barry B. Brey , "The Intel Microprocessor, Programming and Interfacing" prentice –Hall, Inc., 2007.

Chuck Hellebuyck"Programming PIC Microcontroller with PICbasic",Elsevier science USA,2003.

D.C. Ramsay, "Principles Of Engineering Instrumentation", Halstead Press an Imprint Of Wiley & Sons INC., New York,1996.

Gerd Wostenkuhle ,"Measuring system Design", john wiley & sons,Ltd,2005.

Gods Atul P., "Microprocessor Microcontroller and Applications", India Technical Puplications Pune, 2008.

**Table 1 Input And Output Address Mapping.**

Addresses	Function description
300 H	Address of analogue channel select
301 H	A/D enable and start conversion
302 H	Statue of A/D (EOC)
303 H	A/D data reading enable

**Table. 2 Illustrated the results of wind direction for five days.**

Time (hr)	Date				
	1/11/2010	7/11/2010	14/11/2010	21/11/2010	28/11/2010
	Direction				
1	NE	N	WN	WN	NW
2	NE	N	NW	NW	WN
3	N	NW	NW	NW	NW
4	N	N	NW	WN	NW
5	N	W	NW	W	WN
6	N	W	W	W	WN
7	N	W	WN	WN	NW
8	NW	WN	WN	N	NW
9	NE	NW	NW	N	NW
10	N	NW	WN	NW	NW
11	NE	N	NW	WN	NW
12	NE	N	NW	WN	WN
13	N	NE	NW	WN	WN
14	NE	NE	WN	W	NW
15	NE	W	WN	W	NW
16	NE	N	WN	WN	WN
17	N	N	N	WN	WN
18	N	WN	N	N	W
19	NW	NW	NE	N	NW
20	NW	N	NE	NE	NW

21	NW	NE	N	E	WN
22	NW	NE	NW	NE	NW
23	NW	N	NW	N	W
24	NW	N	W	WN	W



**Fig. 1 Illustrates Wind Direction Sensor.**



**Fig. 2 Illustrate Types Of Wind Speed Sensor.**



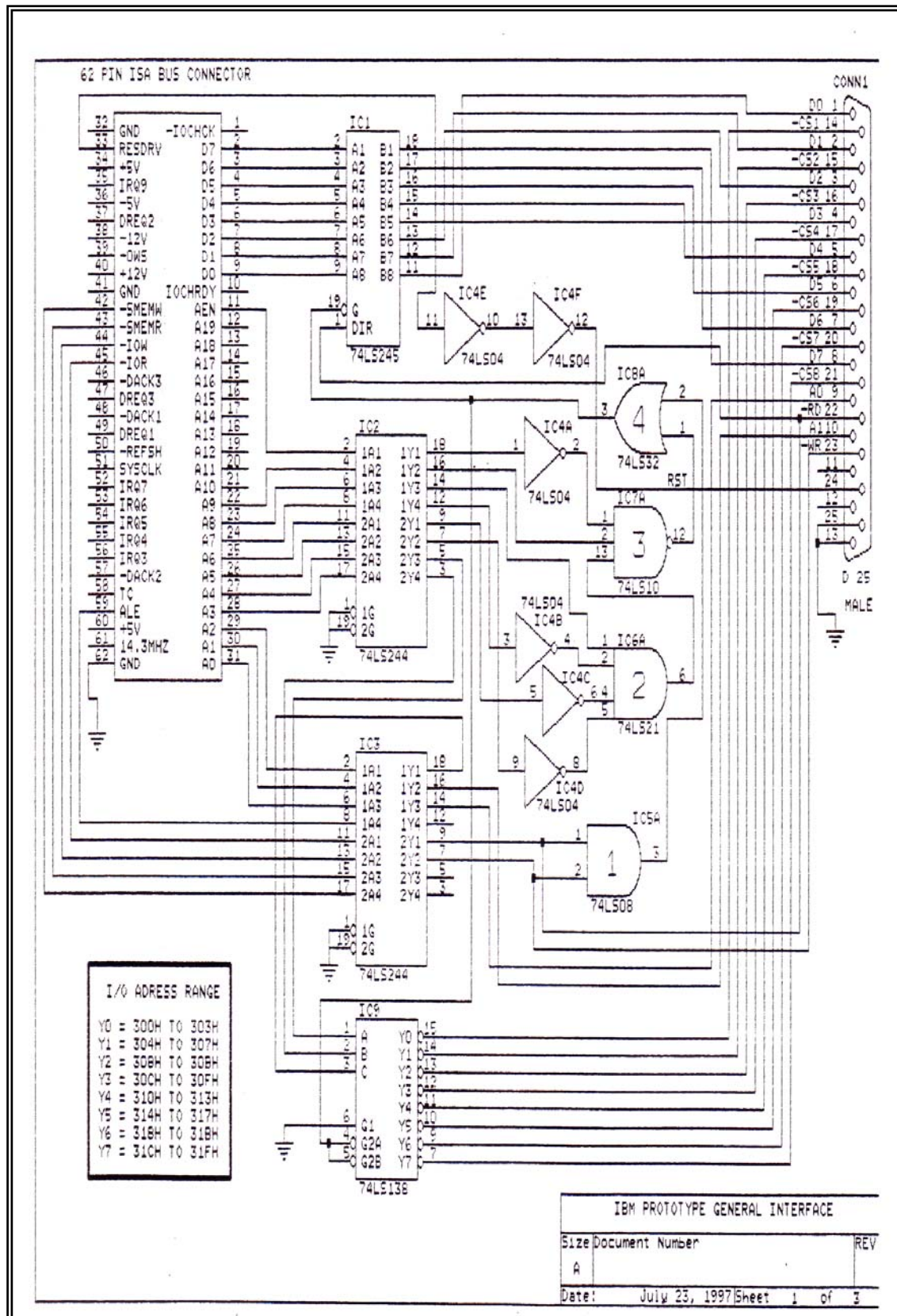


Fig. 3 Illustrate The Detail Of Digital Interfacing Circuit For ISA Bus.



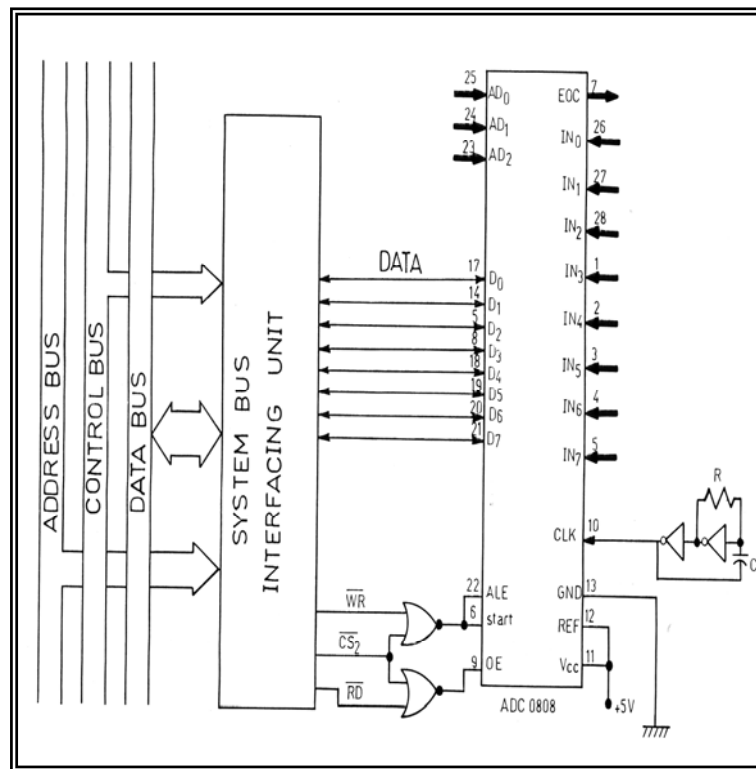


Fig. 4 Illustrates The Data Acquisition System.

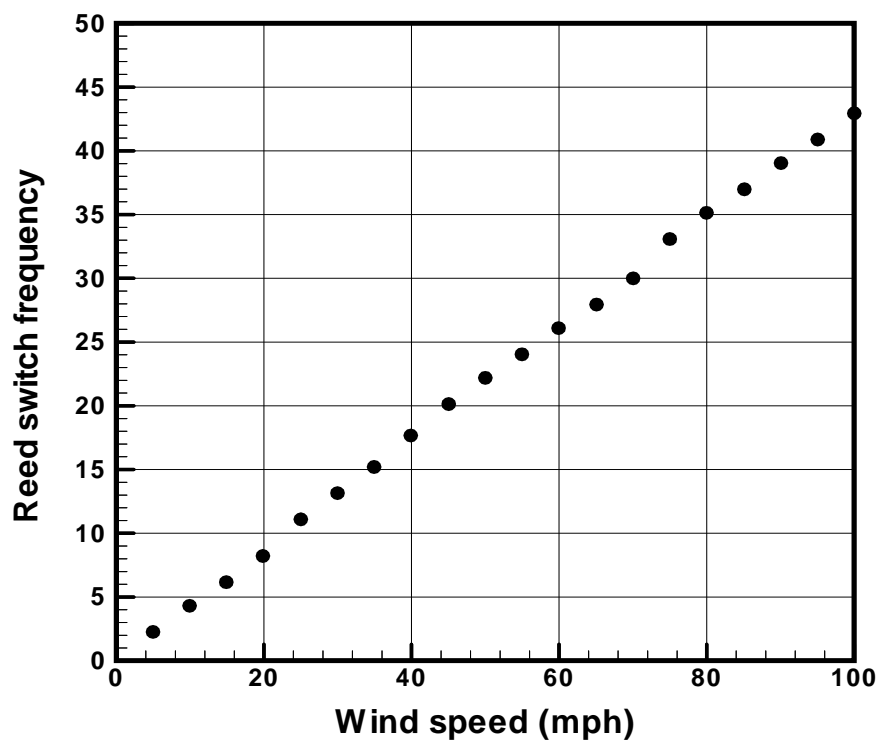


Fig. 5 Illustrate A Relations Ship Between The Reed Switch Frequency And Wind Speed.

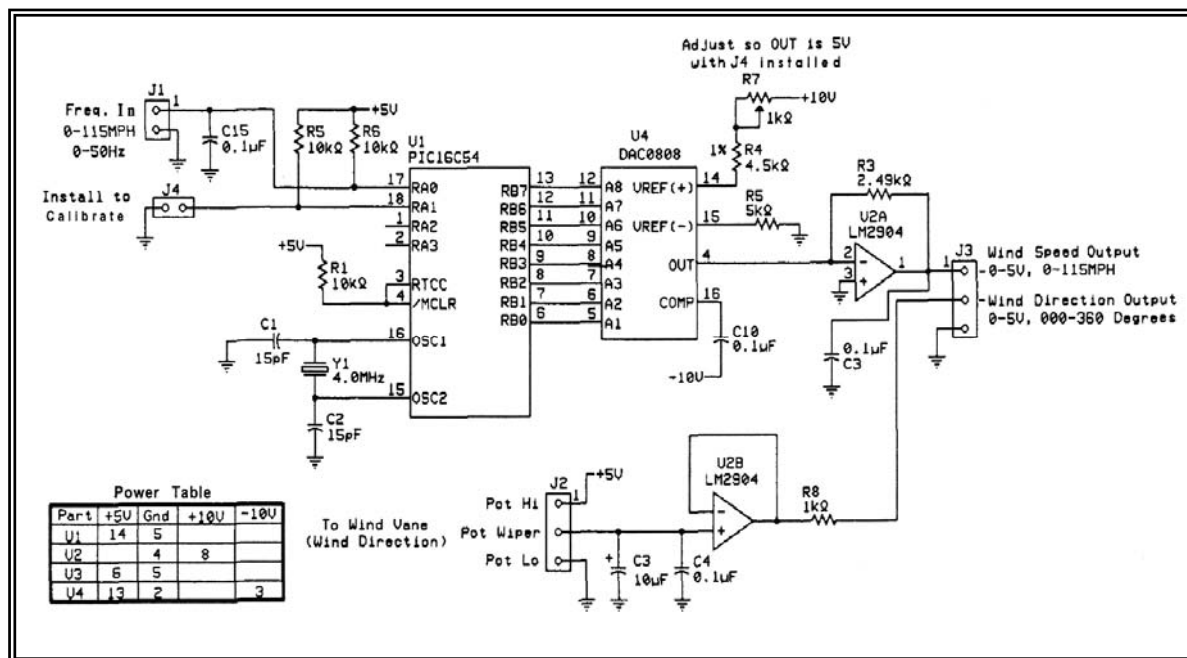


Fig. 6 Illustrate the Electronic Circuit Details Wind Speed and Direction Transducer.

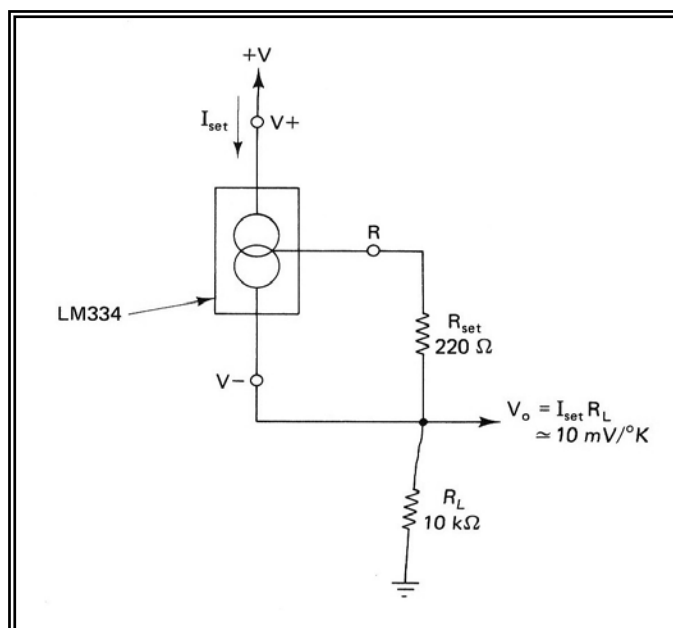
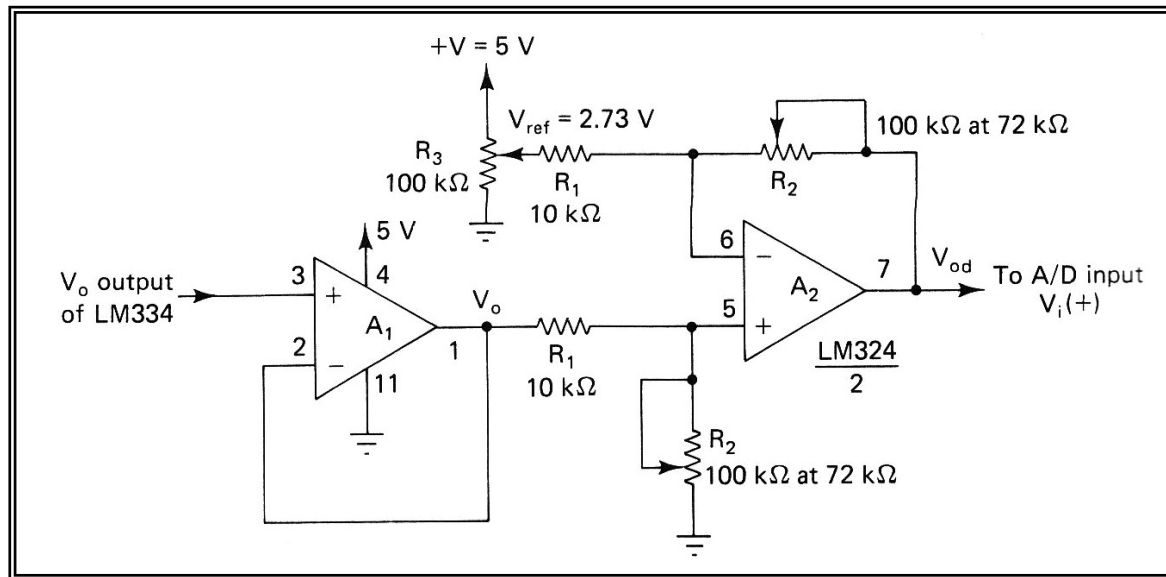
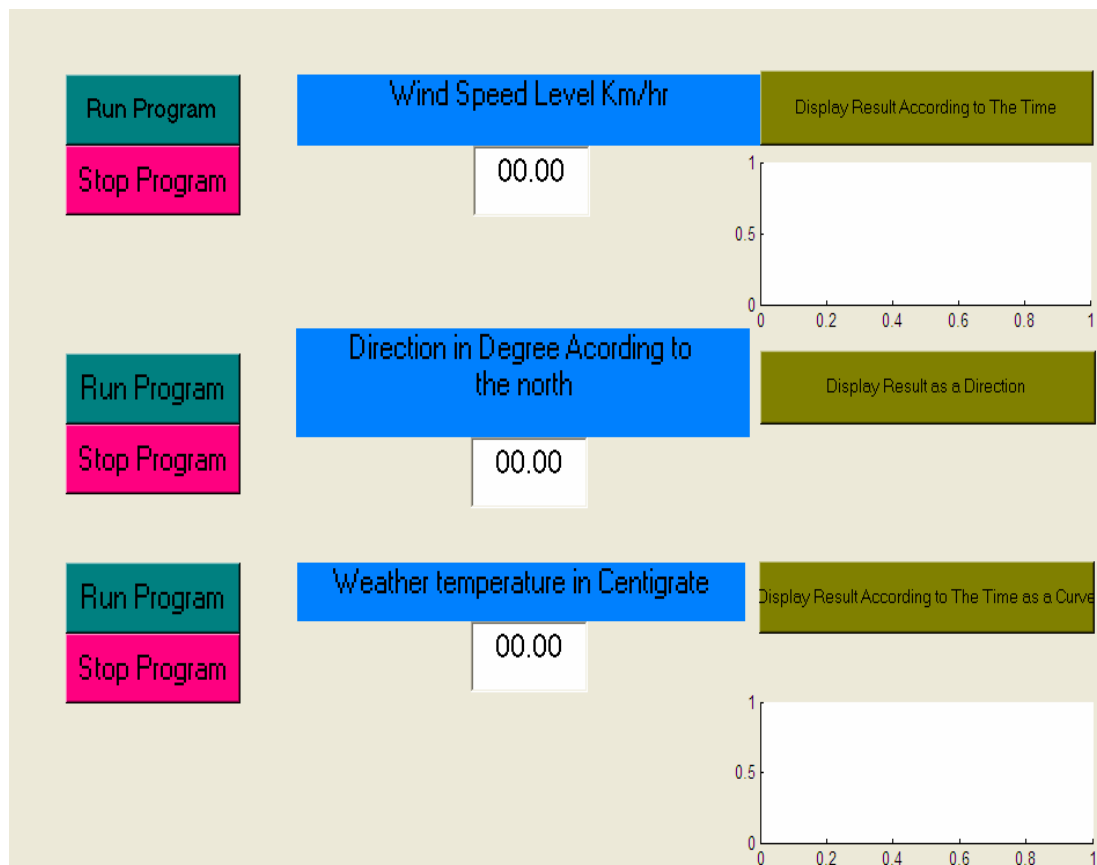


Fig. 7 Illustrate LM334 Connection Diagram.



**Fig. 8 Illustrate the Signal Conditioning Through Voltage Follower and Differential Amplifier.**



**Fig. 9 Illustrate User Window (Man-Machine Interface) MMI.**

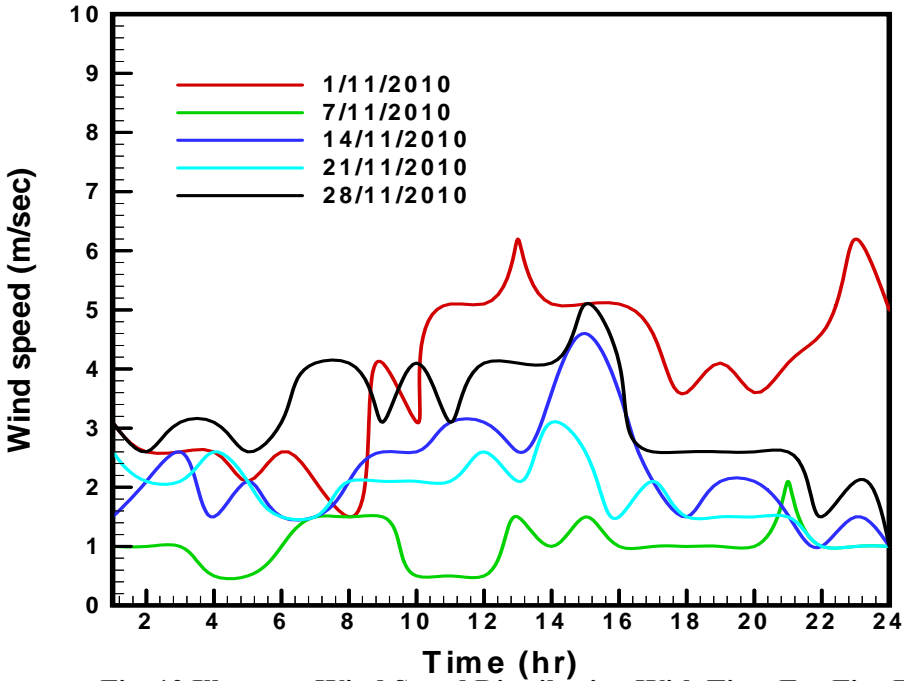


Fig. 10 Illustrate Wind Speed Distribution With Time For Five Days.

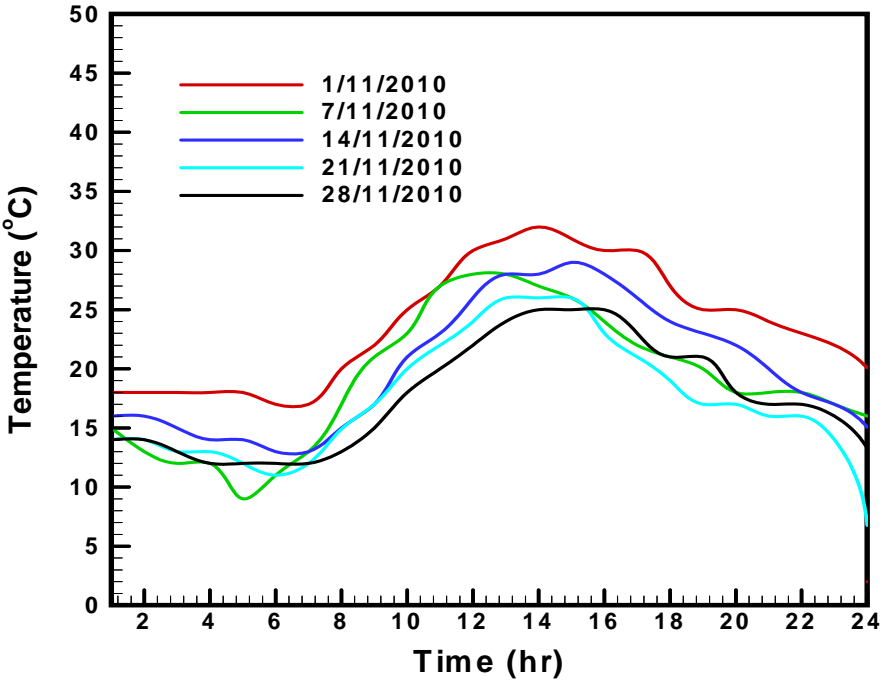


Fig. 11 Illustrate Temperature Distribution With Time For Five Days.

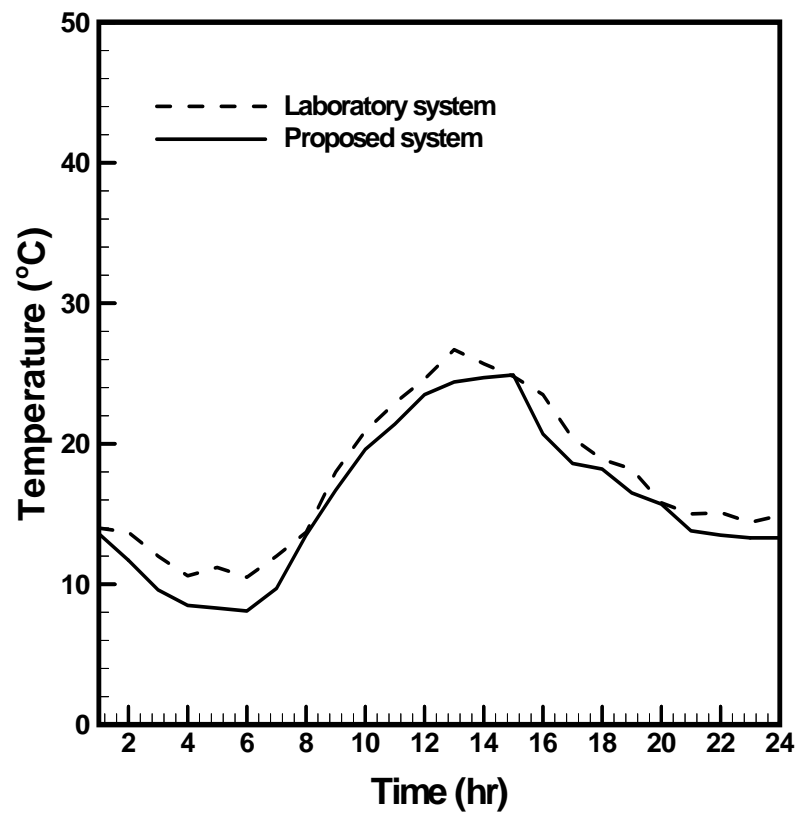


Fig.12 Illustrate The Comparison Of Temperature For Proposed System And Laboratory System.

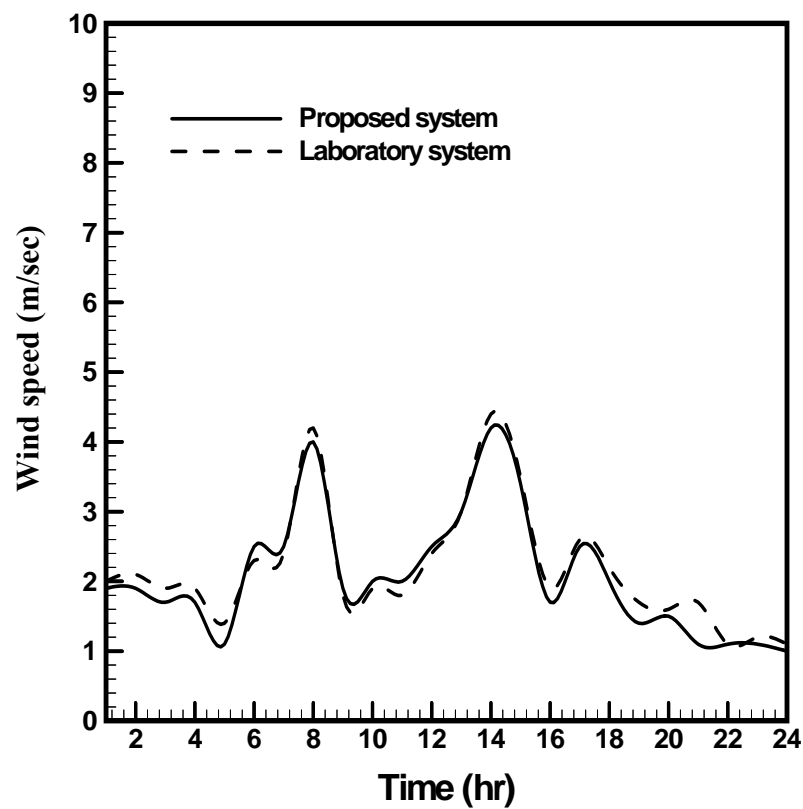


Fig.13 Illustrate The Comparison Of Wind Speed For Proposed System And Laboratory System.



## Hybrid Controller for a Single Flexible Link Manipulator

Waladin K. Sa'id  
Control Systems Dept.  
University of Technology Baghdad, Iraq  
[waladinksy@yahoo.com](mailto:waladinksy@yahoo.com)

Bahaa I. Kazem  
Mechatronics Eng Dept.  
University of Baghdad  
[bahaak@mit.edu](mailto:bahaak@mit.edu)

Alya'a M. Manaty  
College of Science  
University of Thi-Qar  
[alyaanow@yahoo.com](mailto:alyaanow@yahoo.com)

### Abstract

In this study, the dynamic modeling and step input tracking control of single flexible link is studied. The Lagrange-assumed modes approach is applied to get the dynamic model of a planner single link manipulator. A Step input tracking controller is suggested by utilizing the hybrid controller approach to overcome the problem of vibration of tip position through motion which is a characteristic of the flexible link system. The first controller is a modified version of the proportional-derivative (PD) rigid controller to track the hub position while sliding mode (SM) control is used for vibration damping. Also, a second controller (a fuzzy logic based proportional-integral plus derivative (PI+D) control scheme) is developed for both vibration damping and hub position tracking. A comparison is made between the performances of these two controllers. The Hybrid controller with PD and SM shows better tracking behavior than obtained from the suggested fuzzy (PI+D)<sup>2</sup> controller for a single link flexible manipulator.

**Keywords:** Flexible Link, Single Link, Hybrid Control, Fuzzy Control.

/

### الخلاصة

في هذه الدراسة تم دراسة النموذج الديناميكي والسيطرة على حركة ذراع ذو وصلة واحدة single link. تم تطبيق طريقة لاكرانج - النمط الكفوء Lagrange-assumed modes approach للحصول على نموذج ديناميكي لذراع الانسان الآلي. وتم الحصول على نموذج خطي للذراع ذو الوصلة الواحدة والذي تم محاكاته باستخدام برنامج Matlab وأداة Simulink للتحليل والمحاكاة. تم اقتراح مسيطر لتتبع الادخال من فكرة المسيطر الهجين hybrid controller للتغلب على مشكلة الاهتزاز في طرف الذراع خلال الحركة والذي هو من صفات الهياكل المرنة. حيث تم تصميم نسخة معدلة من مسيطر PD لتتبع مسار المفصل بينما تم استخدام سيطرة النمط المنزلق sliding mode لتخميد الاهتزازات. وكذلك تم تطوير مسيطر ثاني (مسيطر منطق مضيب Fuzzy (PI+D)<sup>2</sup>) كطريقة للسيطرة على كل من تخميد الاهتزازات وتتبع مسار المفصل. وتمت مقارنة نتائج اداء المسيطرين والتي تظهر بوضوح تفوق عمل المسيطر الهجين من النوع الاول مقارنة مع مسيطر المنطق المضيب المقترح.

## 1. Introduction

Many of today's robots are required to perform tasks which demand a high level of accuracy in end-effector positioning. Most robots cannot directly sense this position and instead calculate it using the joint angles and forward kinematics equations. This technique assumes that the links connecting the joints are rigid, and thus many robots have large, heavy links which behave like true rigid links. This prevents oscillations in the links which cause errors in the calculated end-effector position. Since the links are heavy, much of the joint motor's power is expended moving the link and holding them up against gravity. Also payloads must be kept quite small compared to the mass of the robot itself, since large payloads will cause sagging and vibrations in the links which create uncertainty in end-effector position. This results in a situation where these rigid robots are very inefficient and slow. In an attempt to solve these problems, the field of flexible robots was created, Natarajan et al (1998).

In order to fully exploit the potential offered by flexible robot manipulator, it is desirable to have an explicit, complete, and accurate dynamic model. This model must consider the effects of structural link flexibility and properly deal with vibrational behavior. Different schemes for modeling of the manipulators are studied by a number of researchers as described below. The mathematical models of the manipulators are generally derived from energy principles and for a simple rigid manipulator, the rigid arms store kinetic energy by virtue of their moving inertia and store potential energy by virtue of their position in the gravitational field, but the flexible arms store potential energy by virtue of the deflections of its links.

To include bending one may often use the Euler-Bernoulli equation which ignores shearing and rotary inertia effects. These two effects may be incorporated using a Timoshenko beam element which generally must be used if the beam is short relative to its diameter, Book et al (1990). In most models of flexible manipulators Euler-Bernoulli beams are used.

The robotic systems with flexible links are continuous dynamical systems characterized by an infinite number of degrees of freedom and are governed by nonlinear coupled, ordinary and partial

differential equations. The exact solution of such systems is not feasible practically and the infinite

Dimensional model imposes severe constraints on the design of controllers as well. Hence, they are truncated to some finite dimensional models using assumed modes method (AMM), finite elements method (FEM) or lumped parameters method.

In the literature a number of techniques for deriving equations of motions were used to develop the dynamic equations of motion of flexible link systems. Three main techniques were used by researchers, namely: Newton-Euler approach, Boyer et al (1996), Lagrangian approach, Geniele et al (1997), and Hamiltonian approach, Benati et al (1991).

The control difficulty of flexible arm is due to the non-collocated nature of the sensor and actuator positions which results in unstable zero dynamics. In other words, the nonlinear system is non-minimum phase. Therefore, the system has an unstable inverse dynamics. The non-minimum phase property makes exact asymptotic tracking of a desired tip trajectory impossible, if one employ causal controllers. Furthermore, the robot should handle a wide variety of payloads, the robustness of the control system becomes very important, Talebi et al (1996).

The control strategies considered in this field can be divided into open-loop and closed-loop methods. Open-loop control involves altering the shape of actuator commands by considering the physical and vibration properties of the system. The main source of vibration in the flexible manipulator is the motion itself. Thus, input torque profiles are generated by minimizing input energy at system natural frequencies, so that vibration in the flexible manipulator system is reduced during and after the move. Many types of shaped input strategies are developed on the basis of extracting the energies around the natural frequencies. These are, Gaussian shaped input, low pass filtered torque input and band-stop filtered torque input. While closed-loop control uses measurements of the system states and alters the actuator input in order to reduce the system vibration, Azad et al (2003).

A number of feed-back control strategies have been proposed in the literature for the end-point trajectory tracking in flexible manipulators. Book et al (1975) and Hasting et al (1987), employed linear control theory, while Singh et al (1986), De Luca et

al (1989), and De Luca et al (1991) made use of nonlinear decoupling. They recognized that a multi-link arm could not be controlled based on their approach because of nonlinearities in the dynamics of a multi-link arm.

Tang et al. (2006) focused on tracking control problem of flexible link manipulators. In order to alleviate the effects of nonlinearities and uncertainties, a combined control strategy based on neural network (NN) and the concept of sliding mode control (SMC) was proposed systematically. The chattering phenomenon in conventional SMC is eliminated by incorporated a saturation function in the proposed controller, and the computation burden caused by model dynamics was reduced by applying a two-layer NN with an analytical approximated upper bound, which was used to implement a certain functional estimate. In addition, the Lyapunov analysis can guarantee the signals of closed-loop system bounded and the online NN adaptive laws made the system states converge to the sliding surface.

Alwan et al (2008) suggested the dynamic model and control; of a robot with single flexible-link with revolute joint, which rotates in the horizontal plane. The dynamic equations are derived using the (assumed mode)/Lagrangian formulation, based on Euler-Bernoulli beam theory. Both the rigid degrees of freedom and the elastic degrees of freedom of the system are treated as generalized coordinate. Although the equations of motion of the system are highly nonlinear and coupled, due to the dynamic model derived in this work takes into account the coupling effects between rigid body motions and elastic deformation. The inverse dynamic method is used to present the Trajectory Control of Flexible Robot Arm; the desired position of the end point of the manipulator is given versus time, and the required joint torques are determined. The main difficulty is that the numerical solution of the inverse dynamic problem of flexible manipulators normally diverges. The computed joint torques can be used as feedforward controls which minimize the work of the feedback controller needed to compensate modeling errors.

In this work several control schemes have been suggested and simulated for step input to possessing interesting nonlinear and non-minimum phase features for one flexible link manipulator.

## 2-Dynamic Modeling Of A Single Flexible Link

The schematic of a planar single-link flexible manipulator is shown in **Fig. 1**. Where (X , Y) is an inertial coordinate frame, and (x , y) is the coordinate assigned for a flexible link moving with instantaneous Center of Mass (CoM).  $\theta$ ,  $w(x,t)$ ,  $\ell$ , and  $\tau$  represent the hub angular position, the deflection along the arm, the length of the link, and the torque applied to the hub, respectively.

Single link flexible arm modeled as an Euler-Bernoulli beam in rotation. At one end, the arm is clamped on a rigid hub mounted directly on the vertical shaft of a DC motor, the other end is free to flex in a horizontal plane, and has a mass  $m_p$  as a payload. It is assumed that the length of the beam,  $\ell$  is much greater than its width, thus restricting the beam to oscillate in the horizontal direction. Neglecting the effects of shear deformation and rotary inertia, the deflection of any point on the beam is given by the Euler-Bernoulli beam equation Thomson (1981).

The Euler-Bernoulli beam theory and the assumed modes method can be used to express the deflection  $w(x,t)$  of a point located at a distance  $x$  along the link as:

$$w(x,t) = \sum_{i=1}^n \phi_i(x) \delta_i(t) \quad (1)$$

where  $\phi_i(x)$  is the mode shape function and  $\delta_i(t)$  is the time varying modal function and  $n$  is the number of finite modes.

The absolute vector of a point along the link is described by:

$$P = \begin{bmatrix} p_x \\ p_y \end{bmatrix} = \begin{bmatrix} \cos \theta & -\sin \theta \\ \sin \theta & \cos \theta \end{bmatrix} \begin{bmatrix} x \\ w \end{bmatrix} = \begin{bmatrix} x \cos \theta & -w \sin \theta \\ x \sin \theta & +w \cos \theta \end{bmatrix} \quad (2)$$

In order to derive the equations of motion for this system which is a combination of a lumped parameter part (the hub rotation and the payload mass) and distributed parameter part (the link deformation); an energy-based method is the most convenient, i.e. Lagrange formulation. The Lagrangian,  $L$ , of the system can be determined by substituting equation for the total kinetic energy and the total potential energy ( $L = T - V$ ).



Therefore, the kinetic energy  $T$  and the potential energy  $V$  of the system have to be computed.

$$T = T_h + T_\ell + T_p \quad (3)$$

where  $T_h$  is the kinetic energy contributions from the hub:

$$T_h = \frac{1}{2} J_h \dot{\theta}(t)^2 + \frac{1}{2} m_h \dot{w}_0^2 \quad (4)$$

Where  $w_0$  is the deflection at the hub. From the geometric boundary condition this is equal to zero.  $T_\ell$  from the link: is:

$$T_\ell = \frac{1}{2} \int_0^\ell \dot{p}' \dot{p}' dx \quad (5)$$

Where

$$\dot{p}' \dot{p}' = \dot{w}^2 \dot{\theta}^2 + \dot{x}^2 \dot{\theta}^2 + 2\dot{x}\dot{w}\dot{\theta} + \dot{w}^2$$

Similarly, the kinetic energy associated with the payload can be written as:

$$T_p = \frac{1}{2} m_p \dot{w}_\ell^2 + \frac{1}{2} J_p \dot{\theta}(t)^2 \quad (6)$$

Where  $w_\ell$  is the deflection at the end of the link

The potential energy of the link is composed of two parts: the gravitational energy  $V_g$ , and the strain potential energy  $V_e$  owing to the flexure of the link Chapnik et al (1991),

$$V = V_e + V_g \quad (7)$$

Since the movement of the link is assumed in the horizontal plane only, the gravitational energy can be neglected. The potential energy resulting from the elastic deformation of the link is given by:

$$V_e = \frac{1}{2} \int_0^\ell EI w''^2 dx \quad (8)$$

The potential energy  $V_e$ , of the system is stored in the flexible modes and can be attributed to "modal stiffnesses"  $K$  which are evaluated by integrals over the length of the link.

Then the dynamic equations of the system can be derived using the Euler-Lagrange. A system with  $n+1$  generalized coordinates  $q$  must satisfy  $n+1$

differential equations of the form:

$$\frac{d}{dt} \left[ \frac{\partial L}{\partial \dot{q}} \right] - \frac{\partial L}{\partial q} = U \quad (9)$$

The computational details on various differentials and integrals can be found in Manaty

2008, results are a coupled set of second order dynamic equations:

$$M(q_i) \ddot{q}_i + C(q_i, \dot{q}_i) + D\dot{q}_i + Kq_i + g(q_i) = U \quad (10)$$

$$\begin{bmatrix} M_{rr}(q) & M_{rf}^T(q) \\ M_{fr}(q) & M_{ff}(q) \end{bmatrix} \begin{bmatrix} \ddot{\theta} \\ \ddot{\delta}_i \end{bmatrix} + \begin{bmatrix} C_{rr}(q, \dot{q}) & C_{rf}(q, \dot{q}) \\ C_{fr}(q, \dot{q}) & C_{ff}(q, \dot{q}) \end{bmatrix} \begin{bmatrix} \dot{\theta} \\ \dot{\delta}_i \end{bmatrix} + \begin{bmatrix} d_{rr} & 0 \\ 0 & D_{ff} \end{bmatrix} \begin{bmatrix} \dot{\theta} \\ \dot{\delta}_i \end{bmatrix} + \begin{bmatrix} 0 & 0 \\ 0 & K_{ff} \end{bmatrix} \begin{bmatrix} \theta \\ \delta_i \end{bmatrix} + \begin{bmatrix} g_r(q) \\ g_f(q) \end{bmatrix} = \begin{bmatrix} 1 \\ 0 \end{bmatrix} \tau \quad (11)$$

where  $r$  and  $f$  denote rigid and flexible part, respectively.  $M(q_i)$  and  $K_{ff}$  are the positive definite symmetric inertia matrix and positive definite diagonal stiffness matrix respectively.

The elements ( $i=n+1, j=n+1$ ) of the inertia matrix and stiffness matrices for a single link robot with one vibration mode take on the expression below.

$$m_{11}(q) = J_h + J_p + \rho \frac{\ell^3}{3}$$

$$m_{12}(q) = \rho \int_0^\ell x \phi_1 dx$$

$$m_{21}(q) = m_{12}^T(q)$$

$$m_{22}(q) = m_p \phi_\ell^2 + m_h \phi_0^2 + \rho \int_0^\ell x \phi_1 dx$$

$$k_{22} = EI \int_0^\ell \phi_1''^2 dx$$

### 3. Hybrid Controller

Similarly to most of the contributions in the field, the proposed control method is developed for the one-link flexible arm as a first step towards general multi-link arms. The suggested control approach consists of two sub-controllers; one is slow sub-controller to tracking the desired input, and the other is fast sub-controller to damp out vibration. Using the dynamic model eq. (11) and eq. (12), a hybrid controller is designed. The rigid sub-controller will be built using the inverse control approach (Augmented PD controller), while the flexible sub-controller is sliding mode control (SMC).



### 3.1 Augmented PD Controller

The purposes of slow sub-controller are tracking input without steady state error and reducing coupling effect from flexibility. To design the control  $u_r$  for the  $n$  joint coordinates  $q_r$ , infinitely stiff links are assumed. The rigid body model for the manipulator can be recovered from the  $n$  upper rows of eq. (12), by setting  $q_i = 0$  for all  $(n_e)$  flexible links. This yields  $q_e = \dot{q}_e = \ddot{q}_e = 0$ , and the equations of motion are then

$$M_r(q_r)\ddot{q}_r(t) + C_r(q_r, \dot{q}_r) + g_r(q_r) = u_r \quad (12)$$

Accurate measurements of joint variables, either angles or displacements and joint velocities are assumed to be available. If the tip location  $r_t$  of the manipulator is of interest, then

$$r_t = f(q_r) \quad (13)$$

the vector of desired joint coordinates  $q_r^d$  must be computed using the inverse kinematic equation

$$q_r^d = f^{-1}(r_t^d) \quad (14)$$

The well-known inverse dynamics control method is chosen here, where the control  $u_r$  is taken to be a function of the manipulator state in the form;

$$u_r = M_r(q_r)\ddot{q}_r + C_r(q_r, \dot{q}_r) + g_r(q_r) \quad (15)$$

Because the mass matrix  $M_r$  is invertible, the combined system reduces to

$$\ddot{q}_r = \ddot{q}_r^d \quad (16)$$

where  $u_r$  represents a new input vector, which is still to be chosen, for the system.

The approach

$$\ddot{q}_r = -K_p q_r - K_D \dot{q}_r + \ddot{q}_r^d \quad (17)$$

with constant control matrices  $K_p$  and  $K_D$  leads to a simple linear second-order system,

$$\ddot{q}_r + K_D \dot{q}_r + K_p q_r = \ddot{q}_r^d \quad (18)$$

where  $r$  is the reference input. Under the assumption of positive definite matrices  $K_p$  and  $K_D$ , this system

is asymptotically stable. Given a desired trajectory  $q_r^d$ , one may choose

$$r = \ddot{q}_r^d + K_D \dot{q}_r^d + K_p q_r^d \quad (19)$$

The tracking error  $e = q_r^d - q_r$  then satisfies the homogeneous second-order differential equation

$$\ddot{e} + K_D \dot{e} + K_p e = 0 \quad (20)$$

Choosing  $K_p$  and  $K_D$  as diagonal gain matrices of the type

$$\begin{aligned} K_p &= \text{diag}\{\omega_1^2, \dots, \omega_n^2\} \\ K_D &= \text{diag}\{2\delta_1\omega_1, \dots, 2\delta_n\omega_n\} \end{aligned} \quad (21)$$

results in a closed-loop system that is globally decoupled. Each joint response is equal to the response of a second-order system characterized by a natural frequency  $\omega_i$  and a damping ratio  $\delta_i$ .

The method of inverse dynamics is attractive because the nonlinear coupled dynamics of the manipulator is canceled and replaced by  $n$  linear decoupled second-order systems. However, such exact cancellation schemes leave open many issues of sensitivity and robustness due to unavoidably imperfect compensation. These issues are addressed in several books dealing in details with modeling and control of robot manipulators, e.g. Spong et al 1989. However the final control law used in this paper is given by

$$u_r = M_r(q_r)\ddot{q}_r + K_r(q_r, \dot{q}_r) + g_r(q_r) \quad (22)$$

$$\ddot{q}_r = \ddot{q}_r^d + K_D(\dot{q}_r^d - \dot{q}_r) + K_p(q_r^d - q_r) \quad (23)$$

### 3.2 PI - Sliding Mode Controller (SMC)

The flexible sub-controller should be designed to damp out vibration. Sliding Mode Control (SMC) is often favored as a basic control approach, especially because of its insensitivity property toward the parametric uncertainties and the external disturbances. SMC are characterized by control laws that are discontinuous on a certain manifold in the state space, the so-called sliding surface. The control law is designed such that the representative point's trajectories of the closed-loop

system are attracted to the sliding surface and once on the sliding surface they slide towards the origin . However the major drawback in the SMC approach is the undesired phenomenon of chattering because of the discontinuous change of control laws across the sliding surface. In practical engineering systems, chattering may cause damage to system components, as well as excite unmodeled and high frequency plant dynamics , Kwatny et al (1987).

There exist several techniques to eliminate chattering. PI-SMC approach provides an effective way to resolve the chattering problem. In general, the first step to illustrate the standard SMC is to define a time-varying sliding surface,  $S(t)$ , that is linear and stable. The  $S(t)$  acting on the tracking-error expression selected in this work, is:

$$S(t) = \lambda e(t) + \dot{e}(t) \quad (24)$$

where  $\lambda$  is a strictly positive constant, and  $e(t)$  is the tracking error, while  $\dot{e}(t)$  is the time derivative of the tracking error  $e(t)$ . Since the aim of this controller is to damp out the vibration to zero, therefore  $q_f(t)$  and  $\dot{q}_f(t)$  are used instead of  $e(t)$  and  $\dot{e}(t)$  respectively, then eq. 24) becomes

$$S(t) = \lambda q_f(t) + \dot{q}_f(t) \quad (25)$$

Sliding mode means that once the state trajectory has reached the sliding surface  $S(e, \dot{e}) = 0$  the system trajectory remains on it while sliding into the origin (0,0), independently of model uncertainties, unmodeled frequencies, and disturbances, Quang (2000).

To keep the  $S(e, \dot{e})$  at zero, the control law is designed to satisfy the following sliding condition (Lyapunov function):

$$\dot{V} = \frac{1}{2} S(t)^T S(t) \leq 0 \quad (26)$$

Its time derivative becomes  $\dot{V} = \dot{S}S$  and the control  $u_f$  is chosen such that

$$\dot{S}(t)S(t) \leq -\eta |S(t)| \quad (27)$$

where  $\eta$  is a positive constant that guarantees the system trajectories hits the sliding surface in a finite

time. Essentially, eq. (26) states that the squared “distance” to the surface, as measured by  $S^T S$ , decreases along all system trajectories. Thus, eq. (27) provides a sufficient reaching condition such that the tracking error  $e_i$  will asymptotically converge to zero, Quang (2000). In order to meet that condition, the control law is chosen as follows

$$u_f = -K_s \text{sgn}(S) \quad (28)$$

where the sliding gain  $K_s > 0$  and  $\text{sgn}(S)$  is a sign (or signum) function, which is defined as

$$\text{sgn}(S) = \begin{cases} -1 & \text{if } S < 0 \\ 0 & \text{if } S = 0 \\ 1 & \text{if } S > 0 \end{cases} \quad (29)$$

As explained before, using a sign function often causes a chattering problem. A proportional-integral combination of the sliding function is proposed in a boundary layer in place of the signum function by Quang (2000). This continuous controller can force the system states to reach the sliding surface and attain high tracking performance. The equation for this saturated proportional-integral functions is given by

$$\rho_{PI}(\sigma_{PI}) = \begin{cases} 1 & \text{if } \sigma_{PI} > 1 \\ \sigma_{PI} + K_I \int_{t_{i0}}^{t_i} \sigma_{PI} & \text{if } -1 \leq \sigma_{PI} \leq 1, \\ -1 & \text{if } \sigma_{PI} < -1 \end{cases} \quad (30)$$

where

$$\sigma_{PI} = \frac{S}{\Phi};$$

where  $K_I > 0$  is an integral gain, and  $t_{i0}$  is the initial time when the system states enter the boundary layer  $B(t)$  which is defined as ,Nguyen et al (2003),

$$B(t) = \{e, |S(e, t)| \leq \Phi\}, \Phi > 0 \quad (31)$$

where  $|S(x, t)|$  is the distance between state  $e$  and sliding surface  $S$ ,  $\Phi$  is the boundary layer thickness.

If  $|\sigma_{PI}| \geq 1$  the integration term in eq. (30) will be reset to zero to prepare for the system state entering boundary layer. It is assumed that the

chosen integration gains  $K_I$  are sufficiently large such that

$$\begin{aligned}\dot{\sigma}_{PI} + K_I \sigma_{PI} &> 0 \quad \text{for all } \sigma_{PI} > 0 \\ \dot{\sigma}_{PI} + K_I \sigma_{PI} &< 0 \quad \text{for all } \sigma_{PI} < 0\end{aligned}\quad (32)$$

Inequalities (33) imply that  $\rho_{PI}$  increases for all  $\sigma_{PI} > 0$ , and  $\rho_{PI}$  decreases for all  $\sigma_{PI} < 0$  (Nguyen et al (2003)).

The overall Fuzzy PI +D control system is shown in **Fig. 2**.

Similar to the classical (PI+D) controller which uses two integrators, the fuzzy (PI + D)<sup>2</sup> control approach uses two fuzzy (PI + D) controllers. The first controller is used for set-point tracking control, while the second one is used for vibration damping. The block diagram of this approach is shown in **Fig. 3**.

Eight rules, “D output” had been used for fuzzy control output. The formulation for these rules is given by Tang et al (2001).

## 5. Simulation Results And Discussion

The simulation results for a robotic system that has single link with one mode are discussed. The numerical model used in the simulations is illustrated below. It is derived by using the assumed modes method with clamped-free shape functions presented in section 2. The link parameters are given in **Table 1**, these parameters are taken from Azad et al (2003). One mode shape approximation is used for this example. The inertia M, stiffness K, and damping D matrices, are obtained by using the Matlab program given in Manaty (2008).

$$M = \begin{bmatrix} 1.5623 & 0.1837 \\ 0.1837 & 0.3910 \end{bmatrix}$$

$$D = \begin{bmatrix} 0 & 0 \\ 0 & 0.1 \end{bmatrix} \quad K = \begin{bmatrix} 0 & 0 \\ 0 & 31.6931 \end{bmatrix}$$

The simulation results of a single link with one mode approximation using controllers (the hybrid and the fuzzy (PI+D)<sup>2</sup>) designed in section 3 and 4

## 4. The Fuzzy (Pi+D)<sup>2</sup> Controller

This approach was proposed by Soorasksa et al 1998, to control the flexible link manipulator. The overall fuzzy PI+D control law can be obtained by algebraically summing the fuzzy PI control law and the fuzzy D law together. The result is

$$\begin{aligned}u_{PID}(nT) &= u_{PI}(nT - T) + K_{uPI} \Delta u_{PI}(nT) + \\ &u_D(nT - T) - K_{uD} \Delta u_D(nT)\end{aligned}\quad (33)$$

to track a step reference input are shown in Figs 4 and 5.

In this simulation, gains for the hybrid controller are chosen as ( $K_P=5$  and  $K_D = 5$ ) for augmented controller. While the gains for the SMC ( $\lambda = 10$ ,  $\phi = 0.1$ ,  $K_I = 10$ ,  $K_S = 4$ ).

A (1 radian) step reference is applied to the hybrid controller, as well as the fuzzy (PI+D)<sup>2</sup> controller (with  $K_P = 4000$  and  $K_D = 800$  for rigid part and  $K_P = 4000$  and  $kD = 600$  for flexible part).

The proposed hybrid controller demonstrates a significant improvement over the other controller (fuzzy (PI+D)<sup>2</sup>) as illustrated in **Fig. 4**. The manipulator tracks the step reference trajectory with almost no overshoot or undershoots. The hybrid controller has better settling time (2.5 sec) and has virtually no ripple.

The fuzzy (PI+D)<sup>2</sup> controller results show that there is small oscillations in the transient response causing the step response to reach steady-state in (4.7 sec). The fuzzy controller has slightly longer settling time 3.5 sec.

The control signal for the rigid link and for the flexible mode is shown in **Fig. 8** while the tracking error signal is shown in **Fig. 6**. Both results show that the two controllers approaches give unequal torque values for the rigid link and for the deflection as shown in **Fig. 7**. It can be noticed that the error system with hybrid controller reaches zero steady state error after a few seconds (3 sec) while system response when using the fuzzy (PI+D)<sup>2</sup> controller there is (0.1) steady state error.

## 6. Conclusions

In this paper, a model for the single flexible-link manipulator which describes both linear and nonlinear behavior of the entire system has been developed.

Two approaches to control the flexible link manipulator are used. The first one is a hybrid (PD and sliding mode) controller. Where, the augmented PD controller is used as a hub position control while the sliding mode control is used to damp out the vibration of tip position. The second control approach is to use a fuzzy (PI+D)<sup>2</sup> controller for both, the hub angle control and tip deflection control.

The hybrid controller has a steady state error which reaches zero in a fast manner and gives good tracking to the trajectory while the fuzzy (PI+D)<sup>2</sup> has a small steady state error when both controllers try to track the step reference input.

The control torque signal for the hybrid controller shows higher initial torque and lower mean value torque signal than that using fuzzy (PI+D)<sup>2</sup>.

In general the hybrid controller shows better behavior than the proposed fuzzy (PI+D)<sup>2</sup> controller for the single flexible link manipulator.

## References

- Alwan A. Adel, Kazem I. Bahaa, Hussein T. Mustafa "Modeling and Trajectory Control of Planar Flexible Robot Arm", UOB Journal of applied and pure sciences, Vol. 15 No.4, pp. 1818-1826, 2008.
- Azad, A. K. M., Tokhi M. O., and Anand N. , "Teaching of Control for Complex Systems Through Simulation," Proceedings of the 2003 ASEE/WFEO International Colloquium, American Society for Engineering Education, 2003.
- Benati, M., and Morro A., "Formulation of Equations of Motion for a Chain of Flexible Links Using Hamilton's Principle," ASME Journal of Dynamic Systems, Measurements, and Control, vol. 116, pp. 81-88, 1994.
- Book, W. J., "Modeling, Design, And Control Of Flexible Manipulator Arms: A Tutorial Review," Proceedings of the 29th IEEE Conference on Decision and Control, pp. 500-506, Dec. 1990.
- Book, W.J., Maizz-Neto O., and Whitney D.E., "Feedback Control of Two Beam, Two Joint Systems with Distributed Flexibility," ASME Journal of Dynamic Systems, Measurements, and Control, vol. 97, pp. 424-431, 1975.
- Boyer, F., and Coiffet, P. "Generalisation Of Newton-Euler Model For Flexible Manipulators," Journal of Robotic Systems, vol. 13, no. 1, pp. 11-24, 1996.
- Chapnik, B. V., Heppler G. R., and Aplevich J. D., "Modeling Impact On A One-Link Flexible Robotic Arm," IEEE Transactions on Robotics and Automation, vol. 7, no. 4, August 1991.
- De Luca, A., and Siciliano B., "Closed-Form Dynamic Model Of Planar Multilink Lightweight Robots," IEEE Transactions on Systems, Man, and Cybernetics, vol. 21, no. 4, pp. 826-839, 1991.
- De Luca, A., Lucibello P., and Ulivi G., "Inversion Techniques For Trajectory Control Of Flexible Robot Arms," Journal of robotic systems, vol. 6, no. 4, pp. 325-344, 1989.
- Geniele, H., Patel R. V., and . Khorasani K, "End-Point Control Of A Single Link Flexible Manipulator: Theory And Experiments," IEEE Transactions on Control Systems Technology, vol. 5, no. 6, 556-560, 1997.
- Hastings, G. G., and Book W. J., "A Linear Dynamic Model For Flexible Robot Manipulators," IEEE Control Systems Magazine, pp. 61-64, February 1987.
- Kwatny, H. G., and Siu T. L., "Chattering in Variable Structure Feedback Systems," Proceedings of IFAC 10th World Conference, vol. 8, pp. 307-314, 1987.
- Manaty, A. M., "Hybrid Controller For A Flexible Link Robot Manipulator", Ph.D. thesis, University of technology, control and systems dept., Nov. 2008.
- Natarajan, K., Yu S., and Karray F., "Modeling And Control Design For A Flexible-Link Manipulator" IEEE Canadian Conference on Electrical and Computer Engineering, vol. 1, pp. 117-120, issue 24-28 May 1998.



Nguyen, T. V. M., Ha Q. P. and Nguyen H. T., "A Chattering-Free Variable Structure Controller for Tracking of Robotic Manipulators," Faculty of Engineering, University of Technology, Sydney, 2003.

Quang, N. H., "Robust Low Level Control of Robotic Excavation," Ph.D., Thesis, Australian Centre for Field Robotics, University of Sydney, Mar. 2000.

Singh, S. N., and Schy A. A., "Control of Elastic Robotic Systems by Nonlinear Inversion and Modal Damping," ASME Journal of Dynamic Systems, Measurements, and Control, vol. 108, pp. 180-189, 1986

Sooraksa, P., and Chen G., "Mathematical Modeling and Fuzzy Control of a Flexible-Link Robot Arm," Mathematical Computation and Modelling, vol. 27, no. 6, pp. 73-93, 1998.

Spong, M. and Vidyasagar M., "Robot Dynamics and Control," McGraw-Hill, 1989.

Talebi, H. A., "Neural Network-Based Control of Flexible-Link Manipulators," Ph. D. thesis, Concordia University, Montréal, Québec, Canada, 1997.

Tang K. S., Man K. F., Chen G. and Kwong S., "An optimal fuzzy PID controller", IEEE Transaction on industrial Electronics, Vol.48, No. 4, pp 757-765, Aug. 2001.

Tang, Y., Sun F., Sun Z., "Neural Network Control Of Flexible-Link Manipulators Using Sliding Mode," Neurocomputing, no. 70, pp. 288–295, 2006.

Thomson, W. T., "Theory Of Vibration With Applications," Prentice-Hall Inc., Englewood Cliffs, N. J., 2nd edition. 1981.

## List of Symbols

$e(t)$	Tracking error
$EI$	Flexural rigidity (N.m <sup>2</sup> )
$J$	Total inertia (kg.m <sup>2</sup> )
$J_h$	Hub inertia (kg.m <sup>2</sup> )
$J_p$	Payload inertia (kg.m <sup>2</sup> )
$K$	Stiffness matrix
$K_D$	Derivative gain
$K_S$	Sliding gain
$K_I$	Integral gain
$K_p$	proportional gain
$K_{UPI}$	PI constant control gain
$L$	Lagrangian
$l$	Length of the link (m)
$M$	Inertia matrix
$m_l$	Mass of the link (kg)
$m_p$	Mass of the payload (kg)
$P$	Position vector of any point along the link
$q$	Generalized coordinate
$\dot{q}_r$	Velocity of the rigid part
$\dot{q}_r^d$	Desired velocity of joint coordinate
$r$	Position vector of link end
$S(t)$	Time-varying sliding surface
$T$	Kinetic energy
$T_l$	Kinetic energy for link
$T_h$	Kinetic energy for hub
$T_p$	Kinetic energy for payload
$u_f$	Control signal for flexible part
$u_r$	Control signal for rigid part
$V$	Potential energy
$V_e$	Potential energy due to elasticity
$V_g$	Potential energy due to gravity
$w_i(x,t)$	Deflection of a point x along the i <sup>th</sup> link
$w_l$	Deflection at tip position (m)
$\theta$	Joint position of the link (degree)
$\varphi$	Eigen function of the link
$\delta$	Flexible mode of the link
$\theta_c(t)$	Position of the center of mass
$\rho$	Mass density (kg/m)

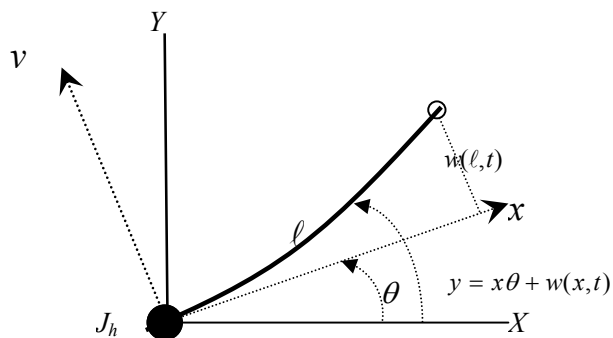


Fig. 1 Single Flexible Link Manipulator

Table 1 The Link parameters for simulation of manipulator, Azad et al 2003

Parameter	Value	Units
Length	1.22	m
Mass density	0.24	kg/m
Flexural rigidity	11.82	N . m <sup>2</sup>
Hub mass	2	kg
Hub moment of inertia	1.35	Kg. m <sup>2</sup>
Payload mass	0.045	Kg
Payload inertia	0.067	Kg.m <sup>2</sup>
damping	0.1	—

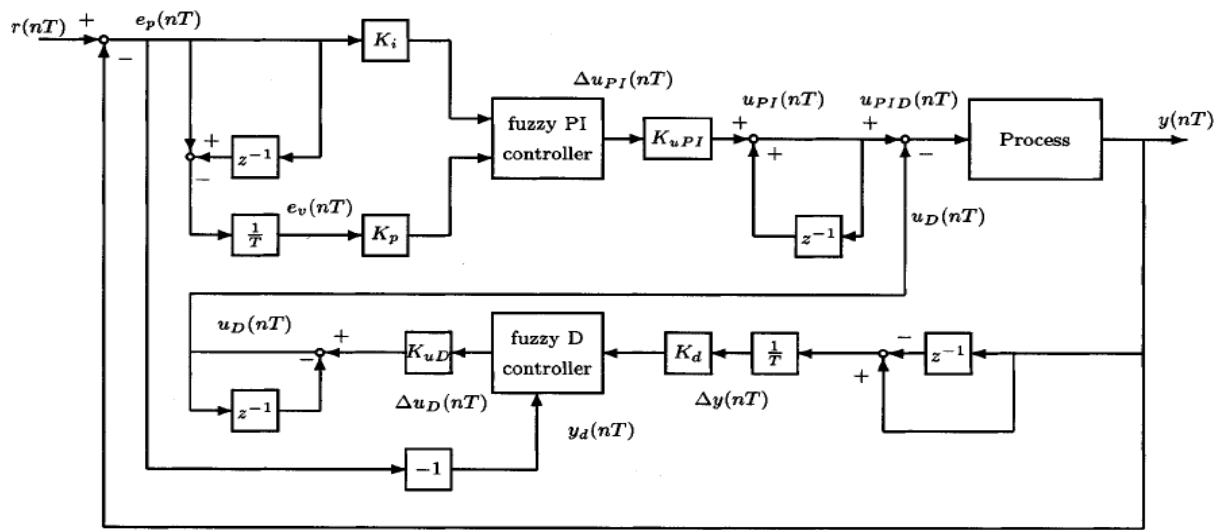
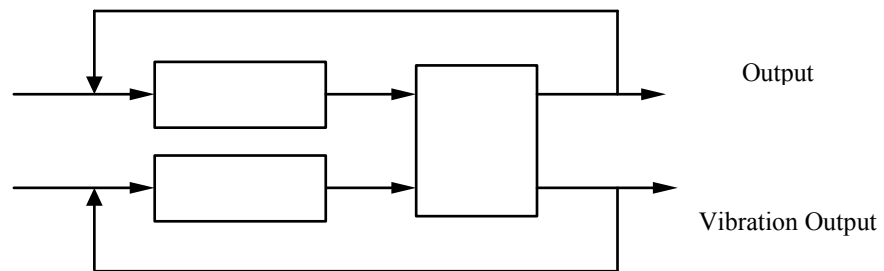
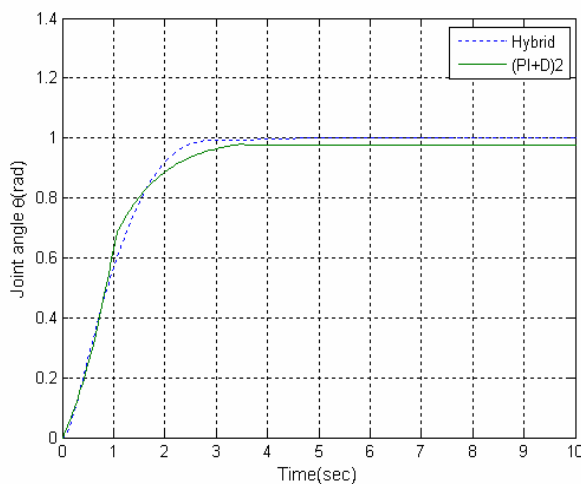
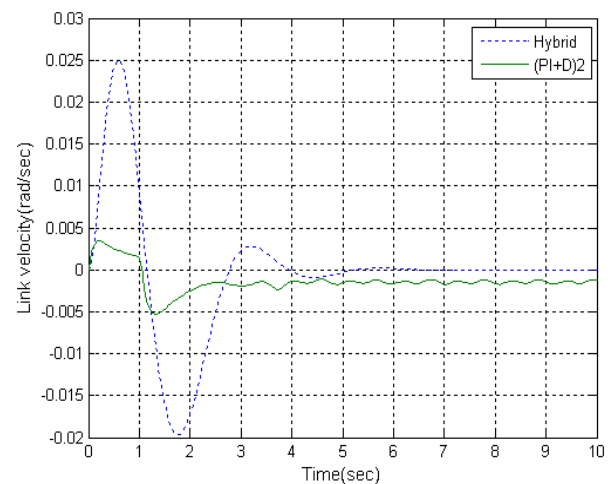


Fig. 2 Fuzzy PI+D control system Sooraksa et al 1998.

Fig. 3 The fuzzy  $(PI+D)^2$  control approach Sooraksa et al 1998.

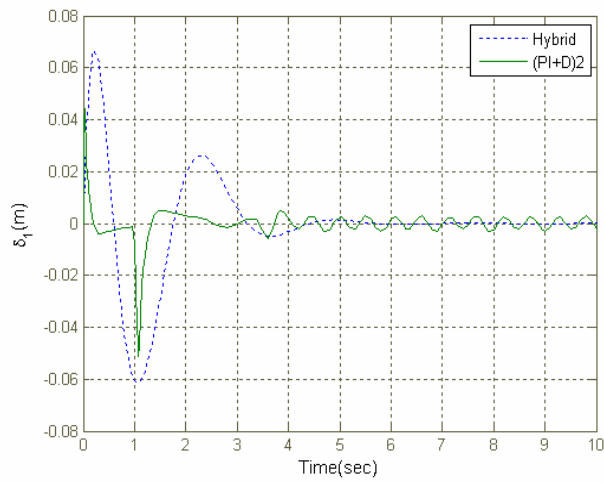
(a) Tracking position



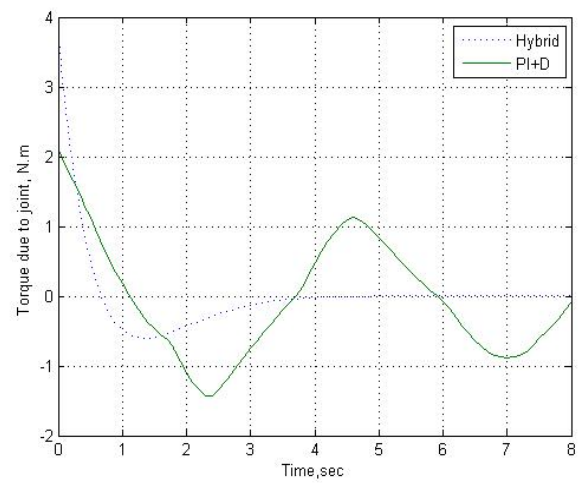
(b) Tracking velocity

Fig. 4 Comparison of tracking performance of hybrid and fuzzy  $(PI+D)^2$  controllers.

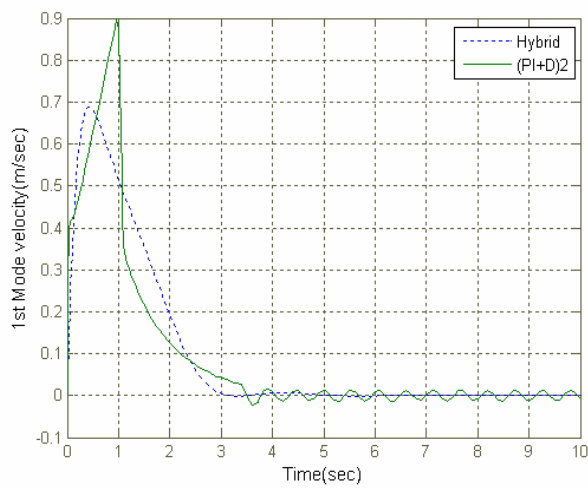




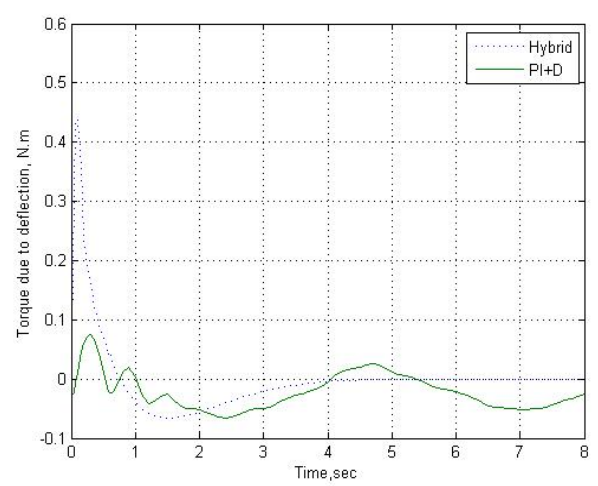
(a) Tip deflection position



(a) Control torque signal for the rigid part.



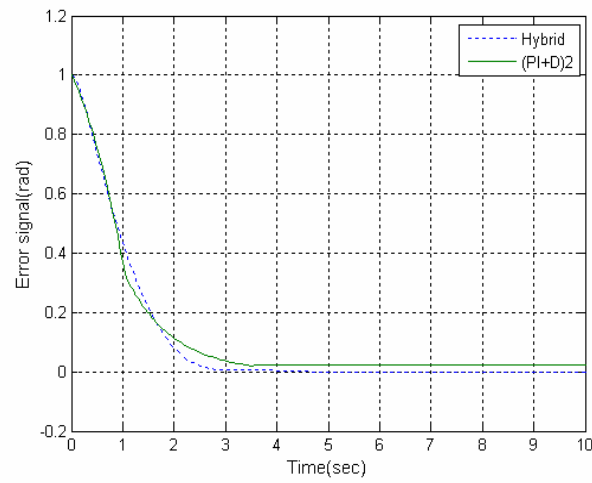
(b) Tip deflection velocity



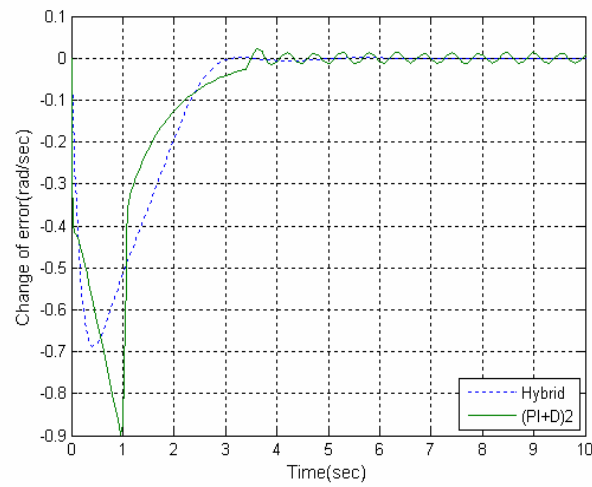
(b) Control torque signal for the flexible part.

Fig. 5 Comparison of first mode suppression performance of hybrid and fuzzy  $(PI+D)^2$  controllers.

Fig. 6 Control torque signal of hybrid and fuzzy  $(PI+D)^2$  controllers.



(a) Rigid part error signal.



(b) Flexible part error signal.

Fig. 7 Tracking error signals.